Ground motions and source mechanisms of earthquakes in multiscales – microseismicity to macroseismicity

by

Chen Gu

Submitted to the Department of Earth, Atmospheric, and Planetary Sciences
in partial fulfillment of the requirements for the degree of

Doctor of Philosophy

at the

MASSACHUSETTS INSTITUTE OF TECHNOLOGY

September 2016

Signature redacted

Author .....
Department of Earth, Atmospheric, and Planetary Sciences
September 12, 2016

Signature redacted

Certified by .....
J. Brian Evans
Professor of Geophysics
Thesis Co-supervisor

Signature redacted

Certified by .....
M. Nafi Toksöz
Robert R. Shrock Professor of Geophysics
Thesis Co-supervisor

Signature redacted

Accepted by ..
Robert D. van der Hilst
Schlumberger Professor of Earth and Planetary Sciences
Head, Department of Earth, Atmospheric, and Planetary Sciences

Ground motions and source mechanisms of earthquakes in multiscales – microseismicity to macroseismicity

by

Chen Gu

Submitted to the Department of Earth, Atmospheric, and Planetary Sciences
on September 12, 2016, in partial fulfillment of the
requirements for the degree of
Doctor of Philosophy

Abstract

This thesis focuses on the source mechanisms of Earthquakes of different scales, from the micro-seismicity in oil/gas fields in Oman, to moderate earthquakes in Kuwait, and finally to pico-seismicity, i.e. acoustic emission, in the laboratory.

To investigate the source mechanisms as well as their uncertainties, a waveform-based Bayesian moment tensor inversion approach was developed and validated by synthetic tests. The Bayesian approach estimates the source parameters and the uncertainties by generating a posterior probability density function of the source parameters. The effects of location, velocity model, and error model of the data on the posterior prediction of the source parameters are discussed. This Bayesian moment tensor inversion method was first applied to the well-documented induced seismicity data in an oil/gas field in Oman.

On Chapter 3, we move on to another mideast country – Kuwait. We conducted ground motion calculations in Kuwait due to regional large earthquakes and to local seismicity. We found that the regional earthquakes with low-frequency and long-duration surface waves were most likely to affect tall buildings, while the local smaller earthquakes are most likely to affect small and old structures constructed before the adoption of building codes. Using the Bayesian moment tensor inversion method, we studied the source mechanisms of local earthquakes in Kuwait. Historically, Kuwait has low local seismicity; however, in recent years the KNSN has monitored more and more local earthquakes. In 2015, two local earthquakes - Mw4.5 on 03/21/2015 and Mw4.1 on 08/18/2015 - have been recorded by both the Incorporated Research Institutions for Seismology (IRIS) and KNSN, and were widely felt by people in Kuwait. Most earthquakes in Kuwait occurred close to oil/gas fields. The earthquakes are generally small (Mw < 5) and are shallow with focal depths of about 2 to 8 km. We determined the location and source mechanism of these local earthquakes, with the uncertainties, using a Bayesian inversion method. Our results show that most likely these local earthquakes occurred on pre-existing faults and may have been triggered by oil field activities. In Kuwait, where oil fields are close to populated areas, these induced earthquakes could produce ground accelerations high enough to

cause damage to local structures.

Chapter 4 is devoted to the study of acoustic emissions during the rock fracturing experiments in the laboratory. The laboratory fracturing can produce pico-seismicity with magnitude as small as -7. Three event-detection and three location algorithms have been implemented to the acoustic emission (AE) data from the fracturing experiment of a cylindrical Berea sandstone sample (Diameter: 36.43 mm; Height: 76.7 mm). The first P-amplitude and waveform-based Bayesian moment tensor inversion algorithms have been applied to the AE data to study the source mechanisms of this fracturing related pico-seismicity. The location, and sensor calibration are discussed in the thesis.

The main contribution from this thesis are: 1) Developing a waveform-based Bayesian moment tensor approach; 2) Understanding the source mechanisms of local earthquakes in Kuwait, and simulating the ground motion due to regional and local earthquakes in Kuwait; 3) Characterizing the laboratory-scale fractures using the fracturing related acoustic emission data.

Thesis Co-supervisor: J. Brian Evans
Title: Professor of Geophysics

Thesis Co-supervisor: M. Nafi Toksöz
Title: Robert R. Shrock Professor of Geophysics

Acknowledgments

I am greatly thankful to my thesis co-advisor, Prof. M. Nafi Toksöz. With his help after my general exam, I was able to continue my PhD study after my general exam, and finally finish my thesis within four years. Prof. Toksöz is an advisor, who treats his students nicely, and care for students like his children. I really enjoy working with him. I also thank his wife Charlotte for taking good care of me and revising my writings.

I would also thank my another thesis co-advisor Prof. J. Brian Evans, who always supports the ideas of students, and always make creative suggestions. Many thanks to my thesis committee members, Prof. Germán A Prieto and Prof. Youssef M Marzouk. They spent a lot of time on my research.

Earth Resources Laboratory is the home of my study at MIT. I would like to take this opportunity to thank many of the former and current students and staff of ERL and Green Building. I thank Prof. Sang-Heon Dan Shim to give me the chance to study at MIT, and patiently taught and trained me to be a scientist. Prof. Robert van der Hilst advised me for my second general project, with his patient tutoring, I started to learn seismology. With their nice and patient advising, I passed the general exam. Many thanks to Prof. Bradford Hager, Prof. Dale Morgan, and Prof. Thomas Herring for sharing their knowledge with me. I would like to thank Junlun Li, and Fuxian Song, who developed the pioneering work of microseismicty in our group, which my thesis work is based on. Sadi Kuleli and Haijiang Zhang also helped me a lot on my research project. Bill Rodi was of great help in statistics and inversion. Zhenya Zhu taught me acoustics patiently.

The second Chapter of my thesis focuses on the earthquakes in Kuwait. I acknowledge Kuwait-MIT center for funding the project. Many thanks to Professor Oral Büyüköztürk, for supporting my research. I thank Hao Sun and Aurelien Mordrent for their help and communication in the project. I greatly thank my Kuwait colleagues, Farah Al-Jeri and Abdullah Al-Enize, for providing data for me, working with me, and teaching me Arabic.

I thank Yunyue Li, Aurelien Mordrent, Piero Pelo, and Frank Willams Abdulaziz Al-Muhaidib, Lucas A. Willemsen and Nasruddin Nazerali, who are great friends and colleagues. I enjoyed conversations with them not only on research topics but also on extracurricular activities. I would also like to thank Yingcai Zheng, Qin Cao, Xuefeng Shang, Hui Huang, Chunquan Yu, Hua Wang, Shujuan Mao, Jianhua Gong, Xinding Fang, Min Chen, Di Yang, Tianrun Chen, Sudipta Sarkar, Alan Richardson, Andrey Shabelansky, Ahmad Zamanian, Oleg Poliannikov, Jonathan Kane, and many others for their help and encouragement. Anna Shaughnessy, Joshua Kastorf, Terri Macloon, Sue Turbak, who take good care of everyone at ERL and Linda Meinke, who is always helpful to solve the computer problems. Carol Sprague, Roberta Allard and Vicki McKenna in the Department Education Office gave me a lot of help.

Outside MIT, I would like to acknowledge Conocophillips for offering an internship position in 2014. Archangelo Sena and Wenjie Jiao give me big help on my internship projects. With that intern experience, I can better understand the importance and potential applications of my PhD research. During my internship, I met some good friends, Yanhua Yuan, Eve Wang, and Yi Shen.

Besides the geophysical research, with the help of my friends in other disciplines, I got the chance to join other interesting projects. Mo Jiang collaborated with me to solve some problems of chemical engineering using geophysical techniques. This collaboration gave me the confidence to conduct inter-disciplinary research. Enying Zheng, a social scientist, advised me to study the evolution of science and technology in ancient China. Weng Cheong Lam, an archeologist, made my dream of archeology come true.

Life is sometimes challenging, I thank my friends – Enying Zheng, Ru Chen, Min Ding, Lidan Wu, Ping Zhai, Zheyan Hong, Xi Xu, Tianhua Wu, Yuanyuan Yao, Liang Wu, Mo Jiang, Wen Zheng, Wenjun Zhang, Tiky Luo, Wen Sang, Zhibiao Rao, Hui Zhang, Binghong Han, Zhaohong Han, Tewei Luo, Sheng Xu, Yaodong Zhang, Xu Zhang, and many others to brings me a lot of confidence and happiness.

Finally, I would like to thank my father Hongxing Gu and mother Haixian Chen for their love and support for me.

Contents

List of Figures

List of Tables

Chapter 1

Introduction

1.1 Background and motivations

Earthquakes happen in different scales. Source mechanisms of earthquakes are important to investigate the physics of seismic process from the acoustic emissions in laboratory experiments, to micro-earthquakes in oil/gas fields, to local earthquakes, and to regional moderate and large earthquakes.

Human beings have a long history recording and studying earthquakes, and developing seismometers. The earliest recorded earthquake occurred in 1831 BC, located at Mount Tai in Shandong province eastern China, according to "Bamboo Annals". Since 780 BC in Zhou Dynasty in China, Chinese started to record the occurring of earthquakes. In 132 AD, a Chinese scientist - Zhang Heng - invented the first seismometer in the world, which could indicate the direction of the earthquake over 300 miles away. However, none of these ancient earthquake records provide a quantitative description of the earthquakes.

With the appearance of early spring-pendulum seismometers in 1751, earthquake signal has started to be recorded and related to the seismic processes. Since 1900, people built seismic networks to record the earthquakes. The development of instruments make it possible to acquire earthquake data in a very broad scales, from the global seismology, to moderate local seismicity, to microseismicity in oil/gas fields, to acoustic emission in the laboratory scale.

The bridging of the seismic signal to the real physics of the seismic processes becomes challenging when the scales that we are able to explore become broader and broader and the environments where earthquakes happen becomes more and more complex. The objective of this thesis is to study the earthquakes in multi-scales: determine their source characteristics, evaluate their potential effects on structures and seismic safety, and develop a better understanding of the physics of earthquakes.

1.2 Previous studies

1.2.1 Bayesian moment tensor inversion

The source mechanisms of the great majority of tectonic earthquakes can be described by a double-couple (DC), corresponding to a shear fracture. However, some events in volcanic, geothermal, and salt dome areas exhibit more complex source mechanisms with non-DC components, such as volumetric component (ISO) and compensated linear vector dipole (CLVD) (Cespuglio et al., 1996; Panza and Saraò, 2000; Templeton and Dreger, 2006; Nayak and Dreger, 2014). These non-DC components have also been related to mine collapses and nuclear explosions (Ford et al., 2009a,b). Previous research on the analysis of induced seismic events in conventional oil/gas fields assumed a DC source mechanism (Li et al., 2011a,b; Li, 2013). Assuming full moment source mechanisms, Horálek et al. (2010) found a DC-dominated source mechanism of the induced micro-earthquakes in a geothermal area during massive fluid injection. However, recent studies have shown interest in non-DC components of source moment tensors in hydraulic fracturing events (Šílený et al., 2009; Warpinski and Du, 2010; Song and Toksöz, 2011; Song, 2013).

Many studies have implemented the inversion of the full moment tensor by the least-squares (LSQ) method and the regularized LSQ method (Sipkin, 1982; Šílenỳ et al., 1992, 1996). However, LSQ methods have disadvantages in estimating and interpreting the uncertainty of the moment tensor solutions, since the LSQ methods only search for the best moment tensor solution and do not give the probability dis-

tributions of the solution. An important question for full moment tensor inversion is whether the non-DC components are real. Some research has applied an F-test to check the significance of the non-DC components (Templeton and Dreger, 2006; Šílený et al., 2009; Horálek et al., 2010; Nayak and Dreger, 2014). LSQ methods do allow a limited uncertainty quantification, based on the Hessian of the misfit function near the LSQ point estimate. But this is only a local and linearized estimate of uncertainty, and can be difficult to interpret in the regularized case. Alternatively, to address the uncertainties of moment tensors resulting from the data noise or imperfect station coverage, many LSQ-based moment tensor inversion studies have applied re-sampling methods to the data, such as Monte Carlo noise realization methods and jackknife tests (Šílený et al., 2009; Stierle et al., 2014a,b). The uncertainties of the moment tensor results were obtained by statistically analyzing the solutions from the resampled data. Du and Warpinski (2011) theoretically derived the uncertainty of the focal plane solutions of seismic sources due to Gaussian noise contamination. In addition, to estimate the uncertainties from earthquake mislocation and velocity mismodeling, some research has observed the effects of mislocation and velocity mismodeling on the moment tensor solutions by performing location and/or velocity model perturbation tests (Stierle et al., 2014a,b). These tests only show how much the inverted parameter changes with the particular changes of earthquake location and velocity model. They did not actually give the statistical uncertainties of the inverted parameters. In addition, Nayak and Dreger (2014) assessed the sensitivity of the moment tensor and location together by statistically analyzing all the feasible moment tensor and location solutions with a variance reduction larger than a threshold. This method actually provides better estimates of the uncertainties of moment tensor and location solutions. The problem is that it is hard to illustrate how to choose a threshold, and why one should choose a threshold of a certain value.

Compared to LSQ methods, Bayesian inversion methods have the advantages of quantifying the uncertainties of model parameters by characterizing a posterior probability distribution over the parameter space (Tarantola, 2005; Kaipio and Somersalo, 2006; Stuart, 2010). Some studies have conducted Bayesian moment tensor inversion

on moderate and large earthquakes. Duputel et al. (2012) introduced a Bayesian moment tensor inversion method to estimate the uncertainties of source mechanisms for large earthquakes ($M_w \geq 6.0$) using W phase waveforms from a global seismic network. That study did not determine the uncertainty of seismic locations jointly with the moment tensor. A very recent paper by Mustać and Tkalčić (2016) has developed a Bayesian full moment tensor inversion for a moderate-size earthquake with a well-studied source mechanism using a regional seismic network. In that research, both the uncertainty of seismic location and moment tensor have been studied by implementing an outer Markov chain to sample the location parameters, and an inner chain to sample the moment tensor parameters.

1.2.2 Ground motion due to regional and local earthquakes in Kuwait

Previous research has provided useful methods to calculate the ground motion in a region. The ground motion prediction equation is a typical method to estimate ground motion intensity based on the observed seismic data and attenuation laws (Abrahamson and Shedlock, 1997). However, this method does not include any physics of earthquake source rupture and ignore the effects of complex crustal structures along the wave propagation path on the wave field. To make the predication more physical and realistic, many studies use simulation methods to predict ground motions according to a virtual future large earthquake (Olsen et al., 1995; Pitarka et al., 1998; Olsen, 2000; Olsen et al., 2006, 2009). The reliability of these simulation methods depends on the accuracy of the earthquake source rupture model, the seismic structure where the wave propagated, and the nonlinear site effects. In the recent decade, increasing studies have used the ambient seismic field method to predict the ground motion from sources around seismic stations (Prieto and Beroza, 2008; Denolle et al., 2013, 2014). This ambient seismic field method can only predict the ground motion near the seismic stations. In this thesis, we use the simulation method to calculate the ground motion, since we are focusing on the ground motion calculation from the

regional large earthquakes in the Zagros Fold Belt.

The possibility to use the simulation method to calculate the ground motion in Kuwait due to regional large earthquakes is based on the well-documented studies on the source mechanism in the Zagros belt and seismic structure in Arabic peninsula, which provided valuable background and references for the ground motion calculation in this paper (Jackson and McKenzie, 1984; Bou-Rabee, 2000; Pasyanos et al., 2007; Sadek, 2004). Carman (1996) has studied the five structural elements in Kuwait based on the data of the seismic structure maps, oil file wells, remote sensing/imaging data, and in rocks. That study indicated a northeast trend for the principal horizontal stress field. Pasyanos et al. (2007) studied the crustal structures in Kuwait using the joint inversion of teleseismic receiver function and Rayleigh and Love fundamental mode surface wave group velocity dispersion. In addition, some previous research has been conducted on the long-period ground motion in the Arabian Gulf (Pitarka et al., 2012, 2015), although there have not been quite detailed studies in the state of Kuwait.

For the ground motion due to local earthquakes in Kuwait, although the source mechanisms for these $M < 5$ earthquakes are not available from any previous studies, the geological and geophysical studies focused on the tectonic and seismic structures in Kuwait and Arabic peninsula (Carman, 1996; Bou-Rabee and VanMarcke, 2001; Pasyanos et al., 2007; Laske et al., 2013), and more detailed studies about the shallow structures in Kuwait have (Bou-Rabee and VanMarcke, 2001; Bou-Rabee, 2000) provided valuable background references for the source mechanism study of local earthquakes and the ground motion calculation in this thesis.

1.2.3 Acoustic emission

The laboratory controlled fracturing in rock samples would generate the acoustic emission (AE) – elastic energy related to very small "earthquakes" with the fault plane size of tens to hundreds cm^2. The acoustic emissions are of great important to study the fracturing mechanics because under the laboratory experiments we are better informed about the stress conditions, the rock properties, and the fault plane

geometry during the fracturing process. However, the low signal-to-noise ratio of the acoustic emission data, the high occurrence rate of AE events, and the difficulties of the sensor calibrations make the event detection, location, and source mechanism inversion difficult to implement.

The history of acoustic emission has been traced back to the middle 20th century before the terminology "AE" was created, Obert and Duvall (1942) firstly detected small noise emitted from rock in compression, and attributed these signals to microfractures in the rock. Kaiser (1950) recorded signals from the tensile specimens of metallic materials. Later, Schofield (1961) firstly used the terminology AE in his work. Since 1960's, many following work historically contributed to the development of AE techniques and applied the AE techniques to to diverse engineering and scientific areas (Drouillard and Laner, 1978; Drouillard, 1987, 1996; Grosse and Ohtsu, 2008).

During the past 50 years, fracture characterization has become one of the most important application areas of AE techniques. Many early studies from 1960's to 1970's have used AE techniques to investigate fracturing and deformation processes of rocks (Savage and Mansinha, 1963; Scholz, 1967, 1968a,b; Lockner and Byerlee, 1977). Savage and Mansinha (1963) studied the radiation pattern of AE due to a tensile failure in a 2-D glass plate. Scholz (1968b) determined the microfracture frequencies by AE event detection, and AE was also located in space by Scholz (1968a) and found to be to locate the fracture during the compression of granite. Lockner and Byerlee (1977) published the pioneering work of locate hydraulic fractures using AE.

Recently, with the increasing interests on the hydraulic fracturing in unconventional oil/gas fields, AE-based laboratory hydraulic fracturing studies has drawn attention in both academia and industry. Stanchits et al. (2011) studied the fracturing of porous rock induced by fluid injection. Ishida et al. (2012); Fu et al. (2015) conducted an experimental study on interaction between hydraulic fractures and partially-cemented natural fractures. Hampton et al. (2015) investigated the fracture dimension when the laboratory hydraulic fracture interacted with natural

discontinuity. Goodfellow et al. (2015) studied the hydraulic fracture energy budget from the laboratory AE study.

Efficient and reliable detection, location, and source analysis methods for AE are crucial to produce fast and accurate results. The similarity of AE and earthquakes suggests it a possible method to study earthquake mechanism (Scholz, 1968a). On the other hand, methods developed in modern seismology can be used to improve the AE analysis. For the event detection, Swindell and Snell (1977) developed a processor automatic signal detection system. (McEvilly and Majer, 1982) introduced an automated seismic processor for microearthquake networks. Earle and Shearer (1994) used an automatic-picking algorithm to characterize global seismograms . (Maeda, 1985) suggested a method for reading and checking phase times in auto-processing system of seismic wave data. Kao and Shan (2004) introduced the source-scanning algorithm to map the distribution of seismic sources in time and space. Kurz et al. (2005) summarized the strategies for reliable automatic onset time picking of AE. All the algorithms in that paper are originated from the seismic event detection.

For the earthquake location, Lomax et al. (2000) developed a Bayesian location algorithm to determine the location, as well as the uncertainties. A double difference location algorithm was introduced to mitigate the effects of inaccurate velocity model on location and improve the accuracy of the relative location(Waldhauser and Ellsworth, 2000). Recent studies for microseismicity and tremor earthquakes have produced more efficient location algorithms dealing with large data set with low signal-to-noise ratio. Zhang et al. (2014) introduced a new method for earthquake depth determination by stacking multiple-station autocorrelograms. Zhang and Wen (2015) suggested an effective method for small event detection and locate. (Grigoli et al., 2013) developed an automated seismic event location by travel-time stacking. Frank and Shapiro (2014) introduced an automatic detection of low-frequency earthquakes (LFEs) based on a beamformed network response Location.

For the AE source analysis, the most common method used in AE is the polarity method using the first-P polarity, and the moment tensor inversion method using the first-P amplitude (Pettitt, 1998; Graham et al., 2010). Although the first-P ampli-

tude moment tensor inversion methods are also used in seismology, many studies of microseismicity used the waveform-based moment tensor inversion method to determine the source mechanism (Li et al., 2011a,b; Song and Toksöz, 2011; Gu et al., submitted).

1.3 Thesis outline

The thesis demonstrate the Bayesian source mechanism inversion method. We applied the source mechanism inversion methods to earthquakes in different scales, as small as "centimeter" scale, such as the acoustic emissions in laboratory fracturing experiments; to "meter" scale, such as the micro-seismicity happening in oil/gas fields in Oman; to "kilometer" scale, such as local earthquakes widely felted in a Kuwait.

Using micro-seismicity data well-studied in an oil/gas field in Oman. Chapter 2 brings up the question of uncertainty quantification of the source mechanisms results. To solve this problem, Chapter 2 developed a waveform-based Bayesian full moment tensor inversion method to do both the source mechanism inversion and uncertainty quantification. This method are first validated using detailed synthetic tests, and then applied to real microseismic data.

We broaden our investigation to earthquakes recorded in Kuwait in Chapter 3. Located at the gulf area in Arabian Peninsular, Kuwait has been affected by large tectonic earthquakes in Zagros fault. In the first part of Chapter 3, we simulated the ground motion due to large earthquakes in Zagros belt. In the second part of Chapter 3, we studied the local earthquakes in Kuwait. Historically, Kuwait itself is an aseismic place, however recently more and more local earthquakes have happened in Kuwait. We investigate the source mechanisms of these local earthquakes in Kuwait, using the Bayesian moment tensor inversion method. Based on the source mechanism results, the ground motion due to local earthquakes are simulated.

After explaining the Bayesian source mechanism inversion method and applying the methods to the micro- and moderate-seismicity ($0 < M < 5$) near oil/gas field in Oman and Kuwait. Chapter 4 investigate even smaller "earthquakes" with the "fault"

size of tens to hundreds cm^2, i.e. the acoustic emissions corresponding to laboratory rock fracturing experiments. I first introduce several event detection methods to automatic pick events from the continuous acoustic emission (AE) data. Then I applied three location algorithm to AE data, and determined source mechanisms are using both the first-P amplitude and the full waveform data.

Chapter 5 concludes the whole thesis and proposes future researches.

Chapter 2

Bayesian Moment Tensor Inversion and Uncertainty Quantification for Induced Microseisimicity in an Oil/Gas Field

2.1 Introduction

Induced micro-earthquakes happen widely in conventional and unconventional oil/gas fields. Induced seismicity study is of great importance in monitoring and understanding the processes of hydraulic fracturing, fluid injection and oil/gas extraction (Maxwell et al., 2014; Shapiro, 2015). The source mechanism inversion is one of the main areas of the induced seismicity studies. The determination of source mechanisms of induced earthquakes can give the stress and fault orientation in the field (Vavryčuk, 2014).

The source mechanisms of the great majority of tectonic earthquakes can be described by a double-couple (DC), corresponding to a shear fracture. However, some events in volcanic, geothermal, and salt dome areas exhibit more complex source mechanisms with non-DC components, such as volumetric component (ISO) and com-

pensated linear vector dipole (CLVD) (Cespuglio et al., 1996; Panza and Saraò, 2000; Templeton and Dreger, 2006; Nayak and Dreger, 2014). These non-DC components have also been related to mine collapses and nuclear explosions (Ford et al., 2009a,b). Previous research on the analysis of induced seismic events in conventional oil/gas fields assumed a DC source mechanism (Li et al., 2011a,b; Li, 2013). Assuming full moment source mechanisms, Horálek et al. (2010) found a DC-dominated source mechanism of the induced micro-earthquakes in a geothermal area during massive fluid injection. However, recent studies have shown interest in non-DC components of source moment tensors in hydraulic fracturing events (Šílený et al., 2009; Warpinski and Du, 2010; Song and Toksöz, 2011; Song, 2013).

Many studies have implemented the inversion of the full moment tensor by the least-squares (LSQ) method and the regularized LSQ method (Sipkin, 1982; Šílenỳ et al., 1992, 1996). However, LSQ methods have disadvantages in estimating and interpreting the uncertainty of the moment tensor solutions, since the LSQ methods only search for the best moment tensor solution and do not give the probability distributions of the solution. An important question for full moment tensor inversion is whether the non-DC components are real. Some research has applied an F-test to check the significance of the non-DC components (Templeton and Dreger, 2006; Šílený et al., 2009; Horálek et al., 2010; Nayak and Dreger, 2014). LSQ methods do allow a limited uncertainty quantification, based on the Hessian of the misfit function near the LSQ point estimate. But this is only a local and linearized estimate of uncertainty, and can be difficult to interpret in the regularized case. Alternatively, to address the uncertainties of moment tensors resulting from the data noise or imperfect station coverage, many LSQ-based moment tensor inversion studies have applied re-sampling methods to the data, such as Monte Carlo noise realization methods and jackknife tests (Šílený et al., 2009; Stierle et al., 2014a,b). The uncertainties of the moment tensor results were obtained by statistically analyzing the solutions from the resampled data. Du and Warpinski (2011) theoretically derived the uncertainty of the focal plane solutions of seismic sources due to Gaussian noise contamination. In addition, to estimate the uncertainties from earthquake mislocation and velocity mismodeling,

some research has observed the effects of mislocation and velocity mismodeling on the moment tensor solutions by performing location and/or velocity model perturbation tests (Stierle et al., 2014a,b). These tests only show how much the inverted parameter changes with the particular changes of earthquake location and velocity model. They did not actually give the statistical uncertainties of the inverted parameters. In addition, Nayak and Dreger (2014) assessed the sensitivity of the moment tensor and location together by statistically analyzing all the feasible moment tensor and location solutions with a variance reduction larger than a threshold. This method actually provides better estimates of the uncertainties of moment tensor and location solutions. The problem is that it is hard to illustrate how to choose a threshold, and why one should choose a threshold of a certain value.

Compared to LSQ methods, Bayesian inversion methods have the advantages of quantifying the uncertainties of model parameters by characterizing a posterior probability distribution over the parameter space (Tarantola, 2005; Kaipio and Somersalo, 2006; Stuart, 2010). Some studies have conducted Bayesian moment tensor inversion on moderate and large earthquakes. Duputel et al. (2012) introduced a Bayesian moment tensor inversion method to estimate the uncertainties of source mechanisms for large earthquakes ($M_w \geq 6.0$) using W phase waveforms from a global seismic network. That study did not determine the uncertainty of seismic locations jointly with the moment tensor. A very recent paper by Mustać and Tkalčić (2016) has developed a Bayesian full moment tensor inversion for a moderate-size earthquake with a well-studied source mechanism using a regional seismic network. In that research, both the uncertainty of seismic location and moment tensor have been studied by implementing an outer Markov chain to sample the location parameters, and an inner chain to sample the moment tensor parameters.

In this study, we introduce a waveform-based Bayesian full moment tensor inversion method. Both the uncertainties of seismic moment tensor and location are analyzed. Unlike the Bayesian method implemented by Mustać and Tkalčić (2016), we sample the source location and the moment tensor parameters using a single Markov chain; this approach reduces computational cost and provides more accu-

rate uncertainty estimates, particularly for the source location. Moreover, we use the conditionally Gaussian structure of the parameter posterior to solve portions of the inverse problem analytically, reducing the dimension of the sampling problem and allowing the impact of source location uncertainty on moment tensor uncertainty to be explicitly quantified. We first validate the method using synthetic data before applying this full moment tensor inversion method to a selected induced event in an oil/gas field in Oman (Figure 2-1). We determine the full moment tensor of the induced seismicity from a conventional oil/gas field. The seismicity of this field and source mechanisms of events using DC assumptions have been studied extensively (Sarkar, 2008; Li et al., 2011a,b). To better quantify the uncertainties, we used the newly developed waveform-based Bayesian method for full moment tensor inversion, source relocation, and uncertainty quantification.

2.2 Methodology

2.2.1 Full moment tensor and waveform modeling

The source mechanisms of a seismic event can be represented by a 3 by 3 symmetric matrix $\boldsymbol{M}$,

$$\boldsymbol{M} = \begin{bmatrix} M_{11} & M_{12} & M_{13} \\ M_{21} & M_{22} & M_{23} \\ M_{31} & M_{32} & M_{33} \end{bmatrix} \tag{2.1}$$

where each element of the matrix presents a force couple (Figure 2-2). $\boldsymbol{M}$ is the full moment tensor representation of a seismic source mechanism. Figure 2-2b shows three examples of different source mechanisms with their full moment tensor matrix representation, physical presentations, and beach ball presentations.

The matrix $\boldsymbol{M}$ can be converted to fault plane solutions, which are very important for analyzing and interpreting the induced seismicity. The following equations define

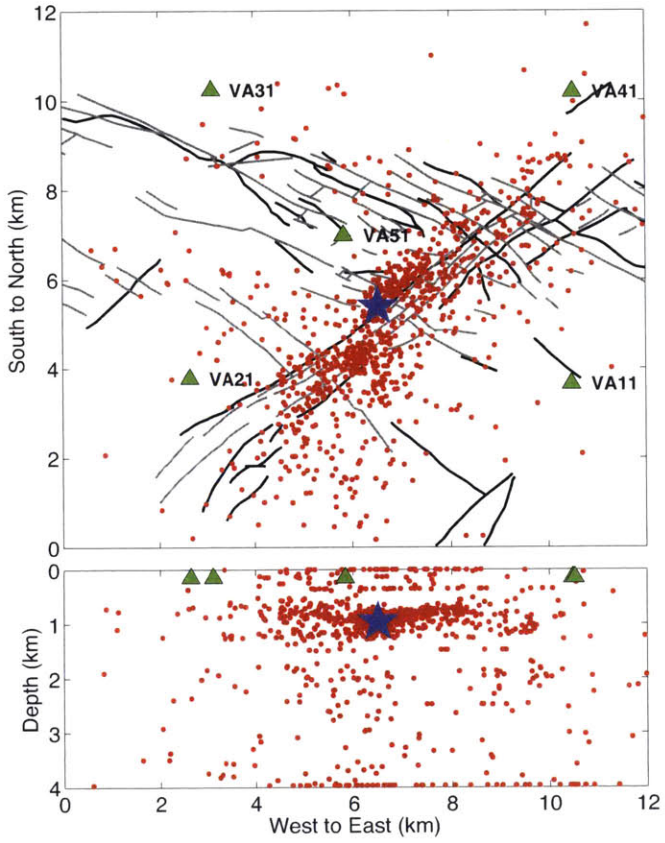

Figure 2-1: Map view and side view of the stations and located events for both near-surface network and downhole network (Sarkar 2008). The red dots denote the location of the detected events, and the green triangles show the location of the stations. The black lines are the identified faults. The green triangles (VA11, VA21, VA31, VA41, and VA51) are the five near-surface stations. These stations are located in shallow boreholes 150 m below the surface.

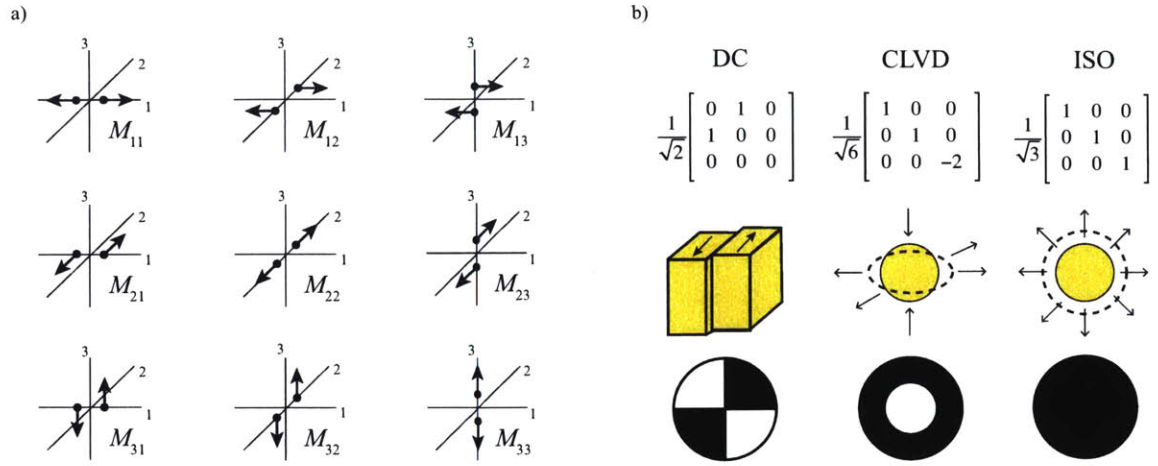

Figure 2-2: a) Graphical description of the $\boldsymbol{M}$ matrix. Each element of the matrix represents a force couple. b) Three examples of source mechanisms. Top: The $\boldsymbol{M}$ matrix of DC, CLVD, and ISO source mechanisms. Middle: The physical representations for three kinds of source mechanisms. Bottom: The beach ball representations of the three source components.

the source-related quantities (Vavryčuk, 2001):

$$\epsilon = -\frac{|\lambda_{min}|}{|\lambda_{max}|}, \tag{2.2}$$

$$M_0 = \frac{1}{\sqrt{2}}\left(\sum_{j=1}^{3}\sum_{k=1}^{3} M_{jk}^2\right)^{\frac{1}{2}}, \tag{2.3}$$

$$ISO = \frac{1}{3}\frac{Tr(m_{jk})}{M_0}, \tag{2.4}$$

$$CLVD = 2\epsilon(1 - |ISO|), \tag{2.5}$$

$$DC = 1 - |ISO| - |CLVD|, \tag{2.6}$$

$$\boldsymbol{u} = \frac{1}{\sqrt{2}}(t + p), \boldsymbol{v} = \frac{1}{\sqrt{2}}(t - p), \tag{2.7}$$

where λ_{min} and λ_{max} are the minimum and maximum eigenvalues of $\boldsymbol{M}$; $\boldsymbol{t}$ and $\boldsymbol{p}$ correspond to the eigenvectors of the maximum and minimum eigenvalues, which indicate the maximum tensile and compressional stress directions; ISO, CLVD, and DC denote the percentages of source components; $\boldsymbol{u}$ is the fracture plane normal vector, and $\boldsymbol{v}$ is the slip vector.

Before performing Bayesian inversion, we must create a forward model that relates

the moment tensor and the location of the seismic source to the observed seismograms. To do so, we first construct a Green's function library, and calculate the synthetic seismograms for a point moment tensor source using the discrete wavenumber integration method (Bouchon, 1981, 2003). The synthetic seismogram $\boldsymbol{v_i^n}$ of the ith component at the nth geophone of location x_r^n is modeled by

$$v_i^n(\boldsymbol{x_r^n}, \boldsymbol{x_s}, t) = \sum_{j=1}^{3}\sum_{k=1}^{3} M_{jk} G_{ij,k}^n(\boldsymbol{x_r^n}, \boldsymbol{x_s}, t) * s(t) + \boldsymbol{e_i^n(t)}, \tag{2.8}$$

where $\boldsymbol{G_{ij,k}(x_r^n, x_s, t)}$ is the spatial derivative of the Green's function of the ith component at the nth geophone of the location $\boldsymbol{x_r^n}$ due to a point moment tensor source of the location $\boldsymbol{x_s}$, $s(t)$ is the source time function, and $\boldsymbol{e_i^n(t)}$ is the noise perturbation of the ith component at the nth geophone. Since $\boldsymbol{M}$ is a symmetric matrix (Figure 2-2), we can simplify $\boldsymbol{M}$ to a vector $\boldsymbol{m}$ of six elementary moment tensor parameters, i.e., $m_1 = M_{11}$, $m_2 = M_{22}$, $m_3 = M_{33}$, $m_4 = M_{12}$, $m_5 = M_{13}$, and $m_6 = M_{23}$. Concatenating all the seismograms and corresponding Green's function matrix (here the Green's function has been convolved with the source time function)

and noise perturbation, we rewrite Equation 2.8 as

$$\begin{bmatrix} \vdots \\ v_i^n(t_0) \\ v_i^n(t_1) \\ \vdots \\ v_i^n(t_T) \\ \vdots \end{bmatrix} = \begin{bmatrix} \vdots & \vdots & \vdots & \vdots & \vdots & \vdots \\ G_{i1,1}^n(t_0) & G_{i2,2}^n(t_0) & G_{i3,3}^n(t_0) & 2G_{i1,2}^n(t_0) & 2G_{i2,3}^n(t_0) & 2G_{i1,3}^n(t_0) \\ G_{i1,1}^n(t_1) & G_{i2,2}^n(t_1) & G_{i3,3}^n(t_1) & 2G_{i1,2}^n(t_1) & 2G_{i2,3}^n(t_1) & 2G_{i1,3}^n(t_1) \\ \vdots & \vdots & \vdots & \vdots & \vdots & \vdots \\ G_{i1,1}^n(t_T) & G_{i2,2}^n(t_T) & G_{i3,3}^n(t_T) & 2G_{i1,2}^n(t_T) & 2G_{i2,3}^n(t_T) & 2G_{i1,3}^n(t_T) \\ \vdots & \vdots & \vdots & \vdots & \vdots & \vdots \end{bmatrix} \begin{bmatrix} m_1 \\ m_2 \\ m_3 \\ m_4 \\ m_5 \\ m_6 \end{bmatrix} + \begin{bmatrix} \vdots \\ e_i^n(t_0) \\ e_i^n(t_1) \\ \vdots \\ e_i^n(t_T) \\ \vdots \end{bmatrix}. \tag{2.9}$$

Finally, Equation 2.9 is simplified as

$$\boldsymbol{d} = \boldsymbol{G}(\boldsymbol{x})\boldsymbol{m} + \boldsymbol{e}, \boldsymbol{x} \in \mathbb{R}^3, \boldsymbol{m} \in \mathbb{R}^6 \tag{2.10}$$

where $\boldsymbol{x}$ denotes the source location $\boldsymbol{x_s}$ in Equation 2.8, $\boldsymbol{d}$ is the concatenation of all the waveform vectors $\boldsymbol{v_i^n}$, $\boldsymbol{G}(\boldsymbol{x})$ is the concatenation of all the synthetic seismograms of six elementary moment tensor parameters, and $\boldsymbol{e}$ is the concatenation of all the noise vectors. The objective of the Bayesian inversion is to predict parameters $\boldsymbol{m}$ and $\boldsymbol{x}$ in Equation 2.10 and quantify their uncertainties based on the waveform data $\boldsymbol{d}$.

2.2.2 Bayesian formulation: prior, likelihood, and posterior

We apply Bayes' rule to the parameters $\boldsymbol{m}$ and $\boldsymbol{x}$ given data $\boldsymbol{d}$

$$P(\boldsymbol{m}, \boldsymbol{x}|\boldsymbol{d}) = \frac{P(\boldsymbol{d}|\boldsymbol{m}, \boldsymbol{x})\pi_0(\boldsymbol{x})\pi_0(\boldsymbol{m})}{P(\boldsymbol{d})}, \tag{2.11}$$

where $\pi_0(\boldsymbol{m})$ and $\pi_0(\boldsymbol{x})$ are the prior probability density of moment tensor $\boldsymbol{m}$ and location $\boldsymbol{x}$, $P(\boldsymbol{d}|\boldsymbol{m},\boldsymbol{x})$ is the likelihood function, $P(\boldsymbol{d})$ is the evidence (or the marginal likelihood), and $P(\boldsymbol{m},\boldsymbol{x}|\boldsymbol{d})$ is the posterior probability density.

The priors $\pi_0(\boldsymbol{m})$ and $\pi_0(\boldsymbol{x})$ depend on the information we know about $\boldsymbol{M}$ and $\boldsymbol{x}$. The priors that we use are simply improper uniform probability density functions , i.e., $\pi_0(\boldsymbol{M}) = const$ and $\pi_0(\boldsymbol{x}) = const$. Improper priors are not integrable and are considered particularly "non-informative" (Sivia and Skilling, 2006); they can suceessfully be used in Bayesian inference as long as the posterior distribution is proper, which is guaranteed by the expressions below.

The form of the likelihood function $P(\boldsymbol{d}|\boldsymbol{m},\boldsymbol{x})$ follows directly from equation 2.10, and depends on the probability distribution $P_{\boldsymbol{e}}$ of the additive error $\boldsymbol{e}$

$$P(\boldsymbol{d}|\boldsymbol{m},\boldsymbol{x}) = P_{\boldsymbol{e}}(\boldsymbol{d} - \boldsymbol{G}(\boldsymbol{x})\boldsymbol{m}), \tag{2.12}$$

where $P_{\boldsymbol{e}}$ is the probability density function of $\boldsymbol{e}$, which is a function of the error mean $\mu_{\boldsymbol{e}}$ and the error covariance matrix $\boldsymbol{\Sigma_e}$.

In this paper we assume the error is Gaussian-distributed with zero-mean and covariance $\boldsymbol{\Sigma_e}$

$$\boldsymbol{e} \sim \mathcal{N}(0, \boldsymbol{\Sigma_e}), \tag{2.13}$$

and that $\boldsymbol{\Sigma_e}$ is the diagonal matrix. The error variance of a particular component of seismograms, $(\sigma_i^n)^2$, is the diagonal element of the block related to that seismic component. The error term models any residual variation, including the observation error, and the model inadequacy, i.e. imperfections of Green's function resulting from any neglected physics (Kennedy and O'Hagan, 2001; Kaipio and Somersalo, 2007). With the Gaussian probability distribution of $\boldsymbol{e}$, the likelihood function can be presented as

$$P(\boldsymbol{d}|\boldsymbol{m},\boldsymbol{x}) = \frac{1}{\sqrt{(2\pi)^N \det \boldsymbol{\Sigma_e}}} \exp\left[-\frac{1}{2}\left(\boldsymbol{d} - \boldsymbol{G}(\boldsymbol{x})\boldsymbol{m}\right)^T \boldsymbol{\Sigma_e}^{-1}\left(\boldsymbol{d} - \boldsymbol{G}(\boldsymbol{x})\boldsymbol{m}\right)\right], \tag{2.14}$$

where N is the total number of data samples used for inversion. With the above prior

and likelihood function, we can obtain the joint posterior distribution of $\boldsymbol{m}$ and $\boldsymbol{x}$

$$P(\boldsymbol{m}, \boldsymbol{x}|\boldsymbol{d}) = cP(\boldsymbol{d}|\boldsymbol{m}, \boldsymbol{x}), \tag{2.15}$$

where c is a normalization constant.

2.2.3 Posterior sampling and prediction

A general approach for characterizing the posterior distribution of $\boldsymbol{m}$ and $\boldsymbol{x}$ is the Markov chain Monte Carlo (MCMC) sampling. The Metropolis-Hasting algorithm (Metropolis et al., 1953; Hastings, 1970), a particular kind of MCMC scheme, constructs a Markov chain that asympotically samples from the posterior. We can evaluate the joint posterior density of $\boldsymbol{m}$ and $\boldsymbol{x}$, $P(\boldsymbol{m}, \boldsymbol{x}|\boldsymbol{d})$, up to a normalizing constant, as given in Equation 2.15. Although this is principle sufficient to run an Metropolis-Hastings sampler, the linear dependence on $\boldsymbol{m}$ and nonlinear dependence on $\boldsymbol{x}$ of the Green's function $\boldsymbol{G}(\boldsymbol{x})$ results in a complex joint dependence of the posterior density on $\boldsymbol{m}$ and $\boldsymbol{x}$. Thus a generic MCMC approach will encounter great difficulty: slow mixing, and an inaccurate characterization of the posterior. We instead design two MCMC approaches that makes more careful use of the problem structure.

Direct sampling for $\boldsymbol{m}$ at fixed $\boldsymbol{x}$

For the first approach, we sample $\boldsymbol{m}$ directly from its full conditional distribution $P(\boldsymbol{m}|\boldsymbol{d}, \boldsymbol{x}^*)$ without resorting to MCMC. Since for a given $\boldsymbol{x}^*$ the modeling waveform $\boldsymbol{G}(\boldsymbol{x}^*)\boldsymbol{m}$ depends linearly on $\boldsymbol{m}$, $P(\boldsymbol{m}|\boldsymbol{d}, \boldsymbol{x}^*)$ can be determined analytically:

$$P(\boldsymbol{m}|\boldsymbol{d}, \boldsymbol{x}^*) \sim \mathcal{N}\left(\mu_{\boldsymbol{m}}(\boldsymbol{d}, \boldsymbol{x}^*), \boldsymbol{\Sigma}_{\boldsymbol{m}}(\boldsymbol{d}, \boldsymbol{x}^*)\right) \tag{2.16}$$

$$\mu_{\boldsymbol{m}}(\boldsymbol{d}, \boldsymbol{x}^*) = \left[\boldsymbol{G}^T(\boldsymbol{x}^*)\boldsymbol{\Sigma}_e^{-1}\boldsymbol{G}(\boldsymbol{x}^*)\right]^{-1}\boldsymbol{G}^T(\boldsymbol{x}^*)\boldsymbol{\Sigma}_e^{-1}\boldsymbol{d} \tag{2.17}$$

$$\boldsymbol{\Sigma}_{\boldsymbol{m}}(\boldsymbol{d}, \boldsymbol{x}^*) = \left[\boldsymbol{G}^T(\boldsymbol{x}^*)\boldsymbol{\Sigma}_e^{-1}\boldsymbol{G}(\boldsymbol{x}^*)\right]^{-1}. \tag{2.18}$$

If one wishes to ignore uncertainty in the source location, i.e., to assume a fixed $\boldsymbol{x}^*$, then this approach characterizes uncertainty in the moment tensor $\boldsymbol{m}$ under such an

assumption. But it can also be used as a building block for an approach that jointly characterizes the uncertainty in $\boldsymbol{m}$ and $\boldsymbol{x}$, which we describe next.

Joint marginal-then-conditional sampling

For the second approach, we first obtain the marginal posterior probability distribution $P(\boldsymbol{x}^*|\boldsymbol{d})$ for any given $\boldsymbol{x}^*$

$$P(\boldsymbol{x}^*|\boldsymbol{d}) \propto P(\boldsymbol{d}|\boldsymbol{x}^*) = \int_{-\infty}^{\infty} P(\boldsymbol{d}|\boldsymbol{m}, \boldsymbol{x}^*)\pi_0(\boldsymbol{m})d\boldsymbol{m} \tag{2.19}$$

We substitute for $P(\boldsymbol{d}|\boldsymbol{m}, \boldsymbol{x}^*)$ using Equation 2.14 and obtain

$$\begin{aligned}
P(\boldsymbol{d}|\boldsymbol{x}^*) &= \frac{1}{\sqrt{(2\pi)^N \det \boldsymbol{\Sigma_e}}} \int_{-\infty}^{\infty} \exp\left[-\frac{1}{2}\left(\boldsymbol{d} - \boldsymbol{G}(\boldsymbol{x})\boldsymbol{m}\right)^T \boldsymbol{\Sigma_e}^{-1}\left(\boldsymbol{d} - \boldsymbol{G}(\boldsymbol{x})\boldsymbol{m}\right)\right] d^6\boldsymbol{m} \\
&= \frac{\exp\left[-\frac{1}{2}\sum_{i=1}^{N}\left(\boldsymbol{\Sigma_e}^{-1}\right)_{ii} d_i^2\right]}{\sqrt{(2\pi)^N \det \boldsymbol{\Sigma_e}}} \int_{-\infty}^{\infty} \exp\left[-\frac{1}{2}\sum_{j,k=1}^{6} A_{j,k}m_j m_k + \sum_{j=1}^{6} B_j m_j\right] d^6\boldsymbol{m} \\
&= \frac{\exp\left[-\frac{1}{2}\sum_{i=1}^{N}\left(\boldsymbol{\Sigma_e}^{-1}\right)_{ii} d_i^2\right]}{\sqrt{(2\pi)^N \det \boldsymbol{\Sigma_e}}} \sqrt{\frac{(2\pi)^N}{\det \boldsymbol{A}}} e^{\frac{1}{2}\boldsymbol{B}^T\boldsymbol{A}^{-1}\boldsymbol{B}} \\
&= \frac{\exp\left[-\frac{1}{2}\sum_{i=1}^{N}\left(\boldsymbol{\Sigma_e}^{-1}\right)_{ii} d_i^2\right]}{\sqrt{\det \boldsymbol{\Sigma_e} \det \boldsymbol{A}}} e^{\frac{1}{2}\boldsymbol{B}^T\boldsymbol{A}^{-1}\boldsymbol{B}},
\end{aligned} \tag{2.20}$$

where

$$\boldsymbol{A} = \sum_{i=1}^{N}\left(\boldsymbol{\Sigma_e}^{-1}\right)_{ii} \begin{bmatrix}
G_{i1}^2 & G_{i1}G_{i2} & G_{i1}G_{i3} & G_{i1}G_{i4} & G_{i1}G_{i5} & G_{i1}G_{i6} \\
G_{i2}G_{i1} & G_{i2}^2 & G_{i2}G_{i3} & G_{i2}G_{i4} & G_{i2}G_{i5} & G_{i2}G_{i6} \\
G_{i3}G_{i1} & G_{i3}G_{i2} & G_{i3}^2 & G_{i1}G_{i4} & G_{i1}G_{i5} & G_{i3}G_{i6} \\
G_{i4}G_{i1} & G_{i4}G_{i2} & G_{i4}G_{i3} & G_{i4}^2 & G_{i1}G_{i5} & G_{i4}G_{i6} \\
G_{i5}G_{i1} & G_{i5}G_{i2} & G_{i5}G_{i3} & G_{i5}G_{i4} & G_{i5}^2 & G_{i5}G_{i6} \\
G_{i6}G_{i1} & G_{i6}G_{i2} & G_{i6}G_{i3} & G_{i6}G_{i4} & G_{i6}G_{i5} & G_{i6}^2
\end{bmatrix}, \tag{2.21}$$

and

$$\boldsymbol{B} = \sum_{i=1}^{N} \left(\boldsymbol{\Sigma}_{\boldsymbol{e}}^{-1}\right)_{ii} d_i \begin{bmatrix} G_{i1} \\ G_{i2} \\ G_{i3} \\ G_{i4} \\ G_{i5} \\ G_{i6} \end{bmatrix}. \tag{2.22}$$

This analytical result lets us evaluate the marginal posterior probability density $P(\boldsymbol{x}^*|\boldsymbol{d})$ at any $\boldsymbol{x}^*$ in the region of interest. We can then sample from $P(\boldsymbol{x}^*|\boldsymbol{d})$ using the adaptive Metropolis (AM) MCMC method (Haario et al., 2001). The AM scheme adjusts the covariance matrix of $\boldsymbol{x}$ every n_0 steps through the MCMC chain based on all the previous samples of $\boldsymbol{x}$:

$$C_{n_0}^* = s_d Cov(\boldsymbol{x_0}, \ldots, \boldsymbol{x_{n_0}}) + s_d \epsilon_0 I_d \tag{2.23}$$

where $C_{n_0}^*$ is the updated covariance matrix at step n_0, $\epsilon_0 > 0$, which is a constant to make $C_{n_0}^*$ positive-definite, $d = 3$ which is the dimension of $\boldsymbol{x}$, and $s_d = 2.42/d$.

For each sampled $\boldsymbol{x}^*$, we then sample $\boldsymbol{m}$ based on the full conditional distribution of $\boldsymbol{m}$ (Equation 2.18). This algorithm is called marginal then conditional sampling (MTC) (Fox and Norton, 2015), and effectively yields a single Markov chain that explores $P(\boldsymbol{m}, \boldsymbol{x}|\boldsymbol{d})$. The posterior distribution of $\boldsymbol{m}$ given $\boldsymbol{d}$ can be extracted as

$$P(\boldsymbol{m}|\boldsymbol{d}) = \int P(\boldsymbol{m}|\boldsymbol{x}^*, \boldsymbol{d}) P(\boldsymbol{x}^*|\boldsymbol{d}) d\boldsymbol{x}^*. \tag{2.24}$$

2.3 Synthetic test

To validate our methods, we first applied our Bayesian inversion method to the synthetic data. The configuration of the seismic source and stations was shown in Figure 2-1. The synthetic source is located at $\boldsymbol{x} = [6.4, 5.4, 1.0]$ km. The source mechanism was set to be Strike = 50°, Dip = 40°, Rake = 280°, DC% = 61%, CLVD% = 17%, ISO = 21%, α = 10°. A layer velocity model was used in the synthetic tests (Figure

2-3, lower right). A 10% Gaussian noise was added to the synthetic data. We grid the region around the true location, and pre-calculate the Green's functions for each possible location grid. The finest grid size is 0.1m.

The synthetic vertical component seismogram for the five stations are shown in Figure 2-4. The analytically-obtained marginal posterior probability distribution $P(\boldsymbol{x}|\boldsymbol{d})$ can be computed according to Equation 4.8, the 3D normalized log analytical marginal probability distribution $\log P(\boldsymbol{x}|\boldsymbol{d})$ is shown in Figure 2-5.

We apply two uncertainty quantification procedures – 1) Direct sampling for $\boldsymbol{m}$, with $\boldsymbol{x}$ fixed at the true location; 2) AM MCMC sampling for $P(\boldsymbol{x})$ and marginal-then-conditional sampling for $\boldsymbol{m}$ – to the synthetic data. The MCMC chain of $\boldsymbol{m}$ and the posterior distribution of $\boldsymbol{m}$ for the two procedures are compared in Figure 2-6. The resulting MCMC chain of $\boldsymbol{x}$ is shown in Figure 2-8.

The comparison between the synthetic waveforms and the posterior predicted waveforms is shown in Figure 2-7. We plot the posterior predicted waveforms as the purple shading areas, and the mean predicted waveforms as bold red lines. For Figure 2-7a), the posterior predicted waveforms are calculated using $\boldsymbol{G}(\boldsymbol{x}^*)\boldsymbol{m}$, where $\boldsymbol{G}(\boldsymbol{x}^*)$ is the Green's function at the the fixed location $\boldsymbol{x}^*$ and $\boldsymbol{m}$ is from the direct MCMC sampling. For Figure 2-7b), the posterior predicted waveforms are calculated using $\boldsymbol{G}(\boldsymbol{x}^*)\boldsymbol{m}$, where $\boldsymbol{G}(\boldsymbol{x}^*)$ is the Green's function at the location $\boldsymbol{x}^*$ sampled by the marginal posterior probability distribution $P(\boldsymbol{x}|\boldsymbol{d})$, and $\boldsymbol{m}$ is from the marginal-then-conditional sampling. The mean posterior predicted waveforms are the average of all the posterior predicted waveforms. The comparison of the inverted source mechanism results and true values are shown in Table 2.1. The posterior predicted waveform region (purple areas) are narrow, and the mean posterior predicted waveforms (red lines) matches well with the synthetic data (blue) for both the two procedures.

The uncertainties of the source parameters and location are presented in the same table. We find that uncertainty of location $\boldsymbol{x}$ is small ($< 1\ m$). Although as expected, the standard deviation of source parameters from $P(\boldsymbol{m}|\boldsymbol{d})$ is only slightly larger than those from $P(\boldsymbol{m}|\boldsymbol{d}, \boldsymbol{x}^*)$, the two posterior distributions - $P(\boldsymbol{m}|\boldsymbol{d}, \boldsymbol{x}^*)$ and $P(\boldsymbol{m}|\boldsymbol{d})$ - are also show small differences. This is because, for the synthetic data, the velocity

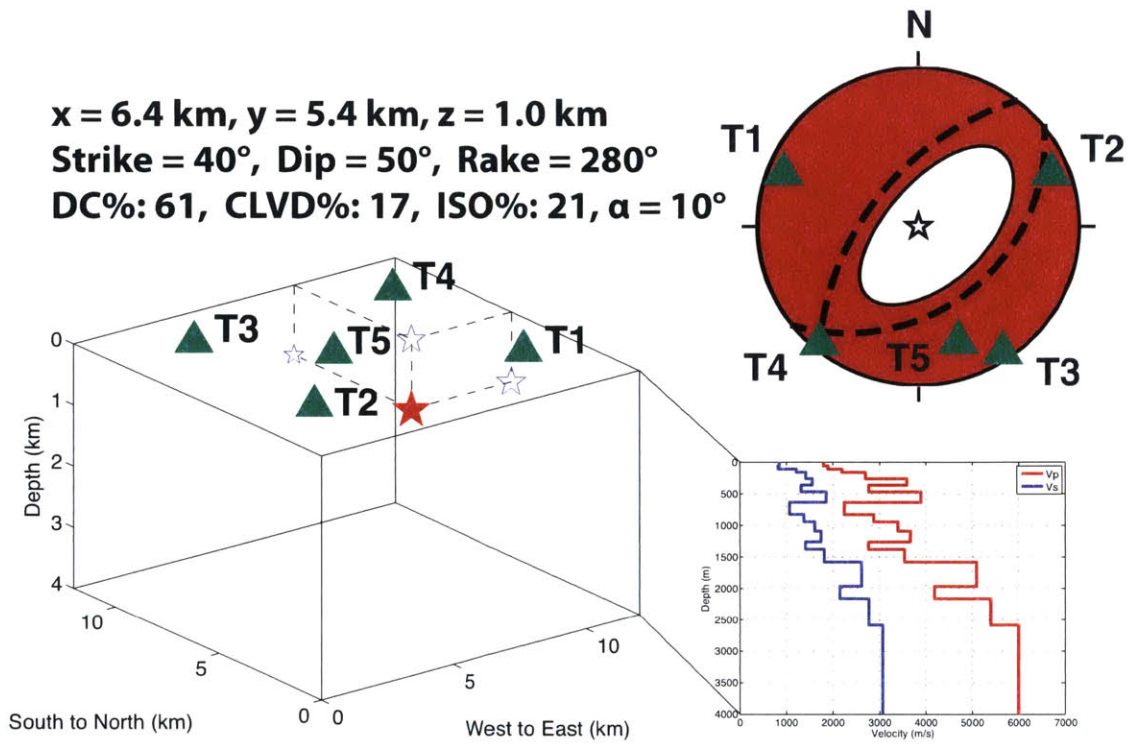

Figure 2-3: The configuration of source and stations of our synthetic data. Left: The cube on the left shows the locations of the source and the stations. The red star denotes the source, the green triangles denote the stations. Right: The beach ball on the top right shows the mechanism of the synthetic source. The green triangles denote the projection of the 5 stations on the source focal plane. The velocity model is shown at the bottom right.

model is known, and the forward Green's functions are accurate. The 3D marginal probability distribution $P(\boldsymbol{x}|\boldsymbol{d})$ is very sharp around the true location. The inclusion of variances of other physics into the model would expand the uncertainties of $\boldsymbol{m}$ and $\boldsymbol{x}$, e.g. velocity model. However, in the paper we only consider the uncertainties of $\boldsymbol{m}$ and $\boldsymbol{x}$.

2.4 Results for real data

The data used are from an oil and gas field in the Sultanate of Oman, studied extensively by Sarkar (2008) and Li et al. (2011a,b). The events were located using the NonLinLoc algorithm, which utilizes a probabilistic, nonlinear, global-search earth-

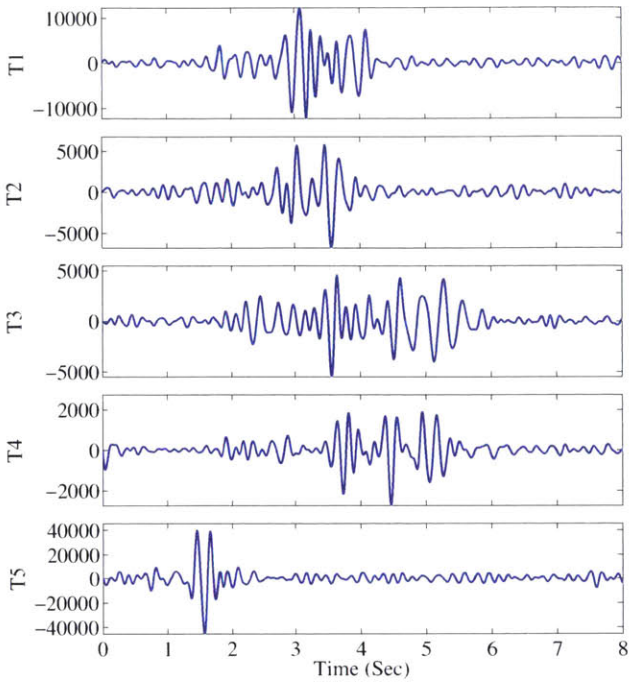

Figure 2-4: The synthetic vertical component seismograms from the five stations.

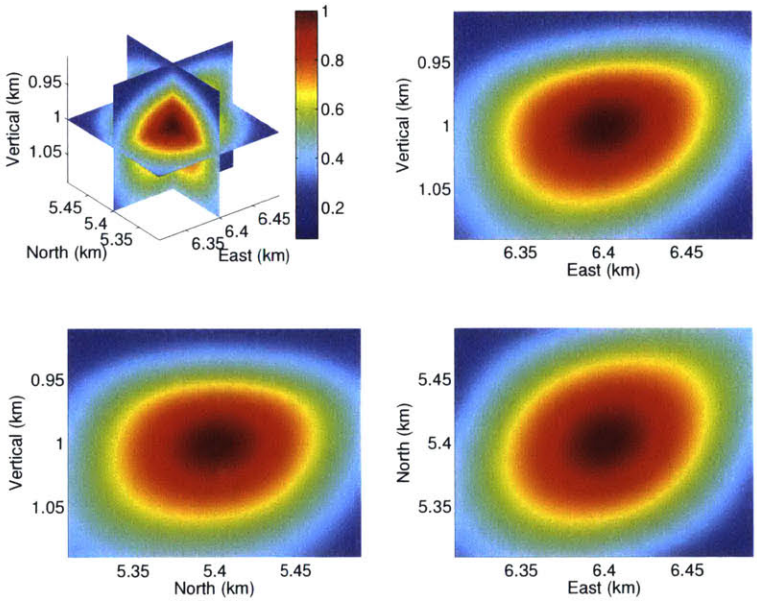

Figure 2-5: The normalized analytically-obtained log marginal likelihood in the 3D space around the true location.

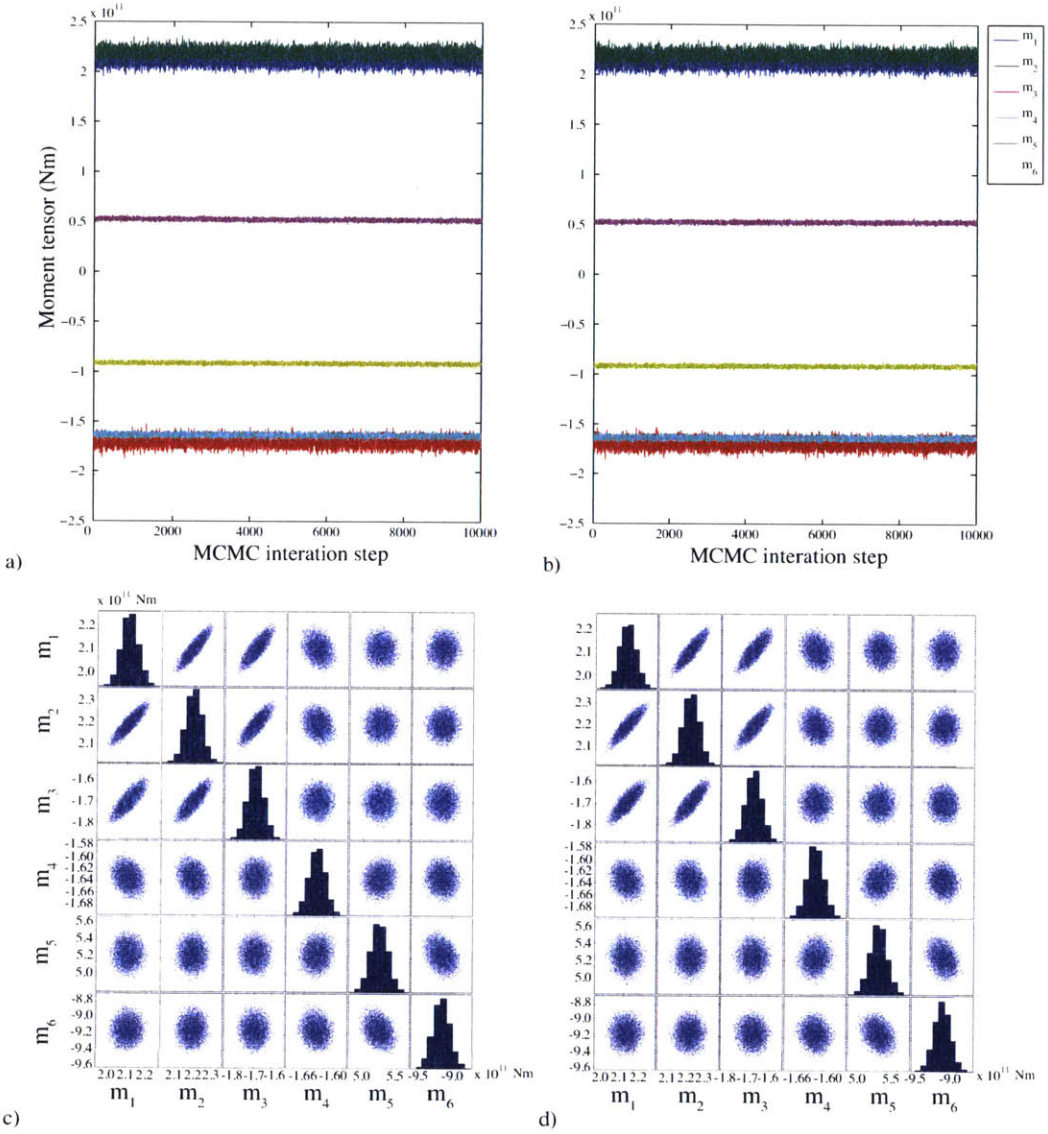

Figure 2-6: a) The MCMC chain of $\boldsymbol{m}$ from direct sampling of $\boldsymbol{m}$ and grid search for $\boldsymbol{x}$ at the true location $\boldsymbol{x} = [6.4, 5.4, 1.0]$. b) The MCMC chain of $\boldsymbol{m}$ from direct sampling of $\boldsymbol{m}$ for $\boldsymbol{x}$ sampled from the marginal posterior distribution $P(\boldsymbol{x}|\boldsymbol{d})$. c) The full conditional distribution of $\boldsymbol{m}$ at the true location $\boldsymbol{x} = [6.4, 5.4, 1.0]$. d) The posterior distribution of $\boldsymbol{m}$ from joint sampling of $P(\boldsymbol{m}, \boldsymbol{x}|\boldsymbol{d})$.

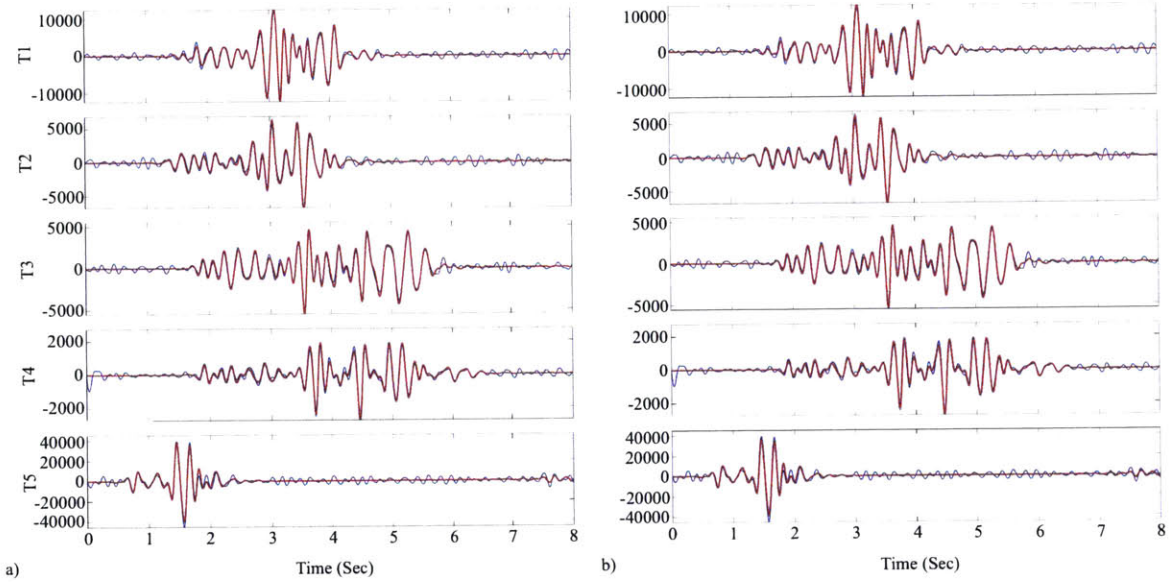

Figure 2-7: The comparison of the mean posterior predicted (red) and synthetic (blue) seismograms. The purple shading areas (very narrow) show the 10^4 posterior predicted waveforms. All the seismograms are bandpass filtered between 3Hz an 8Hz. a) The posterior predicted waveforms are based the direct sampling of $\boldsymbol{m}$ at the true location $\boldsymbol{x} = [6.4, 5.4, 1.0]$. b) The posterior predicted waveforms are based on the Green's function at $\boldsymbol{x}$ sampled from the marginal posterior distribution $P(\boldsymbol{x}|\boldsymbol{d})$ and $\boldsymbol{m}$ from joint sampling of $P(\boldsymbol{m}, \boldsymbol{x}|\boldsymbol{d})$.

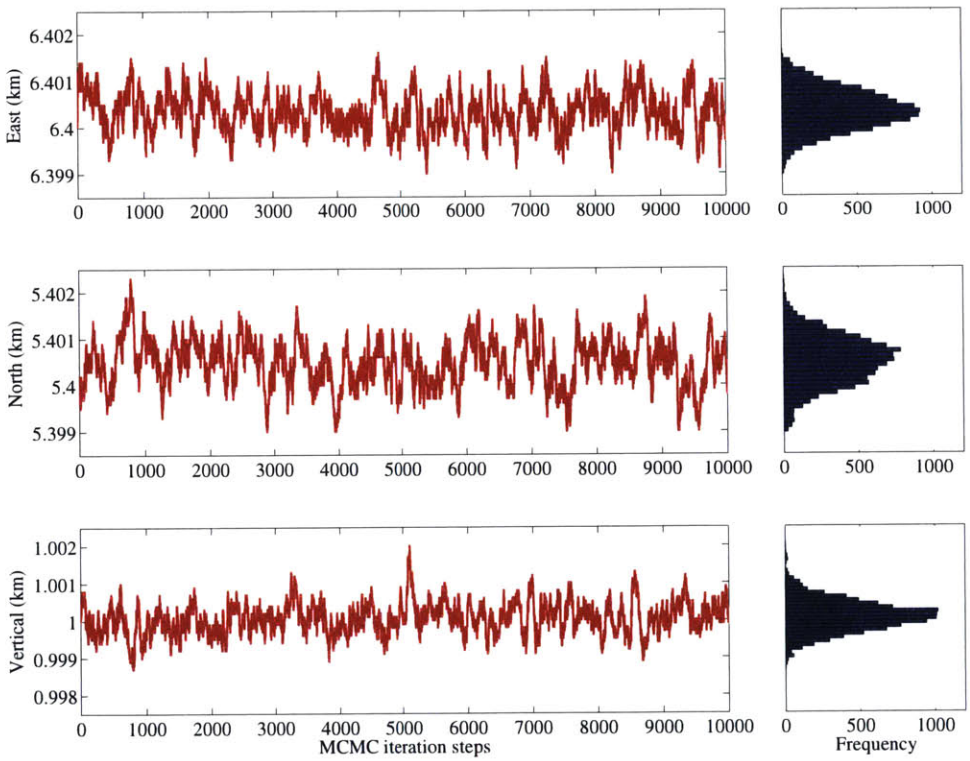

Figure 2-8: Left: The MCMC chain of $\boldsymbol{x}$ from AM MCMC sampling. Right: The histogram of $\boldsymbol{x}$ from 10^4 AM samples.

Table 2.1: The source mechanism results for the synthetic event

		Direct sampling for $\boldsymbol{m}$ for the fixed $\boldsymbol{x}$		Gibbs sampling for $\boldsymbol{m}$ *AM* MCMC for $\boldsymbol{x}$	
	True value	Mean	Standard deviation	Mean	Standard deviation
E (km)	6.4	6.4	-	6.4003	0.0004
N (km)	5.4	5.4	-	5.4005	0.0005
Z (km)	1.0	1.0	-	1.0001	0.0004
$M_0(Nm)$	3.128e+11	3.140e+11	2.366e+09	3.145e+11	2.239e+09
Strike (°)	50	49.4	0.3	49.6	0.3
Dip (°)	40	39.9	0.3	39.4	0.3
Rake (°)	280	279.1	0.4	278.8	0.4
DC (%)	61	61.7	1.0	64.2	1.1
CLVD (%)	17	16.4	0.7	16.8	0.7
ISO (%)	21	21.8	0.8	18.9	0.9
α (°)	10	9.6	0.4	9.5	0.4

*The first Mean for x=(E,N,Z) is the fixed location $\boldsymbol{x}$ from the true value.

quake location algorithm (Lomax et al., 2000). The seismicity data are from the surface monitoring network (Figure 2-1). For this network, five surface stations, instrumented with SM-6B geophones, have been set up since 1999. The data used in the Oman studies consist of 800 events located at the surface network. This field is dominated by two fault systems: the northeast-southwest trending main faults and northwest-southeast trending auxiliary system. The accurate and detailed 1D P-wave velocity models are from the sonic logging data (Sarkar, 2008). The S-wave velocity models are from the double-difference tomography results (Zhang et al., 2009).

We selected one event from the surface monitoring network. The data for inversion are the vertical component seismograms from five stations, since the horizontal components are not accurate because of the unknown orientation of seismometers. The whole seismograms are shown in Figure 2-9. We only fit a part of the seismograms from each station. The fitted seismogram contains a P-segment which involves 2 periods before the P-wave arrival and 4 - 8 periods after P-wave arrival, and a S-segment which involves 2 - 6 periods after the S-wave arrival. Independent time-shift for the P- and S-segment for each station is applied before the Bayesian inversion to mitigate the effects of imperfect Green's function (Zhu and Helmberger, 1996).

For the Bayesian inversion, since it is difficult to estimate a true error covariance matrix including both the effects of data noise and model inadequancy, in order to bound the uncertainties we assume a $\boldsymbol{\Sigma_e}$ with large diagonal values (σ equals 10% of the maximum amplitude over all the stations). First we fix the location to be the NonLinLoc location and apply the direct MCMC sampling for $\boldsymbol{m}$. The full moment tensor results and the uncertainties are shown in Figure 2-10. The waveform matching with the variance reduction is presented in the same figure. We plot the posterior predicted waveforms as the purple shading areas, and the mean predicted waveforms as bold red lines. The posterior predicted waveforms are calculated using $\boldsymbol{G}(\boldsymbol{x}^*)\boldsymbol{m}$, where $\boldsymbol{G}(\boldsymbol{x}^*)$ is the Green's function at the the fixed location $\boldsymbol{x}^*$ and $\boldsymbol{m}$ is from the direct MCMC sampling. The mean posterior predicted waveforms are the average of all the posterior predicted waveforms. Second, we apply an AM MCMC sampling for $\boldsymbol{x}$ and a marginal-then-condition sampling for $\boldsymbol{m}$. We show the full moment tensor

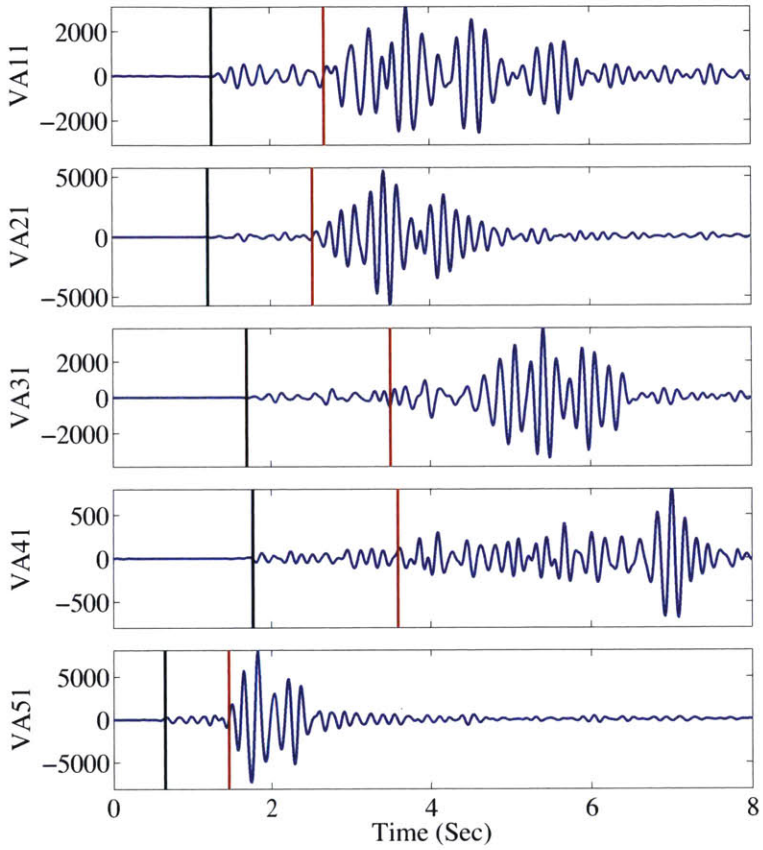

Figure 2-9: The vertical components from five stations for the selected event. All the seismograms are bandpass filtered between 3Hz an 8Hz. The black lines show the arrival time of P waves, and the red lines show the arrival time of S waves.

results, the relative uncertainties, and the waveform matching in Figure 2-12. The posterior predicted waveforms are calculated using $\boldsymbol{G}(\boldsymbol{x})\boldsymbol{m}$, where $\boldsymbol{G}(\boldsymbol{x})$ is the Green's function at the sampled location $\boldsymbol{x}$ and $\boldsymbol{m}$ is from the marginal-then-conditional sampling. The inclusion of the uncertainty of $\boldsymbol{x}$ increased the shading areas of the posterior predicted waveforms, and the uncertainties of the source mechanism results.

The Bayesian source mechanism results with the uncertainties are shown in Table 2.2. The small uncertainties of location are because we assume the velocity model is accurate, and we do not include the uncertainty of velocity models in our Bayesian inversion. We will include the uncertainty of velocity models in our future work. The Bayesian full moment tensor result shows that even considering the uncertainties the strike of the fault plane is close to the directions of the main fault system in this oil/gas field.

2.5 Discussion

The Bayesian moment tensor inversion method works well for recovering the source mechanisms and location from the seismograms; this is validated by our synthetic study. In addition, the Bayesian method naturally lets us obtain the uncertainties of the source parameters and location from the posterior distributions of these parameters. The fault geometry and DC component of the MT are determined most accurately. The uncertainty of isotropic and CLVD components is relatively larger than those of the DC components.

Based on the synthetic simulation and the study of an induced seismic event from an oil/gas field, we can state that the uncertainty quantification of full moment tensor solutions is a powerful tool to estimate how reliable the source mechanism model is.

This study does not include the uncertainty of the velocity model. We expect that the inclusion of velocity uncertainties, in future work, will broaden the uncertainties of the both moment tensor and location solutions and provide more realistic uncertainty bounds.

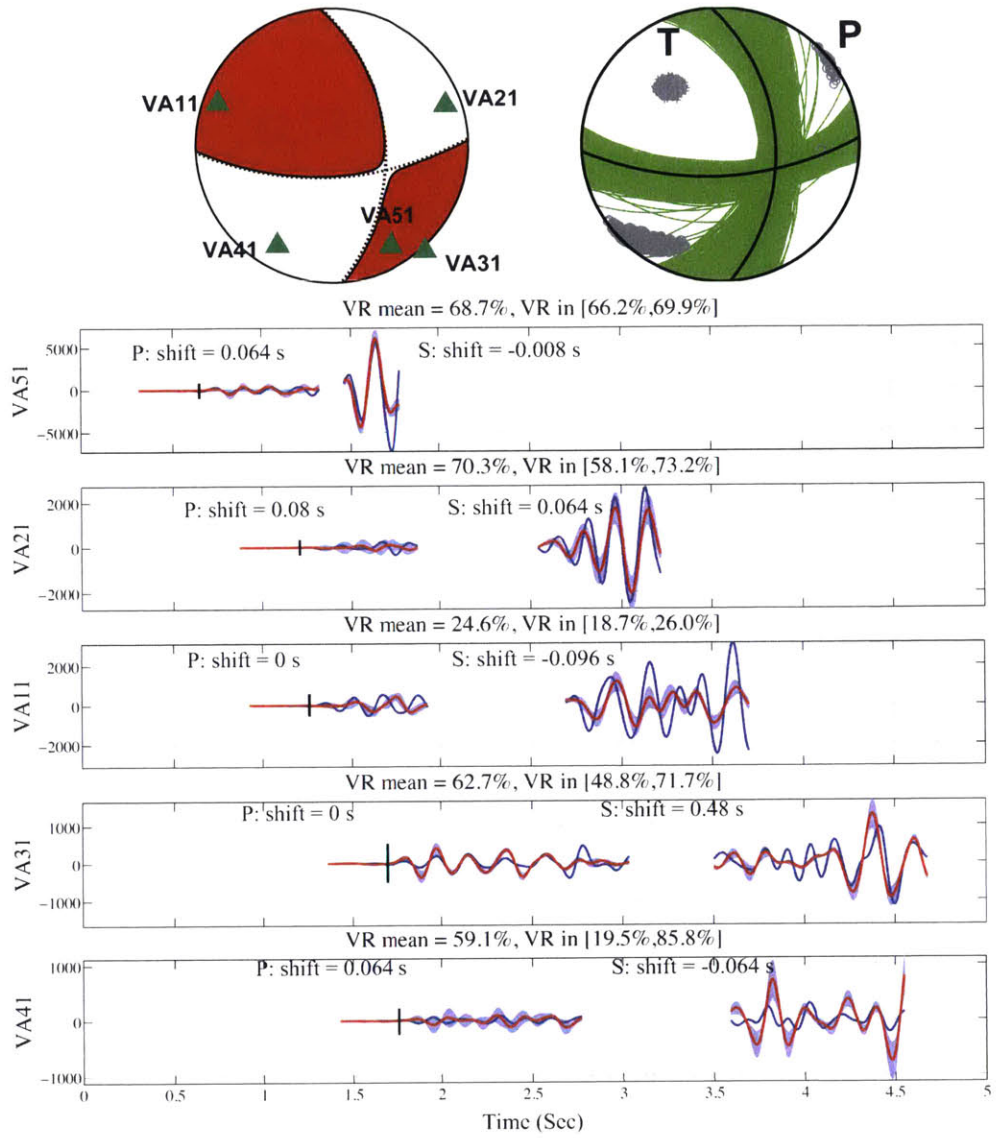

Figure 2-10: Top left: The focal plane projection of the mean value of the source mechanism from direct sampling of $\boldsymbol{m}$ at the fixed $\boldsymbol{x}$ from initial NonLinLoc location. The dashed line shows the mean value of the fault plane solutions. The green triangles denote the five stations. Top right: The green region shows the uncertainty of the fault plane solutions and the tensile and compressional stress from direct sampling of $\boldsymbol{m}$ at the fixed $\boldsymbol{x}$ from initial NonLinLoc location. Bottom: The comparison of the mean posterior predicted (red) and real (blue) data for the separated P- and S-wave segments. The purple shading areas show the 10^4 posterior predicted waveforms. The mean and range of the variance reduction (VR) for each station is shown in the figure.

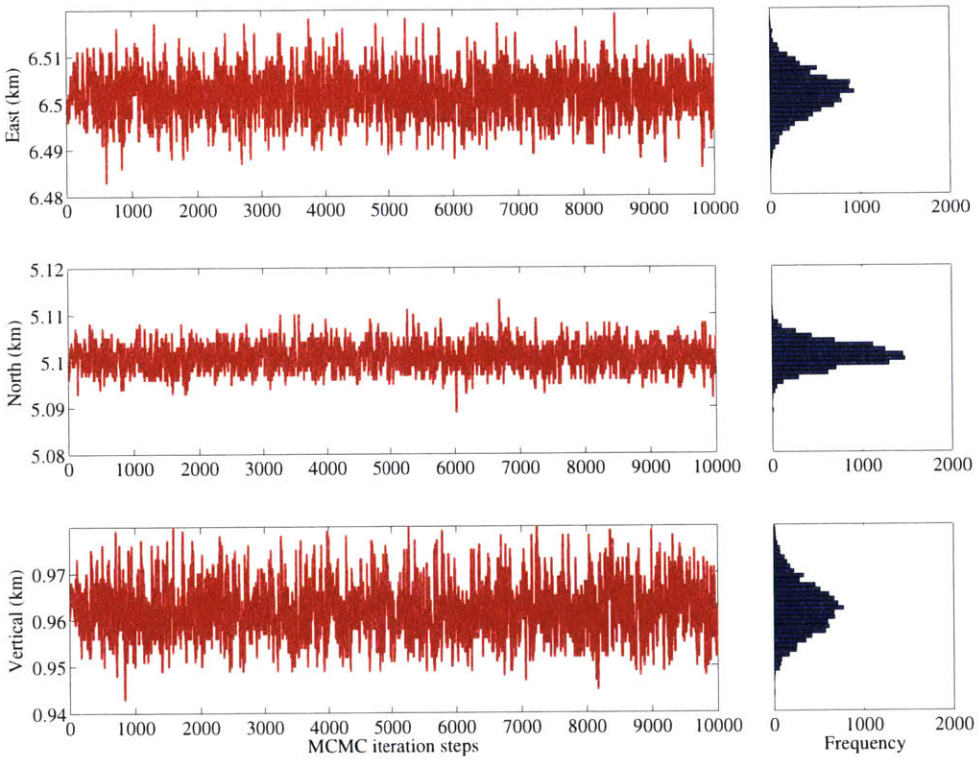

Figure 2-11: Left: The MCMC chain of $\boldsymbol{x}$ from AM MCMC sampling. Right: The histogram of $\boldsymbol{x}$ from 10^4 AM samplings.

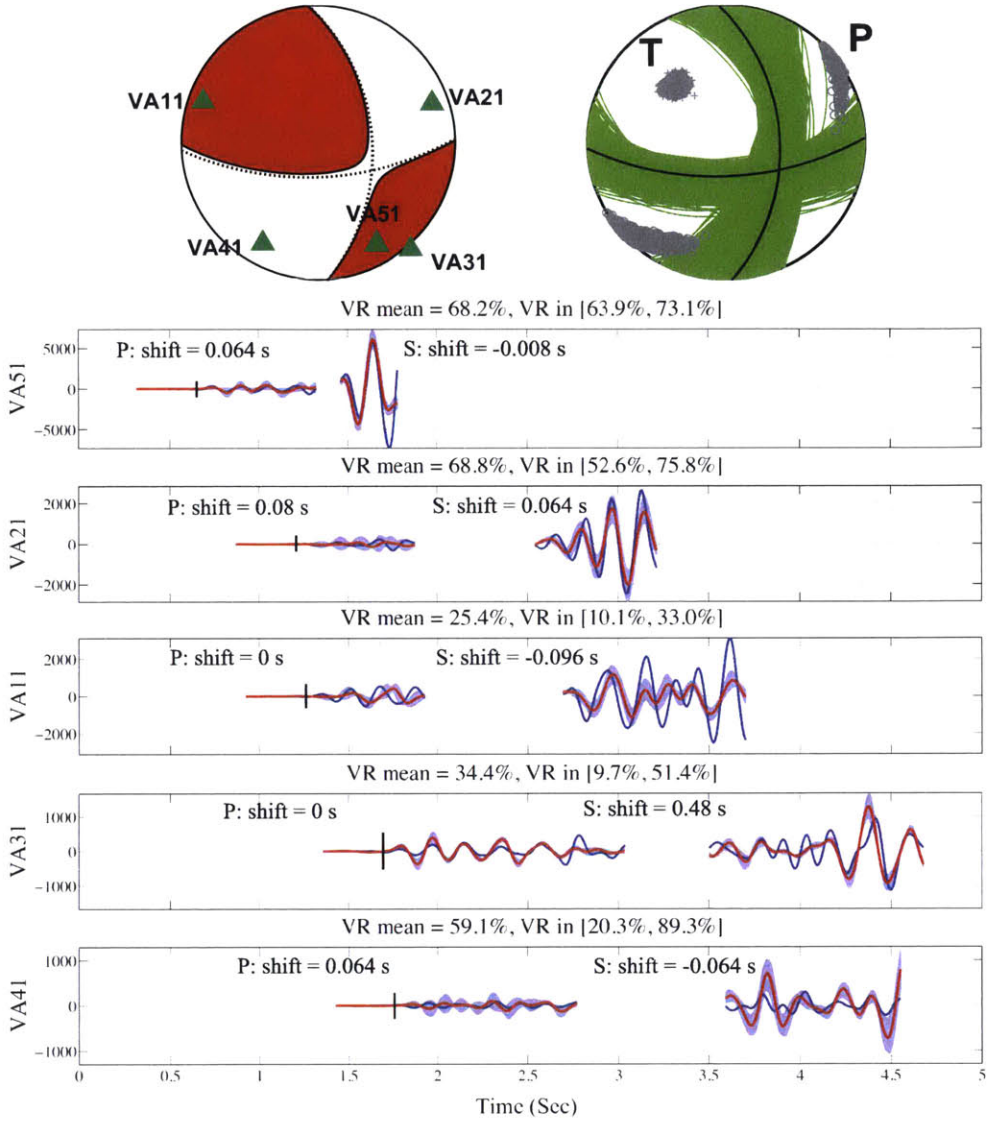

Figure 2-12: Top left: The focal plane projection of the mean value of the source mechanism from marginal-then-conditional sampling of $\boldsymbol{m}$ at each $\boldsymbol{x}$ from AM MCMC sampling. The dashed line shows the mean value of the fault plane solutions. The green triangles denote the five stations. Top right: The green region shows the uncertainty of the fault plane solutions and the gray dots and crosses show the tensile and compressional stress from marginal-then-conditional sampling of $\boldsymbol{m}$. Bottom: The comparison of the mean posterior predicted (red) and real (blue) data for the separated P- and S-wave segments. The purple shading areas show the 10^4 posterior predicted waveforms. The mean and range of the variance reduction (VR) for each station is shown in the figure.

Table 2.2: The source mechanism results of the real event 20010035

	Direct sampling for $\boldsymbol{m}$ for the fixed $\boldsymbol{x}$		Gibbs sampling for $\boldsymbol{m}$ *AM* MCMC for $\boldsymbol{x}$	
	Mean	Standard deviation	Mean	Standard deviation
E (km)	6.50	-	6.5018	0.0047
N (km)	5.10	-	5.1008	0.0027
Z (km)	0.97	-	0.9619	0.0055
M_0	4.3967e+10	1.6907e+09	5.9863e+10	4.6811e+09
Strike (°)	87.3	3.2	87.9	4.1
Dip (°)	63.8	3.9	62.8	5.1
Rake (°)	40.1	4.6	38.8	6.3
DC (%)	56.8	13.3	55.9	13.3
CLVD (%)	48.1	12.2	30.7	12.8
ISO (%)	13.4	6.7	12.6	8.3
α (°)	16.8	7.9	17.5	8.2

*The first Mean for x=(E,N,Z) is the initial NonLinLoc location result.

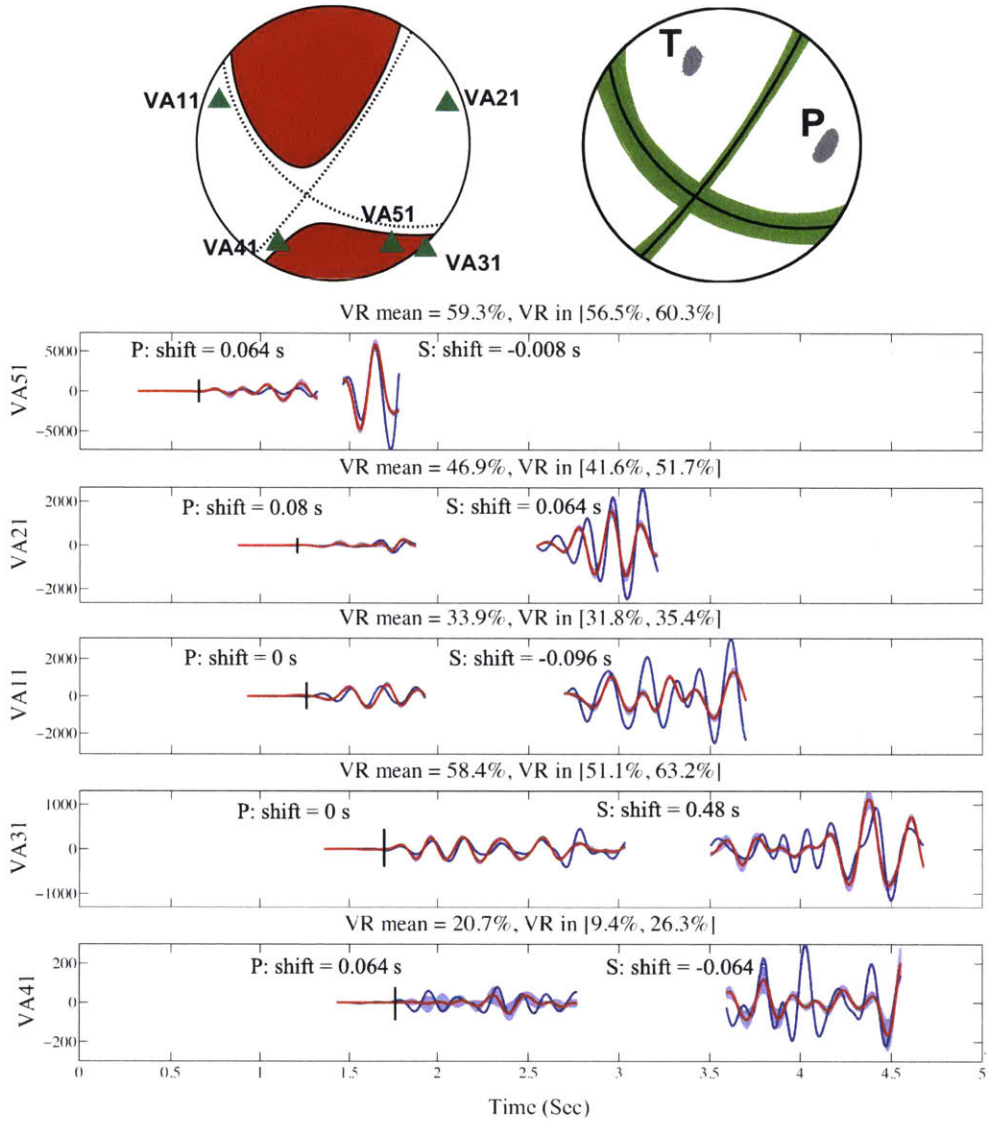

Figure 2-13: Results for non-identical covariance matrix. Top left: The focal plane projection of the mean value of the source mechanism from marginal-then-conditional sampling of $\boldsymbol{m}$ at each $\boldsymbol{x}$ from AM MCMC sampling. The dashed line shows the mean value of the fault plane solutions. The green triangles denote the five stations. Top right: The green region shows the uncertainty of the fault plane solutions and the gray dots and crosses show the tensile and compressional stress from marginal-then-conditional sampling of $\boldsymbol{m}$. Bottom: The comparison of the mean posterior predicted (red) and real (blue) data for the separated P- and S-wave segments. The purple shading areas show the 10^4 posterior predicted waveforms. The mean and range of the variance reduction (VR) for each station is shown in the figure.

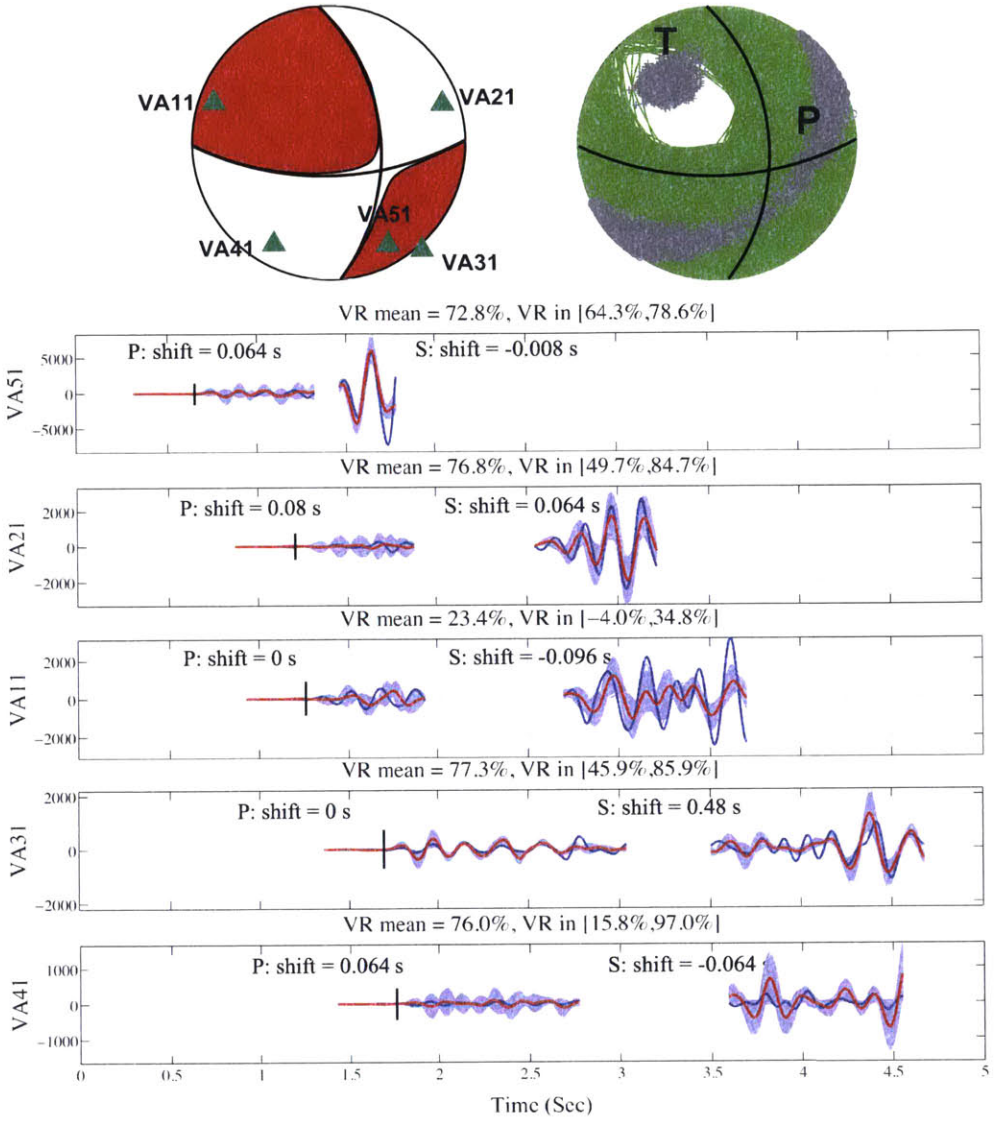

Figure 2-14: Results for 20% Gaussian noise. Top left: The focal plane projection of the mean value of the source mechanism from marginal-then-conditional sampling of $\boldsymbol{m}$ at each $\boldsymbol{x}$ from AM MCMC sampling. The dashed line shows the mean value of the fault plane solutions. The green triangles denote the five stations. Top right: The green region shows the uncertainty of the fault plane solutions and the gray dots and crosses show the tensile and compressional stress from marginal-then-conditional sampling of $\boldsymbol{m}$. Bottom: The comparison of the mean posterior predicted (red) and real (blue) data for the separated P- and S-wave segments. The purple shading areas show the 10^4 posterior predicted waveforms. The mean and range of the variance reduction (VR) for each station is shown in the figure.

Chapter 3

Ground Motion Modeling and Source Mechanism of Regional and Local Earthquakes in Kuwait

3.1 Introduction

Kuwait is affected by two different kinds of earthquakes, regional tectonic earthquakes and smaller local earthquakes. The tectonic earthquakes occurred mostly in the Zagros region and surrounding areas. To monitor these earthquakes, Kuwait initiated the Kuwait National Seismograph Network (KNSN) in 1997, which consisted of seven three-component short-period stations (AB, MI, QR, RD, RS, SA, UM) and one three-component broadband station (KB), in operation from 1997 to 2013. Since the year 2013, the KNSN upgraded the seismic monitoring network by replacing five short-period stations (MI, QR, RD, RS, UM) with broadband stations.

Figure 3-1 shows the significant regional earthquakes around Kuwait in the period 1997-2016. On average, about one earthquake of magnitude 6 or greater occurs in the region each year. From the seismograms recorded from the station MI, we noted most of them have long duration surface waves. To estimate the effects of these regional earthquakes on structures, we applied the pseudo displacement spectral analysis to

a 08/18/2014 Mw 6.2 earthquake which happened at the Iran-Iraq border 200 km NNE of Kuwait city and was widely felt in Kuwait. We show the three-component seismograms and the pseudo displacement response spectra of this earthquake in Figure 3-2. The peak response periods occurred at 3.4 s, 5.7 s, 6.9 s, and 16.0 s. The long period (16 s) peak shown is due to Love waves that are recorded on E-W component.

One experiment has been done by the Kuwait Institute for Scientific Research (KISR) to record the ambient vibration at the top terrace of the Al-Hamra Tower, using two Kinemetrics systems (3 component Episensor accelerometer and Q330 data logger). We show the ambient vibration spectra of the Al-Hamra Tower on day 329 of the year 2013 in Figure 3-3. The ambient vibration peak periods - 3.3 s, 5.7 s, and 7.1 s - obtained from two instruments, each with three components, are quite consistent. These values are close to the periods of the peak pseudo displacement response spectra – 3.4 s, 5.7 s, and 6.9 s. From the observed ground motion and building ambient noise measurements, we can conclude that potential damaging ground vibrations to the tall buildings could occur due to regional earthquakes.

Local earthquakes in Kuwait occur more frequently. Since 1997, the KNSN has recorded more than 1000 earthquakes (Mw < 5). Most of the local earthquakes are distributed close to the oil/gas fields in the northeast and southwest of Kuwait (Figure 3-4), probably induced by oil production activities. Two large local earthquakes - Mw 4.5 in 03/21/2015 and Mw 4.1 in 08/18/2015 - have been recorded by both the Incorporated Research Institutions for Seismology (IRIS) and KNSN. The seismograms of the Mw 4.5 earthquake from three selected stations and the corresponding pseudo displacement response spectra are shown in Figure 3-5. The peak response periods are in the range of from 1 s to 2 s.

We compare the pseudo displacement response spectra for the Mw 6.2 regional earthquake from MI and the Mw 4.5 local earthquake from RQ in Figure 3-6. The reason we choose these two stations is that MI is the closest station to the hypocenter of the Mw 6.2 earthquake, and RQ is the closest station to the hypocenter of the Mw 4.5 earthquake. Thus, we can compare the maximum observed response spectra of the

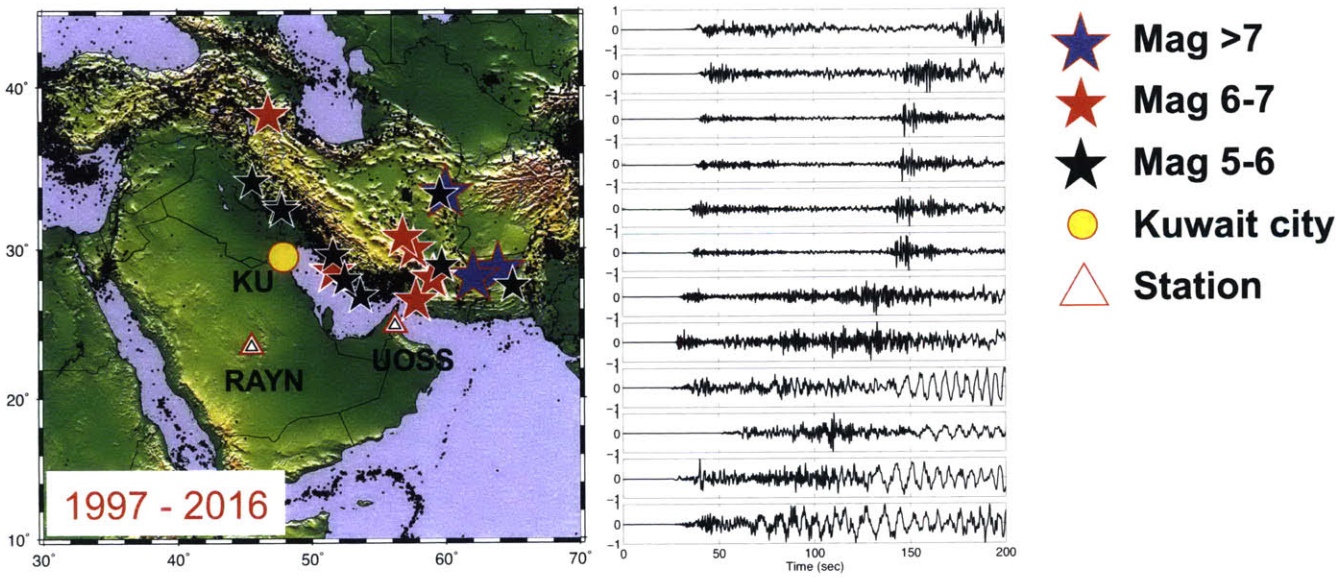

Figure 3-1: Significant regional earthquakes since 1997 affecting tall buildings in Kuwait. Seismograms are recorded by the broadband station MIB in Kuwait.

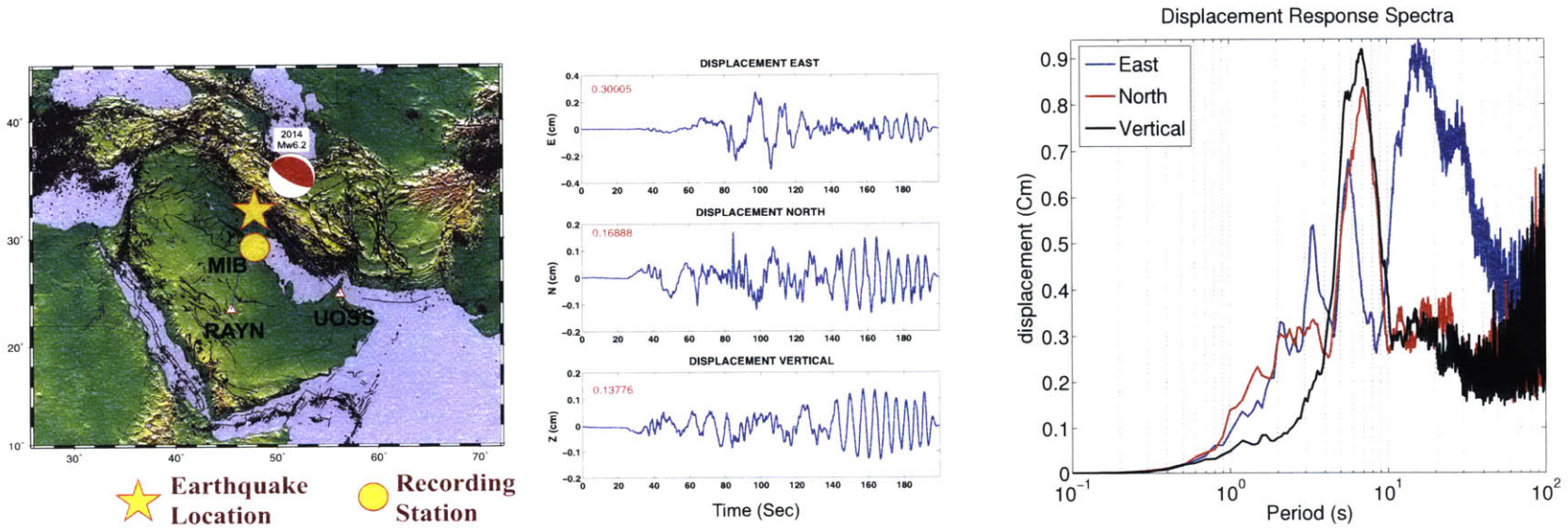

Figure 3-2: This 2014/08/18Mw 6.2 earthquake was widely felt in Kuwait. The red beach ball shows the mechanism and the observed (blue) seismograms at MIB in Kuwait are in the middle. The response spectra of displacement and acceleration are plotted on the right.

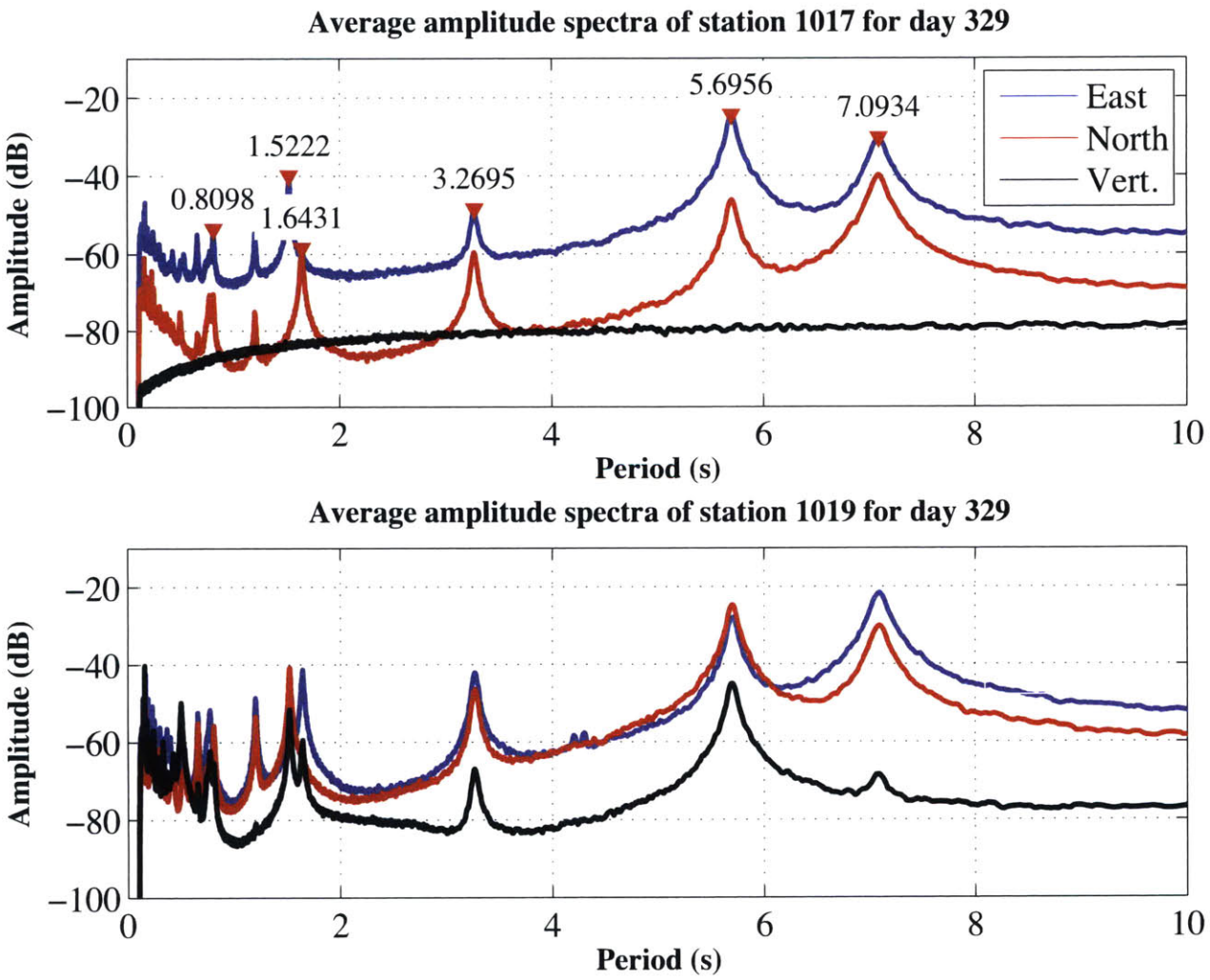

Figure 3-3: Left: Amplitude spectra, calculated using ambient noise data recorded by two Kinemetrics EpiSensor instruments, at the top of the Al-Hamra Tower. Average spectra for the day 329 of year 2014 (computed with a 600 s moving window). The station 1017 did not work well. The vertical component of station 1017 does not receive any meaningful signal, and the two horizontal components were not calibrated well.

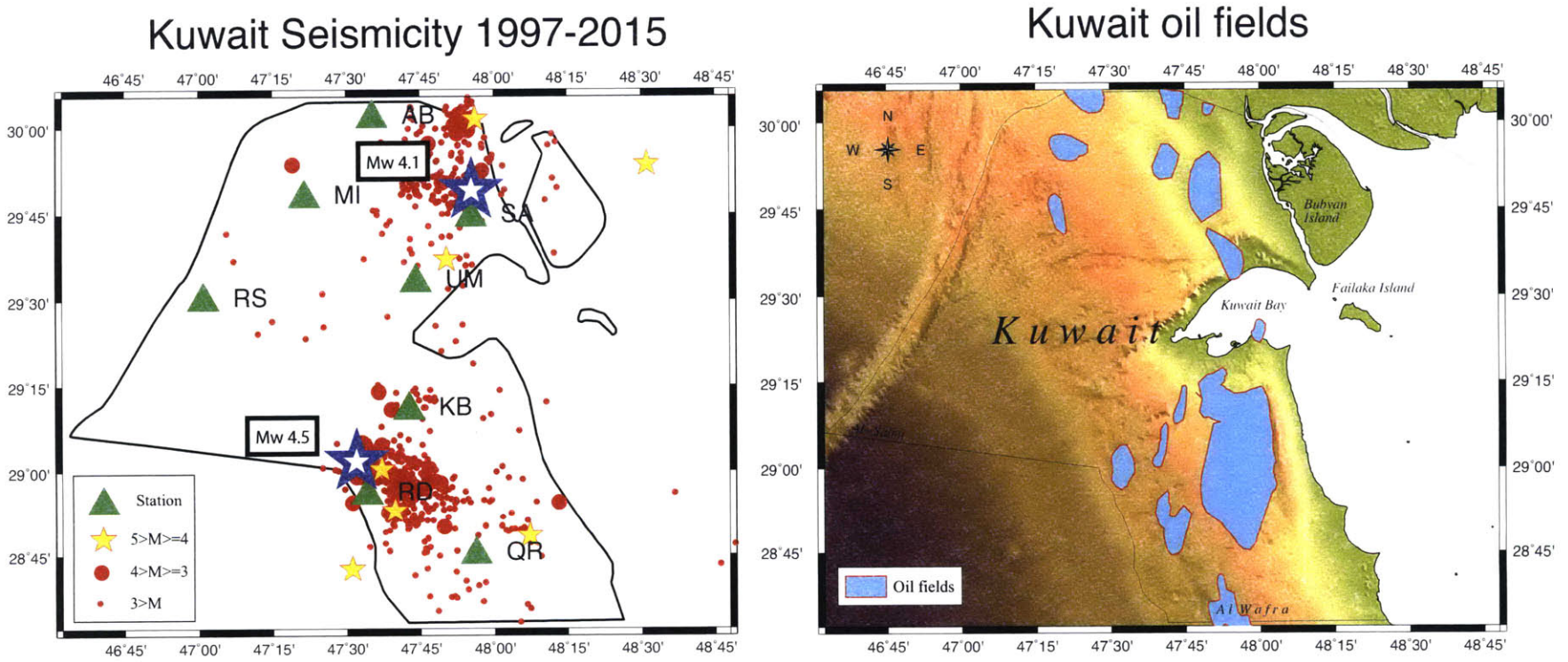

Figure 3-4: Left: Local earthquakes in Kuwait during 1997-2015. The small red circles denote the $M < 3$ earthquakes, the large red circles denote the $4 > M \geq 3$, and the yellow stars with red edges denote the $5 > M \geq 4$ earthquakes. The two largest local events (03/21/2015 Mw = 4.1 and 08/18/2015 Mw = 4.5), shown by white stars, occurred in 2015. Right: Oil fields in Kuwait.

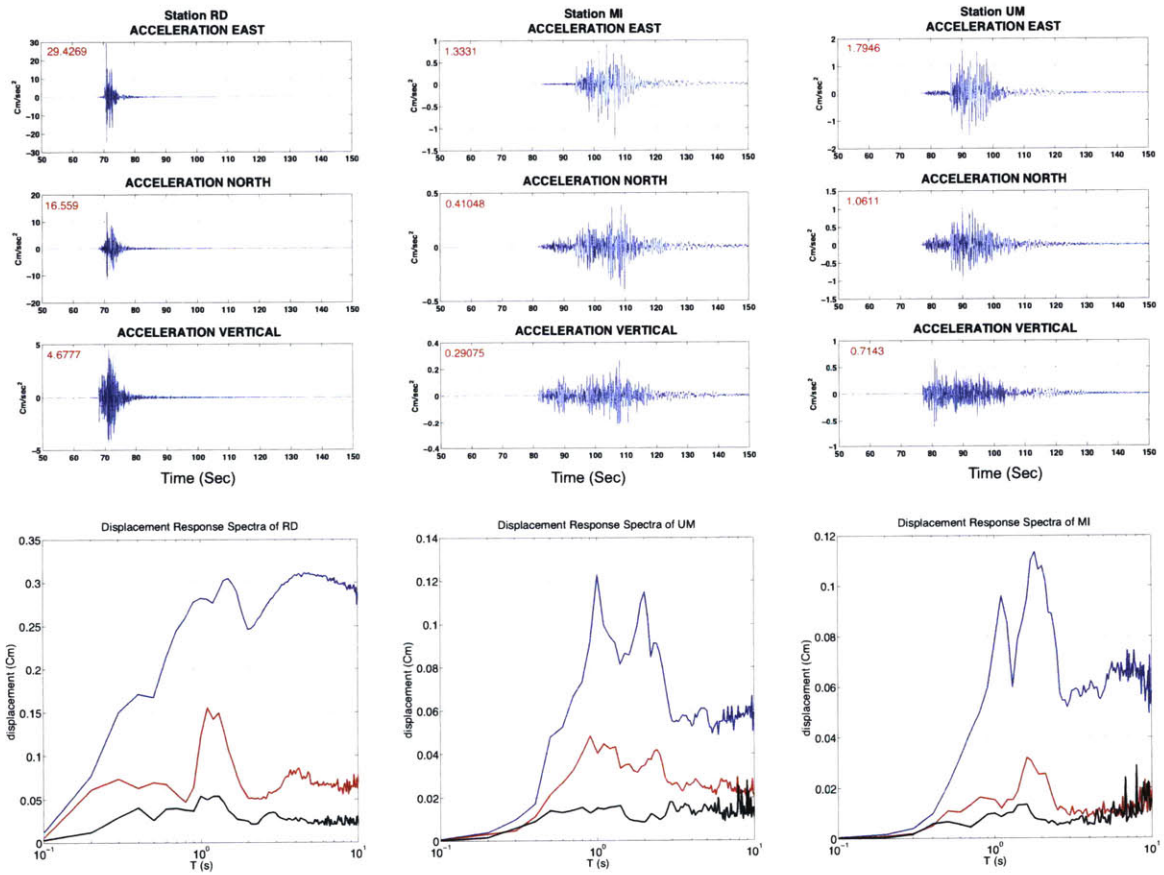

Figure 3-5: Top: 3-Component seismograms for the Mw 4.5 local event (from Kuwait National Seismic Network station. Bottom: Pseudo displacement response spectra of 3-Component seismograms for the Mw 4.5 local event (from Kuwait National Seismic Network stations). The blue line shows the east component, the red line shows the north component, and the black line shows the vertical component.

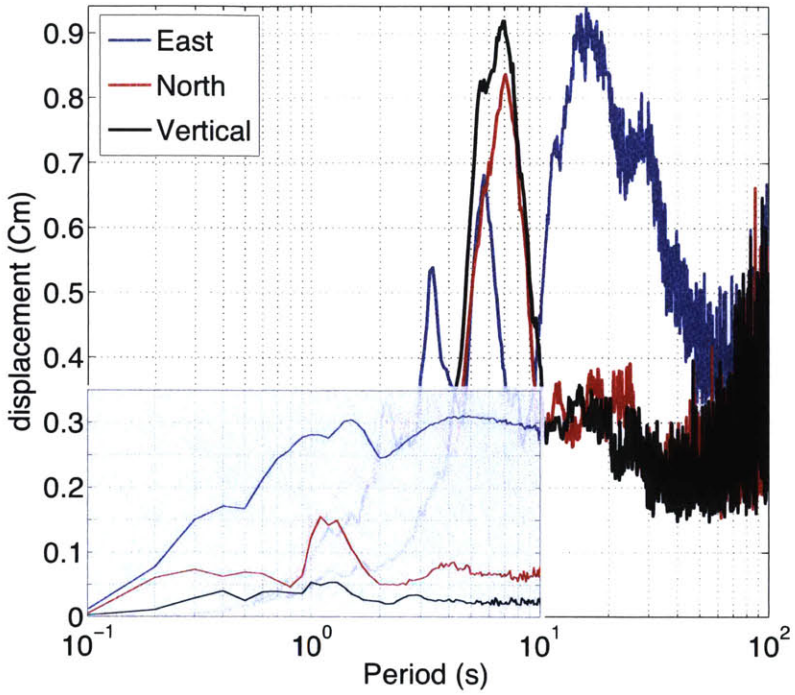

Figure 3-6: The comparison of the pseudo displacement response spectra of the Mw 6.2 (main frame) and Mw 4.5 earthquakes (left-bottom corner in blue sub-frame).

two earthquakes. The peak response period range of the Mw 6.2 earthquake is above 3 s, which is longer than that of the Mw 4.5 earthquake. In addition, the maximum amplitude of the Mw 6.2 earthquake is larger than that of the Mw 4.5 earthquake. However, in the short-period range around 1 s, the Mw 4.5 earthquake presents higher response than the Mw 6.2 earthquake. The different peak response periods mean these two kinds of earthquakes could cause potential damage to structures with different vibration frequencies.

This Chapter focuses on the ground motion simulation in Kuwait, and includes two parts: 1) Ground motion due to regional earthquakes around Kuwait and effects on tall buildings; 2) Ground motions and source mechanisms of local earthquakes and ground motion calculation in Kuwait.

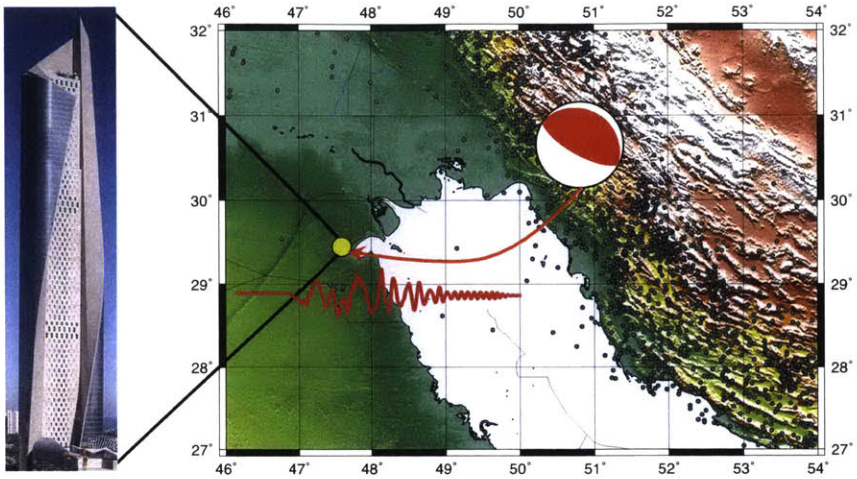

Figure 3-7: The locations of Kuwait and Zagros Fold Belt in a geographic map. The picture of the Al-Hamra building is shown on the left of the map.

3.2 Regional earthquakes around Kuwait

Tall buildings are greatly affected by long trains of low-frequency seismic surface waves from regional earthquakes. There is a rapid increase in the number and construction of tall and ultra high buildings in the world including Kuwait, e.g. the Al-Hamra Tower with the height of 414m (Figure 3-7). Seismic motions are greatly amplified with increasing height of the buildings. Many tall buildings in the world have been built with the structural health monitoring system (Çelebi and Liu, 1998; Çelebi et al., 2014). Building response to seismic activities can be obtained by the seismic interferometry method, using the ambient noise recording from the building monitoring system (Kohler et al., 2005; Snieder and Şafak, 2006; Prieto et al., 2010). However, even with reliable building response, realistic ground motion input is important to assess the seismic hazard to tall buildings.

Previous research has provided useful methods to calculate the ground motion in a region. The ground motion prediction equation is a typical method to estimate ground motion intensity based on the observed seismic data and attenuation laws (Abrahamson and Shedlock, 1997). However, typical hazard calculations do not nclude physics of earthquake source rupture and ignore the effects of complex crustal structures along the wave propagation path on the wave field. To make the predica-

tion more realistic, many studies use simulation methods to predict ground motions using a virtual future large earthquake (Olsen et al., 1995; Pitarka et al., 1998; Olsen, 2000; Olsen et al., 2006, 2009). The reliability of these simulation methods depends on the accuracy of the earthquake source rupture model, the seismic structure where the wave propagated, and the nonlinear site effects. In the recent decade, increasing studies have used the ambient seismic field method to predict the ground motion from sources around seismic stations (Prieto and Beroza, 2008; Denolle et al., 2013, 2014). This ambient seismic field method can only predict the ground motion near the seismic stations. In this section, we use the simulation method to calculate ground motion, since we are focusing on the ground motion calculation from the regional large earthquakes in Zagros Fold Belt.

The possibility of using the simulation method to calculate the ground motion in Kuwait is based on well-documented studies on the source mechanism and seismic structure in Kuwait. These provided valuable background and references for the ground motion calculation in this paper (Jackson and McKenzie, 1984; Bou-Rabee, 2000; Al-Awadhi and Midzi, 2001; Pasyanos et al., 2007; Sadek, 2004). In addition, some previous research has been conducted on long-period ground motion in the Arabian Gulf (Pitarka et al., 2012, 2015), although there have not been quite as detailed studies in the state of Kuwait.

In this section, we first analyzed the ground motion observed by Kuwait National Seismograph Network (KNSN) from regional earthquakes and local earthquakes for selected sites in Kuwait (Bou-Rabee, 1999). The response spectra (pseudo displacement/acceleration spectra) are calculated and compared with the ambient noise spectra at a site near Al-Hamra Tower to assess the seismic hazards to tall buildings in Kuwait City. In addition, to estimate the seismic hazard in Kuwait City, we calculate the ground motion from a Mw 7 virtual earthquake. We consider Mw 7 to be the maximum credible earthquake is because previous seismic hazard research in Oman by El-Hussain et al. (2013). The seismicity of Zagros region and maimum magnitude of credible earthquakes have been studied extensively for seismic hazard studies in Eastern Gulf region (especially Dubai, UAE, and Oman). To minimize the calculation

uncertainties from the crustal and sedimentary basin structures model, we calibrated the input velocity model with a recent 08/18/2014 Mw 6.2 earthquake. The effects of near surface sediments (i.e., soil layers) on the surface waves have also been identified by conducting a simple 2-D finite difference simulation.

3.2.1 Methods and model validation

The observed ground motion in Kuwait shows that the potential hazard to tall buildings in Kuwait is from regional earthquakes. To predict the ground motion in Kuwait and provide information for the generation of building codes, we need to calculate the ground motions for potential earthquakes near Kuwait.

For ground motion calculation, we used the discrete-wavenumber (Bouchon, 1981, 2003) method for the 1-D layered modeling and the finite difference method for the 2-D and 3-D structural models (Almuhaidib and Toksöz, 2014). In this paper, we focused on the 1-D velocity model in Kuwait. The crustal velocity model is based on the KUW1 model of Pasyanos et al. (2007). The 2-D finite difference modeling was used to identify the amplification effects of soil layers in Section 3.2.2.

To validate the method and model, we selected the 08/18/2014 Mw 6.2 earthquake, synthesized the seismograms of that earthquake and made the comparison with the observed seismograms. To better fit the observed seismograms, we varied the thickness, P-wave velocity, and S-velocity of the first layer from the KUW1 model of Pasyanos et al. (2007). The velocity model used in this paper is shown in Table 3.1. There is a good match between the observed and synthetic seismograms, as well as their displacement response spectra (Figure 3-8).

3.2.2 Results and discussion

To determine the ground motions in Kuwait, synthetic seismograms from the largest credible magnitude regional earthquakes were calculated – a Mw 7 earthquake located 300 km east of Kuwait City. Maximum credible magnitude for the region is $Mw = 7$ corresponding to a moment of $M_0 = 6.6 * 10^{26}\ dyne \cdot cm$. Source (fault rupture

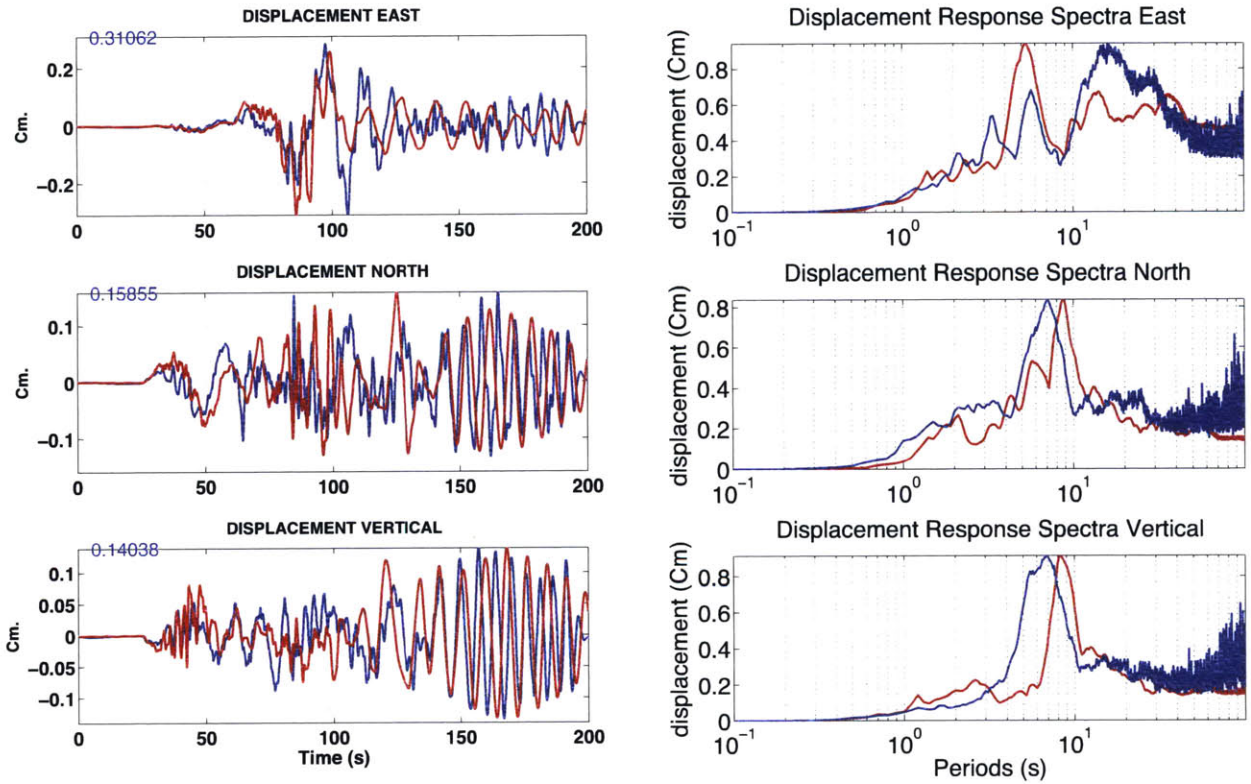

Figure 3-8: : Left: The synthetic seismograms (red) match the recorded (blue) well. Right: The synthetic (red) and observed (blue) pseudo displacement response spectra match well.

Table 3.1: 1-D elastic model for ground motion calculation[a]

Layer number	Thickness (km)	V_P ($km/2$)	V_S ($km/2$)	Density (g/cm^2)	Q_P (s^{-1})	Q_S (s^{-1})
1	3.0	2.50	1.50	2.50	80	40
2	4.0	4.76	2.75	2.60	100	50
3	17.0	5.89	3.40	2.70	300	150
4	9.0	6.41	3.70	2.70	300	150
5	11.0	6.95	3.90	2.70	300	150
6	∞	7.80	4.40	2.70	300	150

[a] To better fit the observed seismograms, we varied the thickness, P-wave velocity (V_P), and S-wave velocity (V_S) of the first layer of the KUW1 model of Pasyanos et al. (2007).

dimension) was assumed to be 20 km × 40 km with the top of the rupture 5 km below the surface, as shown in Figure 3-9. The model earthquake is a thrust event with fault plane: strike = 300°, dip = 20°, and rake = 90°. The ground acceleration, velocity, and displacement were calculated and shown in Figure 3-10. Our calculation results show that in Kuwait City, the maximum acceleration in Kuwait is 5 cm/sec^2 and maximum displacement is 5 cm. The duration of the ground motion is longer than 200 seconds.

It is important to mention that the ground motions shown in the figures are for bedrock, that is for competent rocks. Soil layers tend to amplify these motions and the amplification depends on geotechnical properties of the site.

Soil and soft sediments generally amplify the ground motions. We demonstrated this by an example where there is a sedimentary patch on the hard crustal layer (1-D Kuwait velocity model). We placed seismic station STA1 on the top of the soil layer, and STA2 on the top of a hard rock. The attenuation effects are ignored here. The seismic source is set as a simple point source 5 km away from STA2, and 10 km from STA1. The resulting two-component seismograms are shown in Figure 3-11. Note that the shear waves and Rayleigh waves are amplified by more than a factor of two on the sediment layer. Thus, depending on geotechnical conditions and soil properties, actual ground motion could be twice as high or higher. With more detailed information about the geotectonical information underneath Kuwait City, we can better quantify and predict the ground motions.

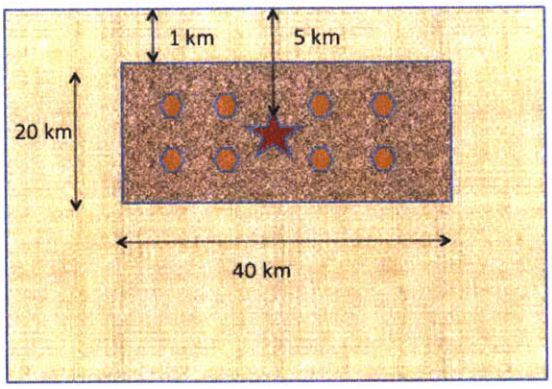

Figure 3-9: Finite Zagros Fault Model ($M_w = 7$), $M_0 = 6.6 * 10^{26}$ $dyne \cdot cm$ used for discrete-wavenumber integration based ground motion simulations. The source dimension is 20 km×40 km. The calculated seismogram in Kuwait city due to an earthquake located across the Gulf from Kuwait is shown in Figure 3-10. The maximum acceleration in Kuwait is 5 cm/sec^2 and maximum displacements are 5 cm. The duration of the ground motion is longer than 200 seconds. The contoured maximum displacements around the quake are also shown in the Figure 3-10.

3.3 Local earthquakes in Kuwait

Kuwait has relatively low local seismicity historically. The maximum reported local earthquake was the 1993 M4.7 Kuwait earthquake, which could have been induced by the burning of the oil fields during the Iraq war (Bou-Rabee and Nur, 2002). However, in recent years the improved Kuwait National Seismic Network (KNSN) has monitored more and more local earthquakes. Since 1997, the KNSN has recorded more than 1000 earthquakes (Mw < 5). Two large local earthquakes - Mw4.5 in 03/21/2015 and Mw4.1 in 08/18/2015 - were reported by both the Incorporated Research Institutions for Seismology (IRIS) and KNSN. Earthquakes happen repeatedly in the same general locations close to the oil/gas fields in Kuwait. The correlation of oil/gas fields and earthquake epicenters are shown in Figure 3-4. The earthquakes are generally small (Mw < 5.0) and are shallow with focal depths of about 2 to 8 km. Such events are very common in oil/gas reservoirs all over the world, including North America, Europe, and the Middle East (Sarkar, 2008; Li et al., 2011a,b; Zoback and Gorelick, 2012; Ellsworth, 2013; Shapiro, 2015). In Kuwait, because of the proximity of these earthquakes to population centers, they could create seismic hazard to older structures built without any earthquake design codes. Determining the nature of these events

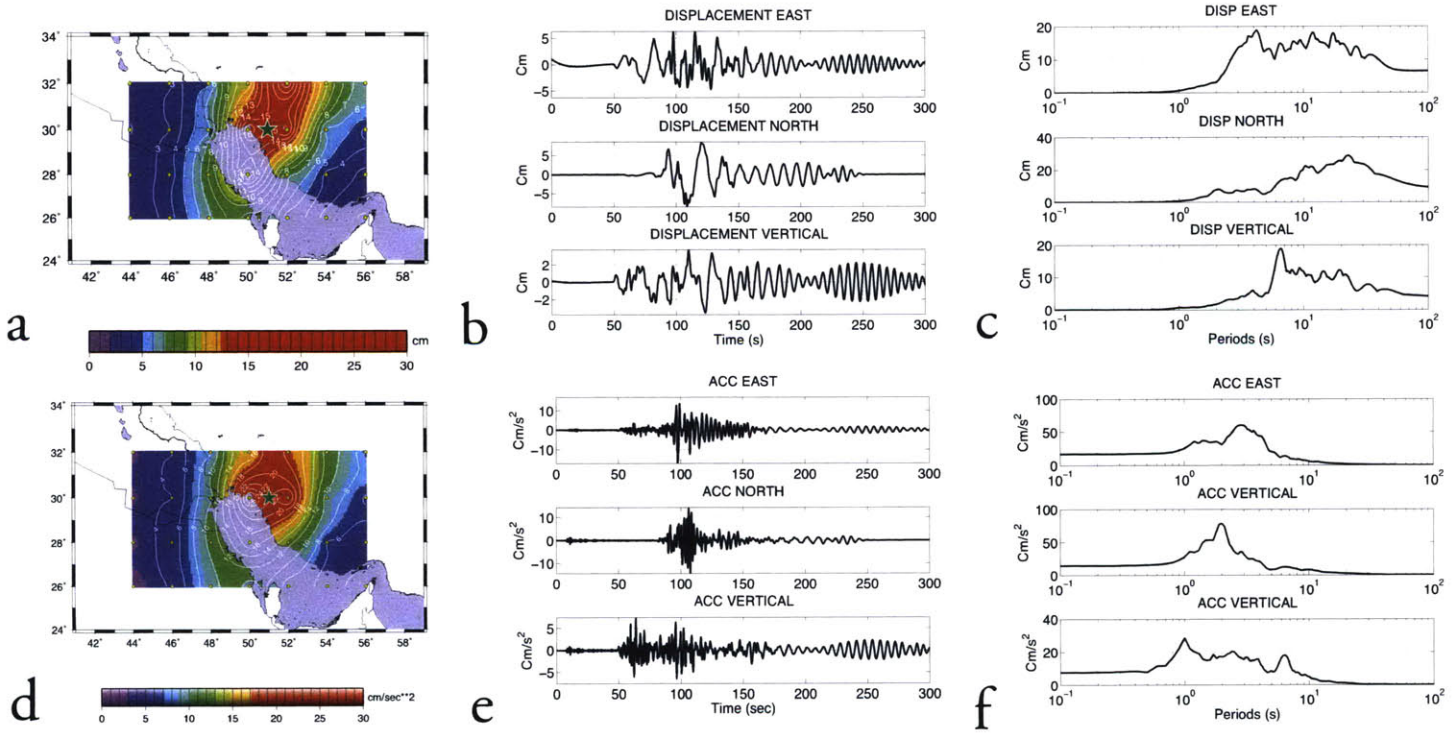

Figure 3-10: Modeled ground motions in Kuwait City due to magnitude Mw=7.0 thrust earthquake in Zagros with strike = 300, Dip=20, and Rake=90. a) contour of maximum displacements (cm) around the epicenter (green star); b) displacement seismiograms (cm); c) pseudo displacement spectra (cm); d) contour of maximum accelerations (cm/s^2) around the epicenter (green star); e) accelerations (cm/s^2); f) pseudo acceleration spectra (cm/s^2).

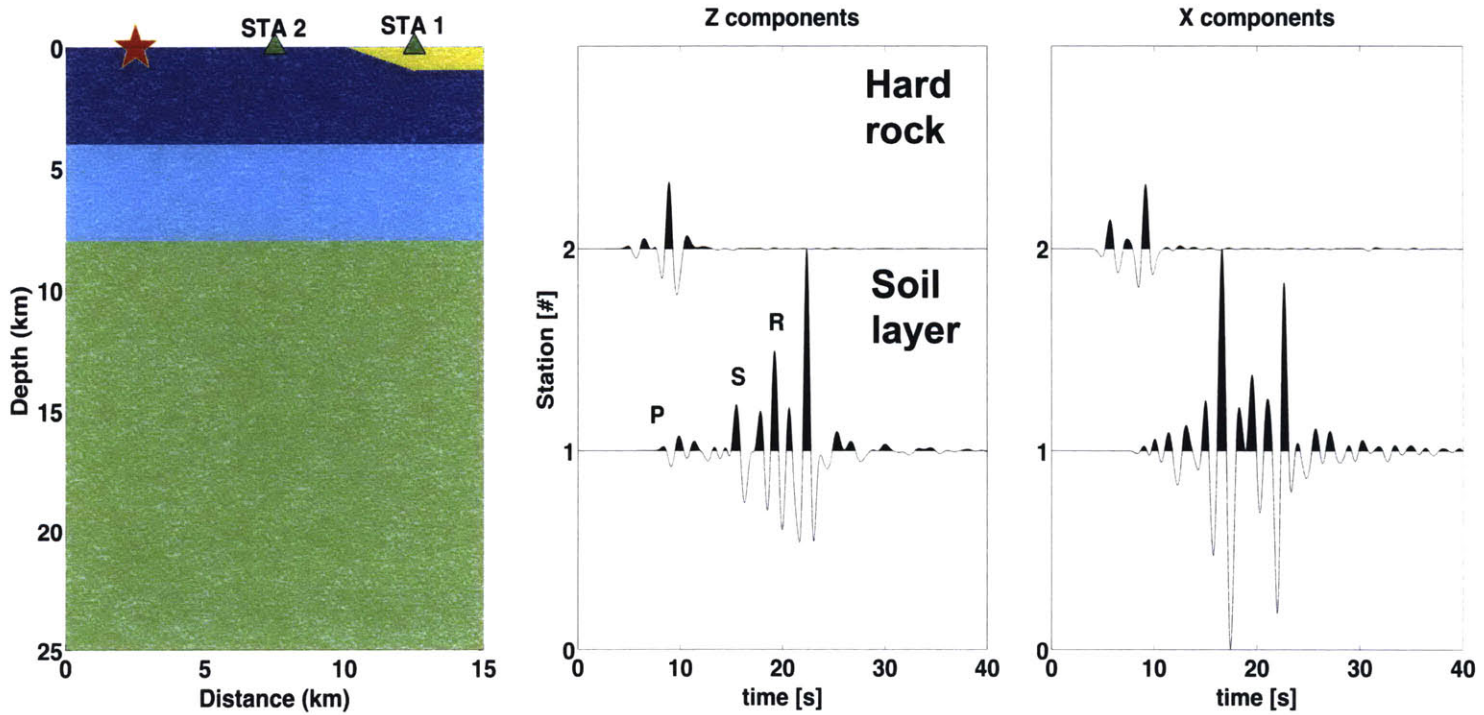

Figure 3-11: Left: 2-D crustal structure; Middle: Vertical component seismograms for STA1 and STA2; Right: Horizotal component seismograms for STA1 and STA2

is important to improve the performance and safety of existing systems.

Source mechanism inversion has been widely used to study the physics of earthquakes in oil/gas fields (Li et al., 2011a,b; Song and Toksöz, 2011). However, the source physics of the local events has seldom been studied in Kuwait. Previous geological and geophysical studies focus on the tectonic and seismic structures in Kuwait (Carman, 1996; Bou-Rabee and VanMarcke, 2001; Pasyanos et al., 2007; Laske et al., 2013). Carman (1996) has studied the five structural elements in Kuwait based on the data of the seismic structure maps, oil wells, remote sensing/imaging data, and rock physics. That study indicated a northeast trend for the maximum principal horizontal stress field. Pasyanos et al. (2007) studied the crustal structures in Kuwait using the joint inversion of teleseismic receiver function and Rayleigh and Love fundamental mode surface wave group velocity dispersion. More detailed studies about the shallow structures in Kuwait have been reported by Bou-Rabee and VanMarcke (2001) and Bou-Rabee (2000). These structural studies provided valuable background references for the source mechanism study in this part.

In this part, we studied the source mechanisms of selected local earthquakes, with their uncertainties, using a Bayesian moment tensor method (Gu et al., submitted). The maximum compressional stress, indicated by the source mechanism results, matches with the regional north-east stress field around Kuwait. Most likely these local earthquakes occurred on pre-existing faults and were triggered by oil field activities, as determined by true history of the events.

An accurate near-surface seismic structure is significant to study the source mechanism of local earthquakes. We use the known sonic well logging data to better constrain the velocity model in the shallow depth. All the velocity values from the well logging data are plotted in Figure 3-12.

Combining the KUW1 model and the well logging data, we tested three velocity models - KUW1, VEL1, and VEL2 (Figure 3-13) - in the later source mechanism inversion study.

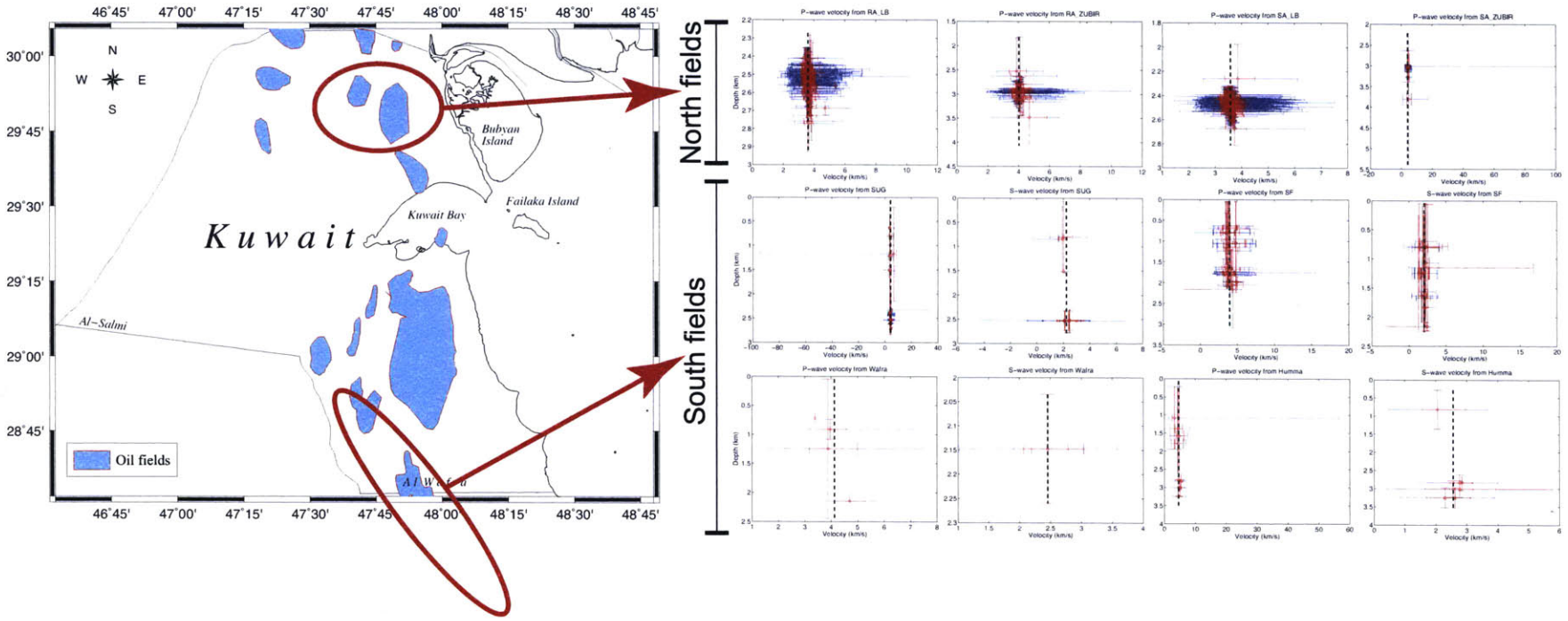

Figure 3-12: Velocity values from the well logging data from the northern and southern oil fields. The dots show the mean velocity values, the blue error bar show the maximum velocity ranges, the red error bar show the velocity standard deviation, and the black dashed lines denote the mean of all the velocity data points.

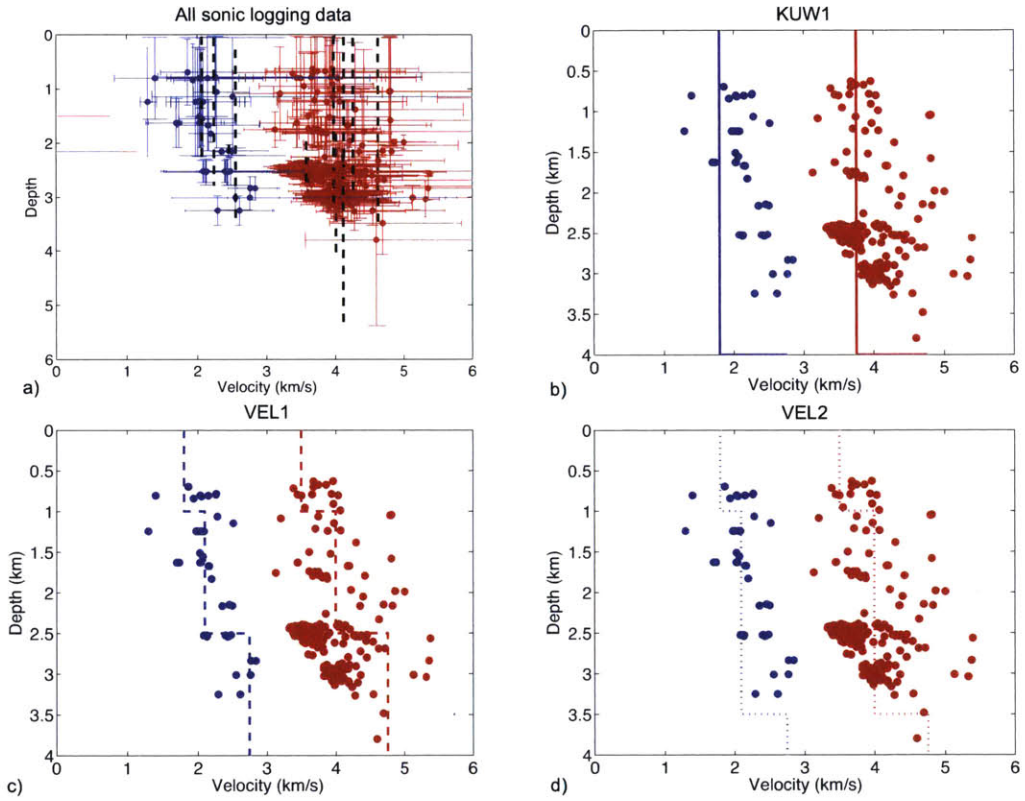

Figure 3-13: Left: The trial velocity model. We use KUW1 velocity model (Pasyanos et al., 2007) from 8 km to ∞. All the trial two-layer model from 0 to 8 km are plotted in the same figure; Right: Zoom in of the depth 0 to 8 km.

3.3.1 Data and methodology

The local earthquakes are generally distributed in two clusters, one around the northern oil fields and the other around the southern oil fields. The seismic data of these local earthquakes were collected by the Kuwait National Seismograph Network (KNSN). The KNSN was initiated in 1997 (Bou-Rabee, 1999), and consisted of seven three-component short-period stations (AB, MI, QR, RD, RS, SA, UM) and one three-component broadband station (KB) in operation from 1997 to 2013. Since the year 2013, the KNSN has upgraded the seismic monitoring network by replacing five short-period stations (MI, QR, RD, RS, UM) with broadband stations. The count of earthquakes shows an increased occurrence rate of the total number of earthquakes since 2002, and a more rapid increase of $M \geq 3$ since 2012 (Figure 3-14). The figure shows a non-uniform distribution of earthquakes. There are three factors that contribute to the distribution: 1) The improvement of the KNSN with time; 2) Disruption caused by the invasion of Kuwait by Iraq in 1990; and 3) The U.S.-Iraq war in 2004 and the following terrorism. Since 2013 the KNSN has been operating without interruptions.

We focused on the broadband seismic data of $M \geq 3$ earthquakes from 2013 to 2015 because of the high quality and broad frequency response of these seismograms. We applied the cross-correlation to the waveforms from northern and southern clusters at the same station and found the waveforms from the same cluster have high correlation coefficients (> 0.5). One example of the waveform correlation for the vertical components of station RS was presented in Figure 3-22. This means that these earthquakes, which occurred repeatedly in the same areas, should have similar source mechanisms. The other waveform correlation analysis results are shown in Figure 3-18, 3-19, 3-20, 3-21, and 3-23.

To determine the source mechanisms of the event, as well as their uncertainties, we applied the waveform-based Bayesian moment tensor inversion methods (Chapter 2) to the two largest local events in 2015 – 03/21/2015 Mw 4.5 and 08/18/2015 Mw 4.1 earthquakes (Figure 3-15). We sampled the moment tensor solution $\boldsymbol{m} =$

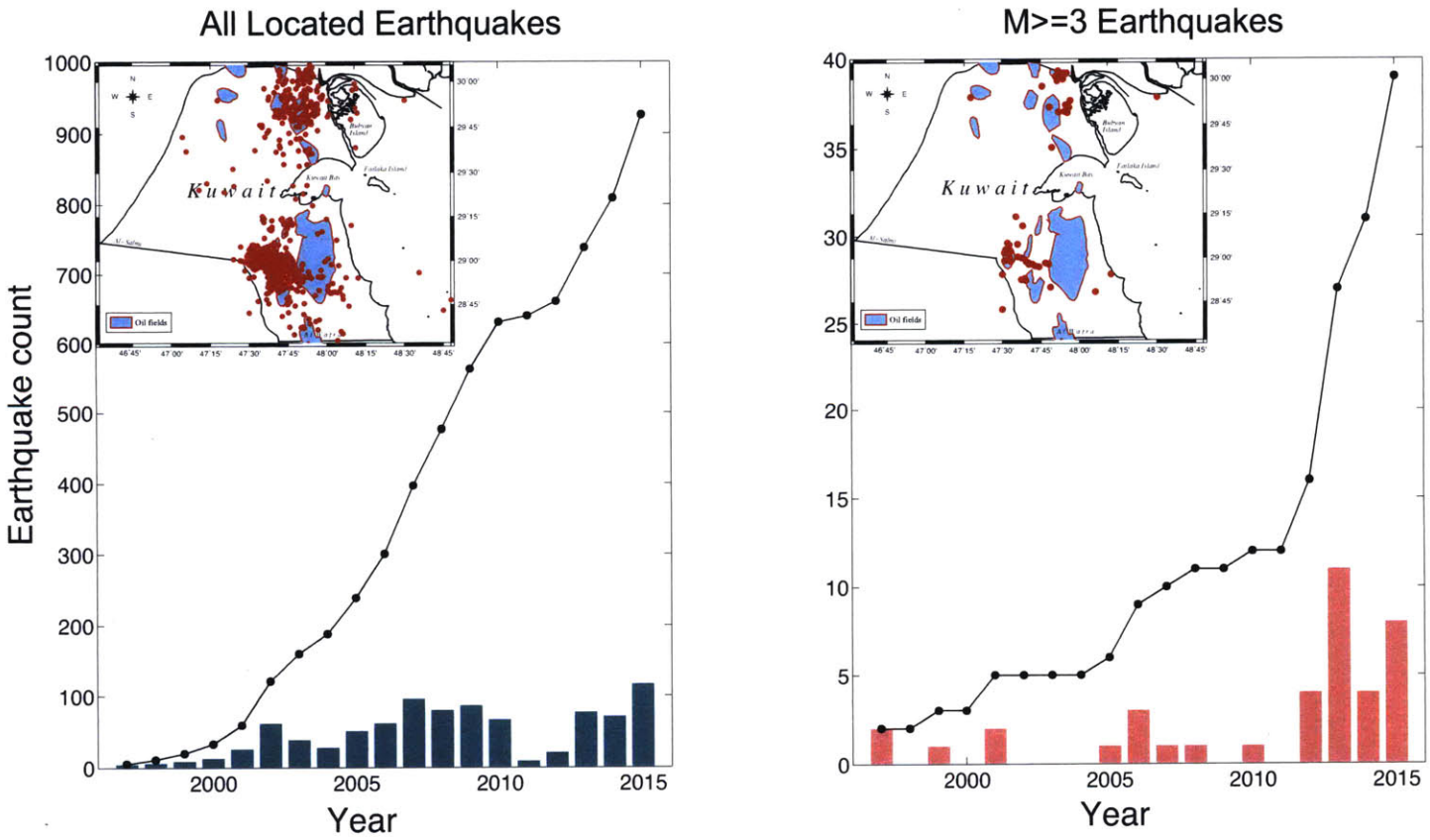

Figure 3-14: Count of Local earthquakes (left) during 1997 to 2015. Left: The count and cumulated count of all the located earthquakes. The location of these earthquakes in a geographic map are shown in the inset. Right: The count and cumulated count of $M \geq 3$ earthquakes. The location of the $M \geq 3$ earthquakes in a geographic map is shown in the inset.

$(M_{11}, M_{22}, M_{33}, M_{12}, M_{13}, M_{23})^T$, according to the full conditional distribution

$$P(\boldsymbol{m}|\boldsymbol{d}, \boldsymbol{x}^*) \propto P(\boldsymbol{d}|\boldsymbol{m}, \boldsymbol{x}^*) = \frac{1}{\sqrt{(2\pi)^N \det \boldsymbol{\Sigma_e}}} \exp\left[-\frac{1}{2}(\boldsymbol{d} - \boldsymbol{G}(\boldsymbol{x}^*)\boldsymbol{m})^T \boldsymbol{\Sigma_e}^{-1} (\boldsymbol{d} - \boldsymbol{G}(\boldsymbol{x}^*)\boldsymbol{m})\right], \tag{3.1}$$

where d denotes the waveform data, $\boldsymbol{\Sigma_e}$ is the error covariance matrix, and $\boldsymbol{G}(\boldsymbol{x}^*)$ is the matrix containing the synthetic seismograms of six elementary moment tensor parameters at the trial location $\boldsymbol{x}^*$. The trial location has varied from depth of zero to ten km at the event hypocenter. We tried different source depths because the event depth is difficult to determine accurately by the travel-time-based location method, with the sparse seismic network and inadequate knowledge of a detailed velocity model for the crust. The depth distribution from the catalog was shown in Figure 3-15. The depth of the events generally concentrated at 2 to 8 km. Note the depths shown in Figure 3-15 are not include any information about their uncertainties. The accuracy determination of the depth will be shown in the later section. The waveform-based moment tensor inversion can help to locate the events more accurately. We sampled 10^3 $\boldsymbol{m}$ at each trial source depth, and quantified the uncertainties by calculating the mean and standard deviation of posterior predicted $\boldsymbol{m}$.

3.3.2 Results

Applying the waveform-based Bayesian moment tensor inversion method, we obtained the source mechanisms of the 03/21/2015 Mw 4.5 and 08/18/2015 Mw 4.1 earthquakes. We show the variance reduction (VR) as a function of trial depth in Figure 3-15. The best full moment tensor results and the uncertainties are shown in the inset. The waveform matching is presented in the same figure. We plot the posterior predicted waveforms as the purple shaded areas, and the mean predicted waveforms as bold red lines. The posterior predicted waveforms are calculated using $\boldsymbol{G}(\boldsymbol{x}^*)\boldsymbol{m}$, where $\boldsymbol{G}(\boldsymbol{x}^*)$ is the Green's function at the the fixed location $\boldsymbol{x}^*$ and $\boldsymbol{m}$ is from the direct MCMC sampling.

The best fitting depth - 2 km and 4 km - for the two earthquakes is shallow and close to the typical reservoir depth. The maximum stress field from the source mech-

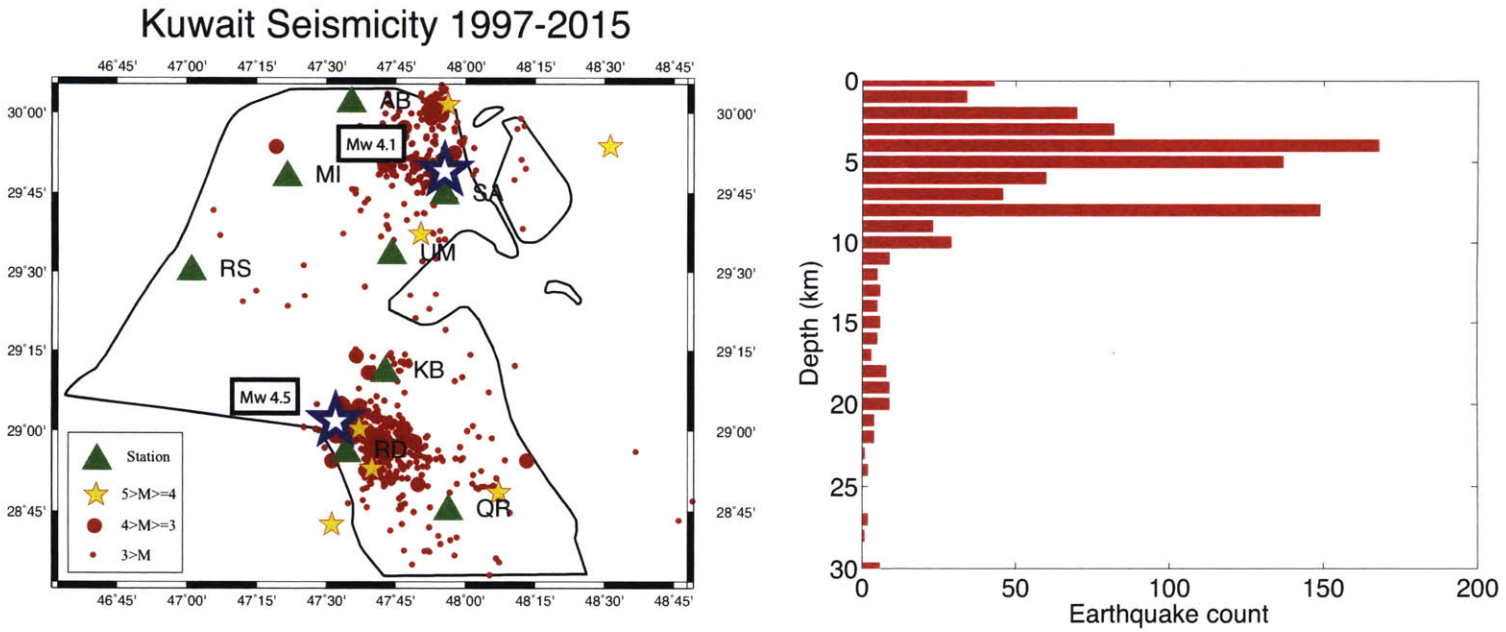

Figure 3-15: Left: 03/21/2015 Mw 4.5 and 08/18/2015 Mw 4.1 earthquakes in a geographic map. Right: Depth distribution for all the located earthquakes. Note the depths shown here are not include any information about their uncertainties. The accuracy determination of the depth will be shown in later.

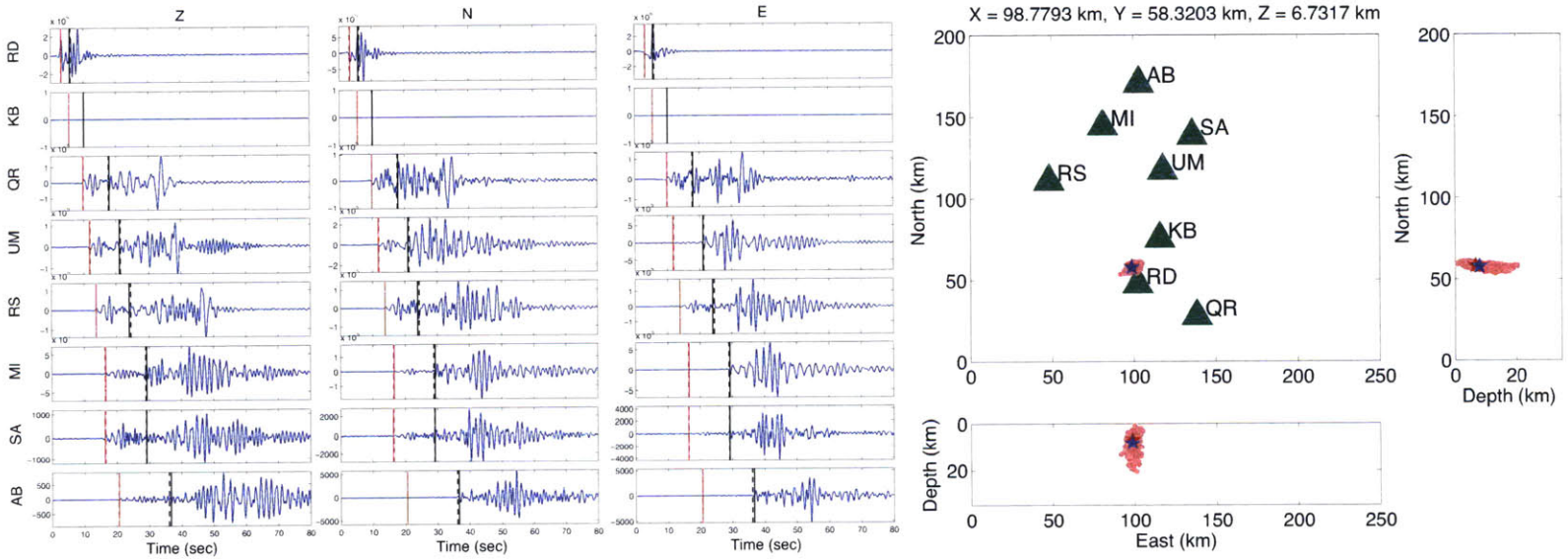

Figure 3-16: Left: The location uncertainty of the 03/21/2015 Mw 4.5. The light-red dots are the posterior location sampling. Right: The observed and theoretical travel time picks marked on the waveforms. The solid lines show the picked P and S waves, and the dashed lines show the theoretical P and S waves.

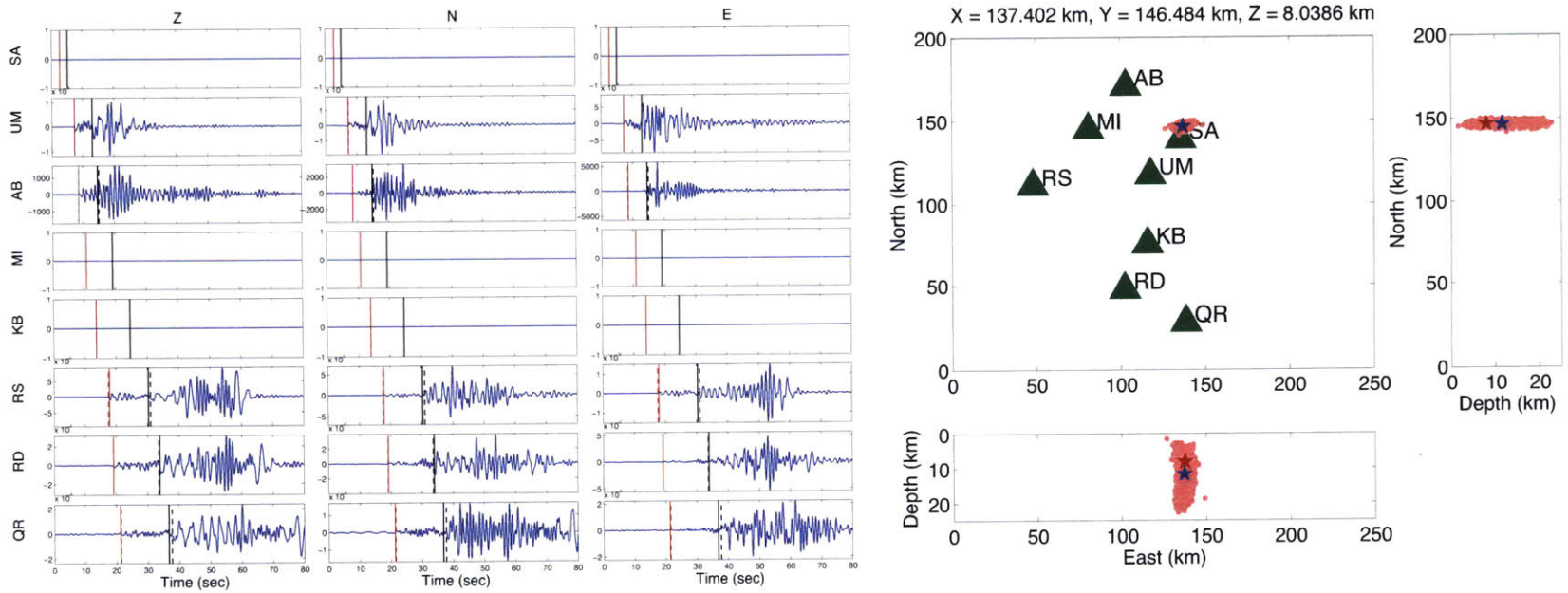

Figure 3-17: Left: The location uncertainty of the 08/18/2015 Mw 4.1. The light-red dots are the posterior location sampling. Right: The observed and theoretical travel time picks marked on the waveforms. The solid lines show the picked P and S waves, and the dashed lines show the theoretical P and S waves.

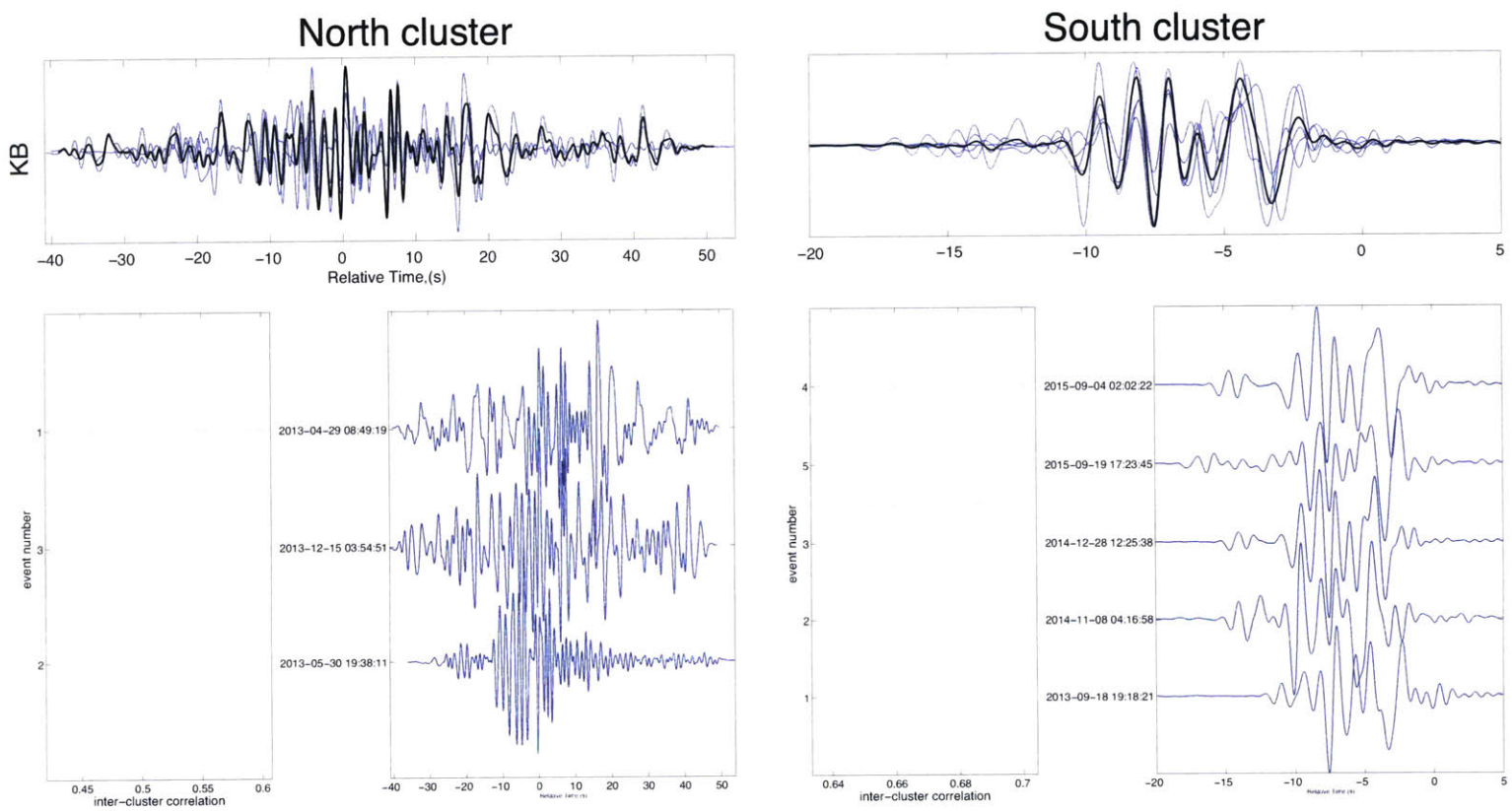

Figure 3-18: The waveform correlation of the $M \geq 3$ earthquakes from the broadband station KB during 2013 to 2015. The waveform overlay and the average waveform are plotted on the top. The linkage and alignment of the waveform are shown on the bottom. Left: Events from the north cluster. Right: Events from south cluster.

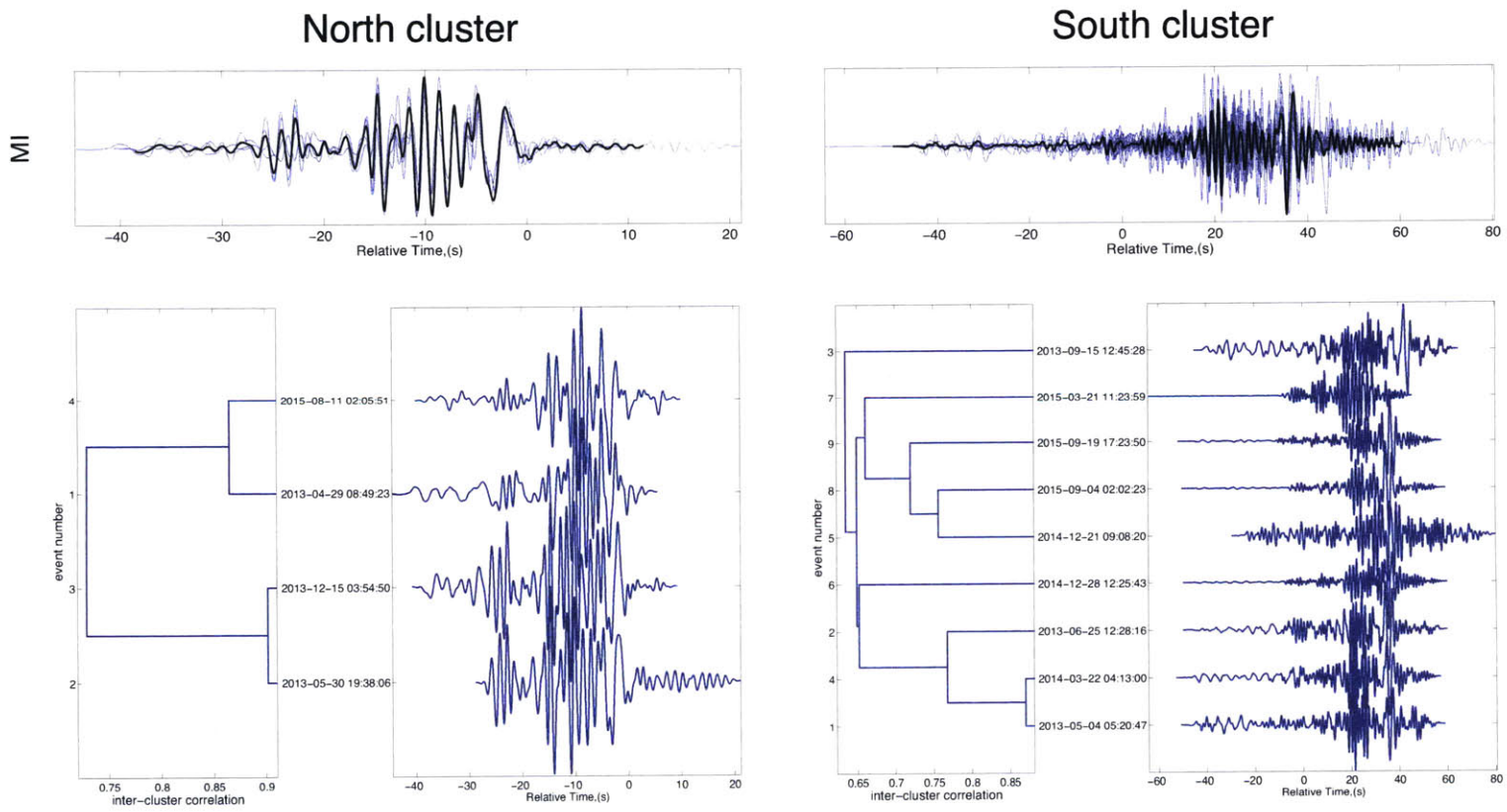

Figure 3-19: The waveform correlation of the $M \geq 3$ earthquakes from the broadband station MI during 2013 to 2015. The waveform overlay and the average waveform are plotted on the top. The linkage and alignment of the waveform are shown on the bottom. Left: Events from the north cluster. Right: Events from south cluster.

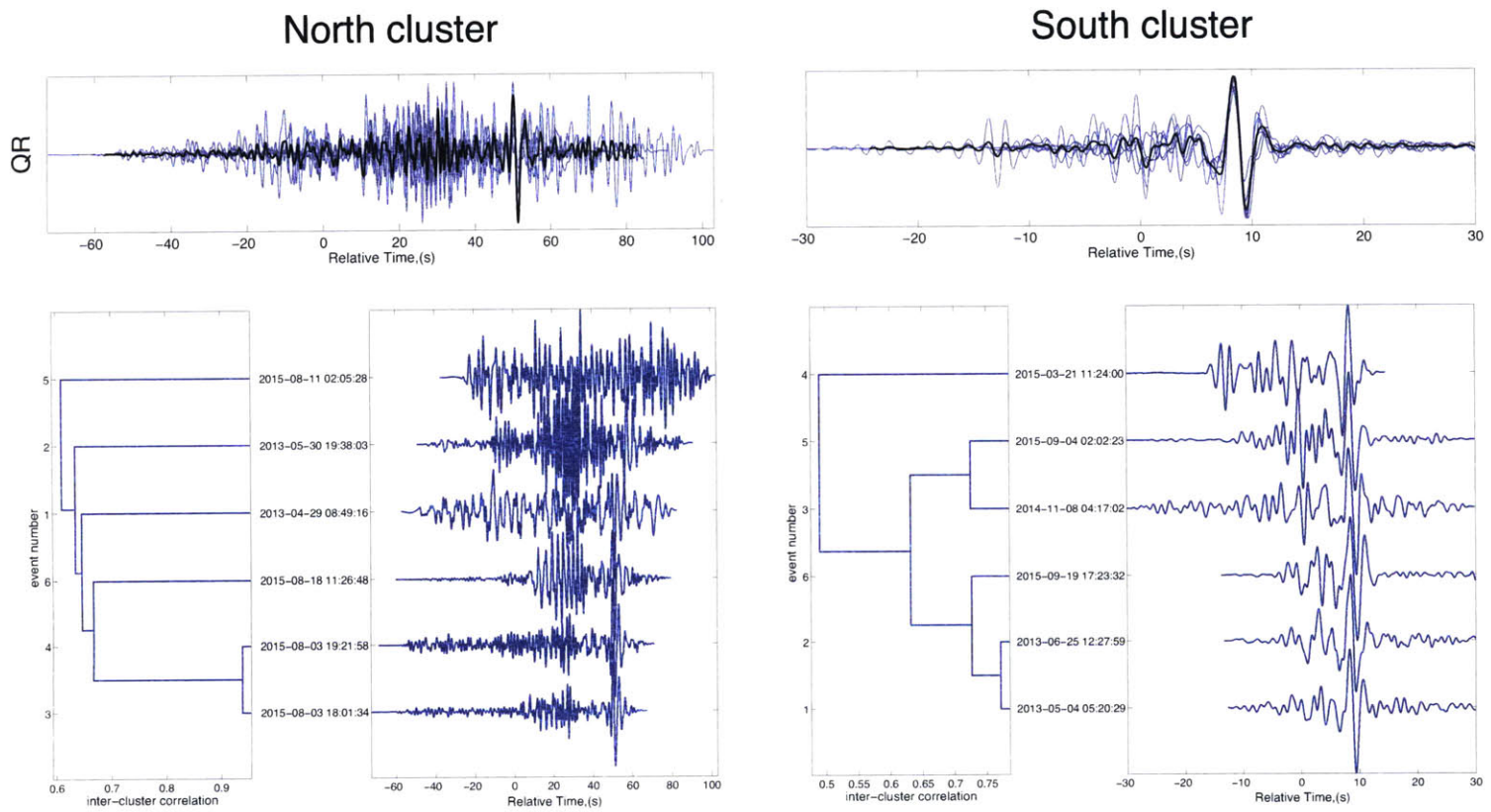

Figure 3-20: The waveform correlation of the $M \geq 3$ earthquakes from the broadband station QR during 2013 to 2015. The waveform overlay and the average waveform are plotted on the top. The linkage and alignment of the waveform are shown on the bottom. Left: Events from the north cluster. Right: Events from south cluster.

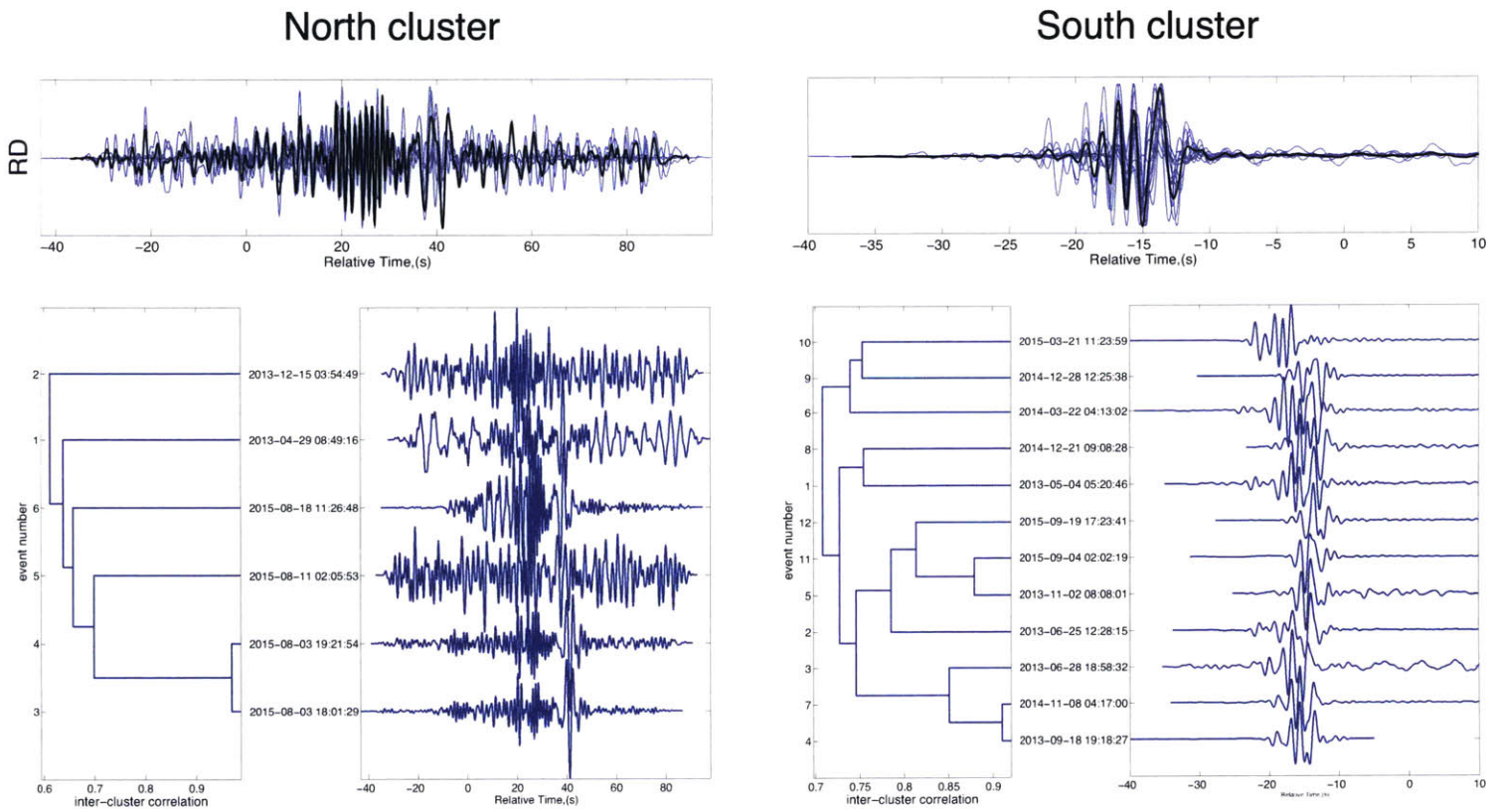

Figure 3-21: The waveform correlation of the $M \geq 3$ earthquakes from the broadband station RD during 2013 to 2015. The waveform overlay and the average waveform are plotted on the top. The linkage and alignment of the waveform are shown on the bottom. Left: Events from the north cluster. Right: Events from south cluster.

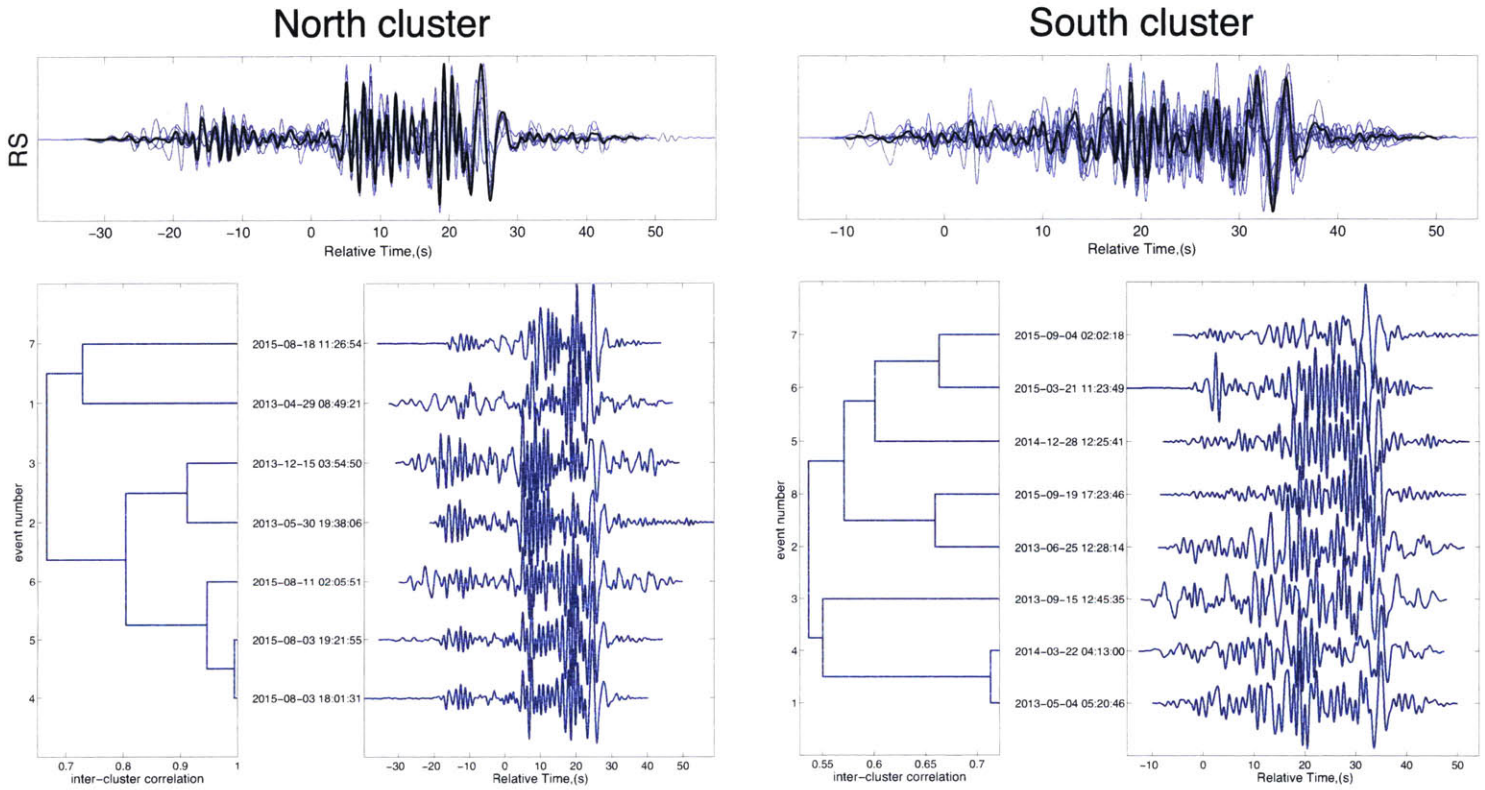

Figure 3-22: The waveform correlation of the $M \geq 3$ earthquakes from the broadband station RS during 2013 to 2015. The waveform overlay and the average waveform are plotted on the top. The linkage and alignment of the waveform are shown on the bottom. Left: Events from the north cluster. Right: Events from south cluster.

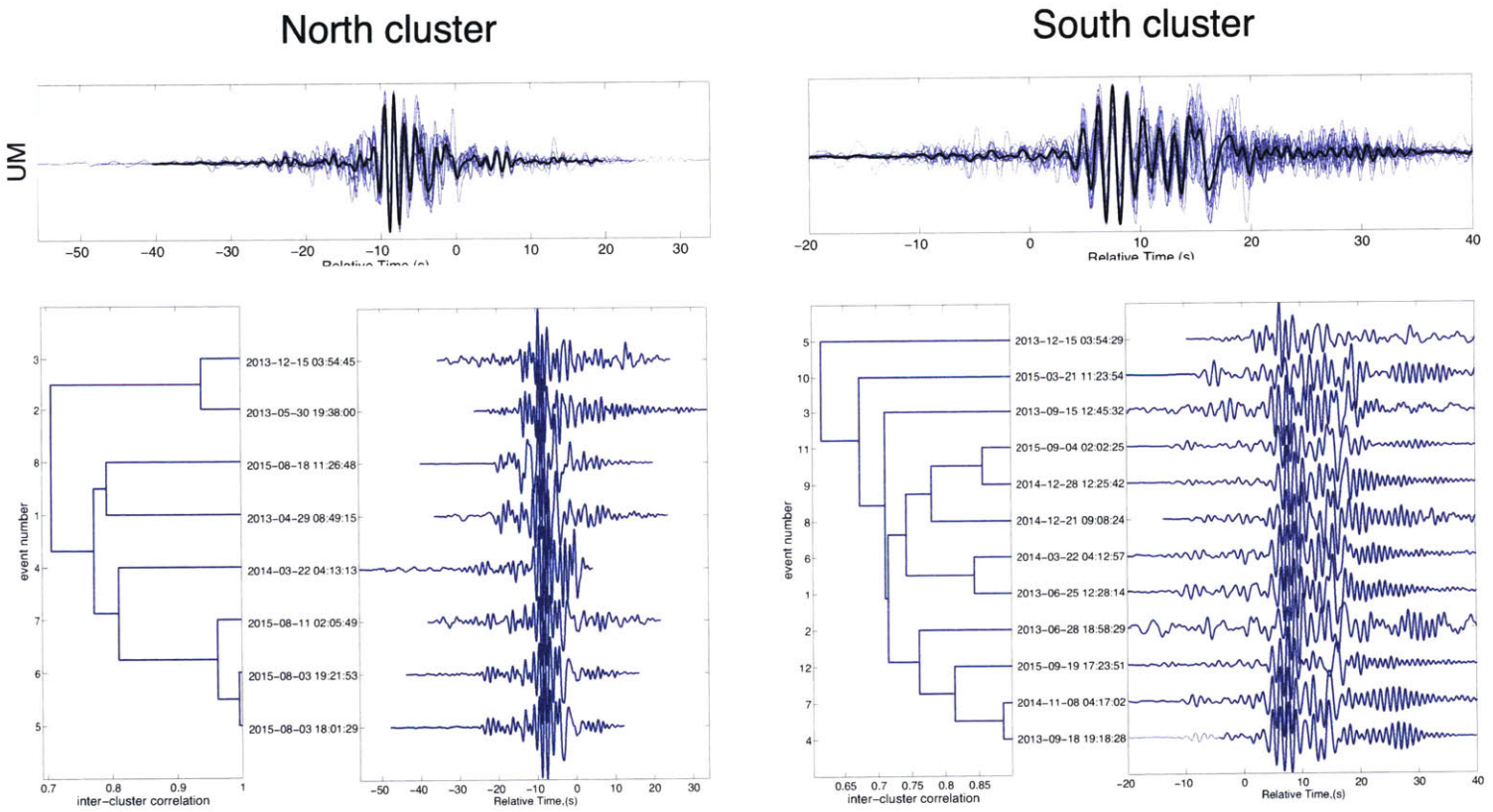

Figure 3-23: The waveform correlation of the $M \geq 3$ earthquakes from the broadband station UM during 2013 to 2015. The waveform overlay and the average waveform are plotted on the top. The linkage and alignment of the waveform are shown on the bottom. Left: Events from the north cluster. Right: Events from south cluster.

anism results matches with the local northeast-southwest maximum compressional stress direction. We note the second maximum VR for Mw 4.5 earthquake also show the possibility that this earthquake may have occured at deeper depth – 8 km. However, the trial source at 8 km does not produce the strong Rayleigh waves shown in most of the local earthquakes in Kuwait.

To determine the ground motions due to local earthquakes in Kuwait, we synthesize the seismograms from the largest credible magnitude local earthquakes calculated – a Mw = 4.5 EQ located at the southern and a Mw = 4.1 EQ located at the northern oil fields. We show the acceleration distribution in Kuwait in Figure 3-33, 3-34, and 3-35.

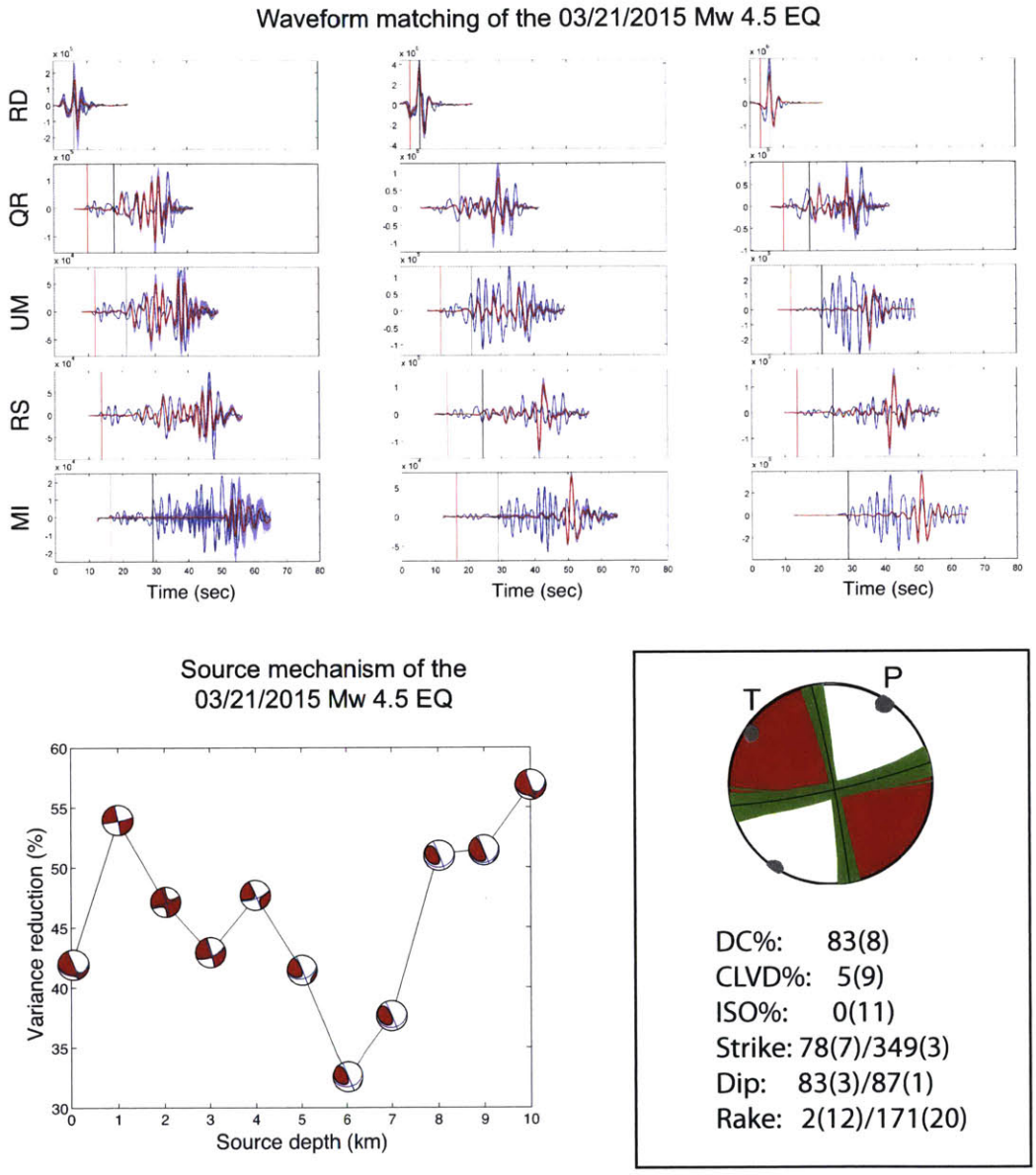

Figure 3-24: Results from KUW1 velocity model. Upper: The comparison of the real data (blue) and the mean posterior predicted waveform (red) for the Mw 4.5 earthquake at the best matching depth. The data are bandpass filtered by 0.1 to 0.5 Hz. Right: Variance reduction of waveform matching as a function of trial source depth. The resulted source mechanism of different trial depth are plotted as beach ball on the figure. The best source mechanism solution, presented as both beachball and text, is shown in the black frame.

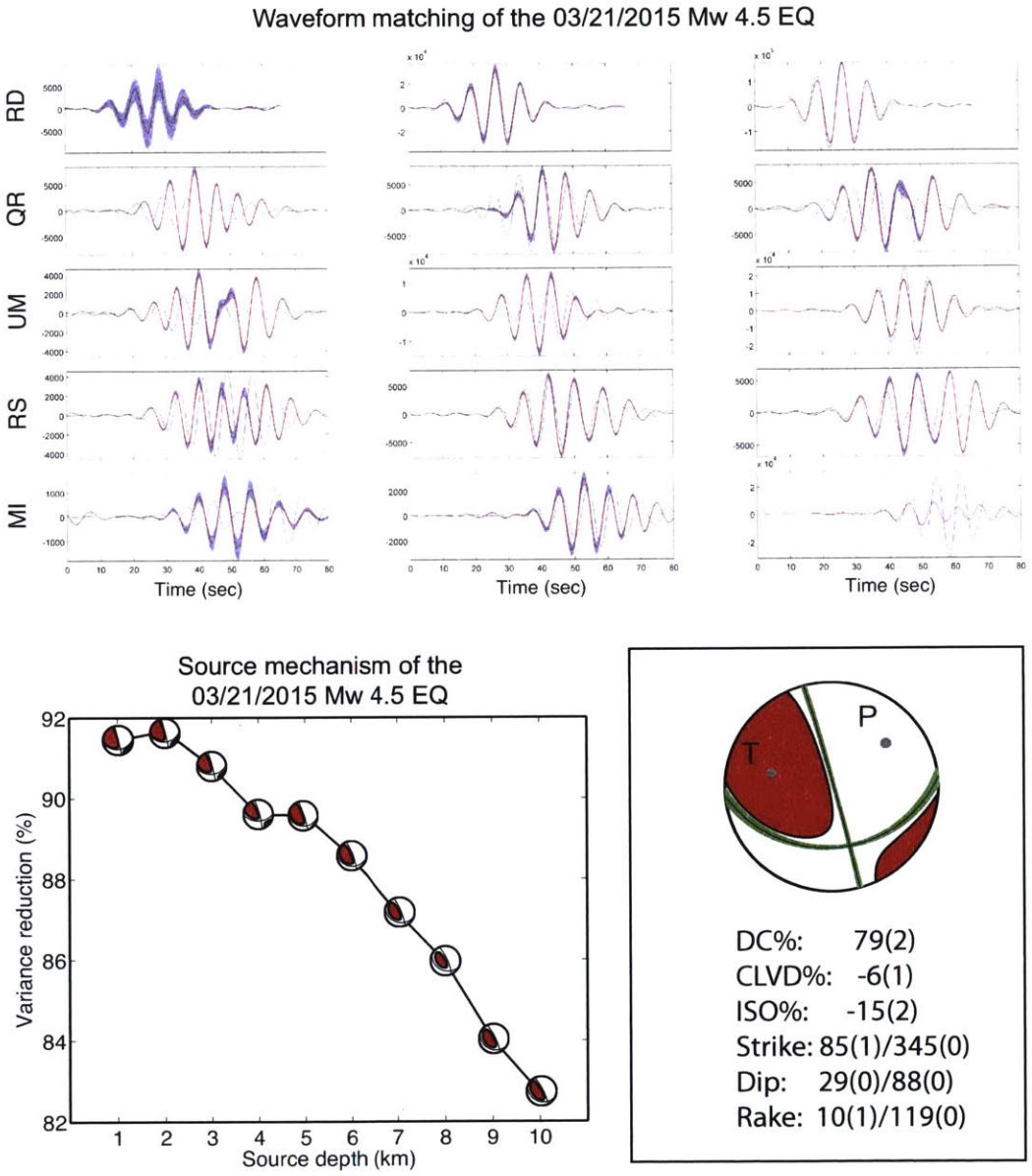

Figure 3-25: Results from KUW1 velocity model. Upper: The comparison of the real data (blue) and the mean posterior predicted waveform (red) for the Mw 4.5 earthquake at the best matching depth. The data are bandpass filtered by 0.1 to 0.15 Hz. Right: Variance reduction of waveform matching as a function of trial source depth. The resulted source mechanism of different trial depth are plotted as beach ball on the figure. The best source mechanism solution, presented as both beachball and text, is shown in the black frame.

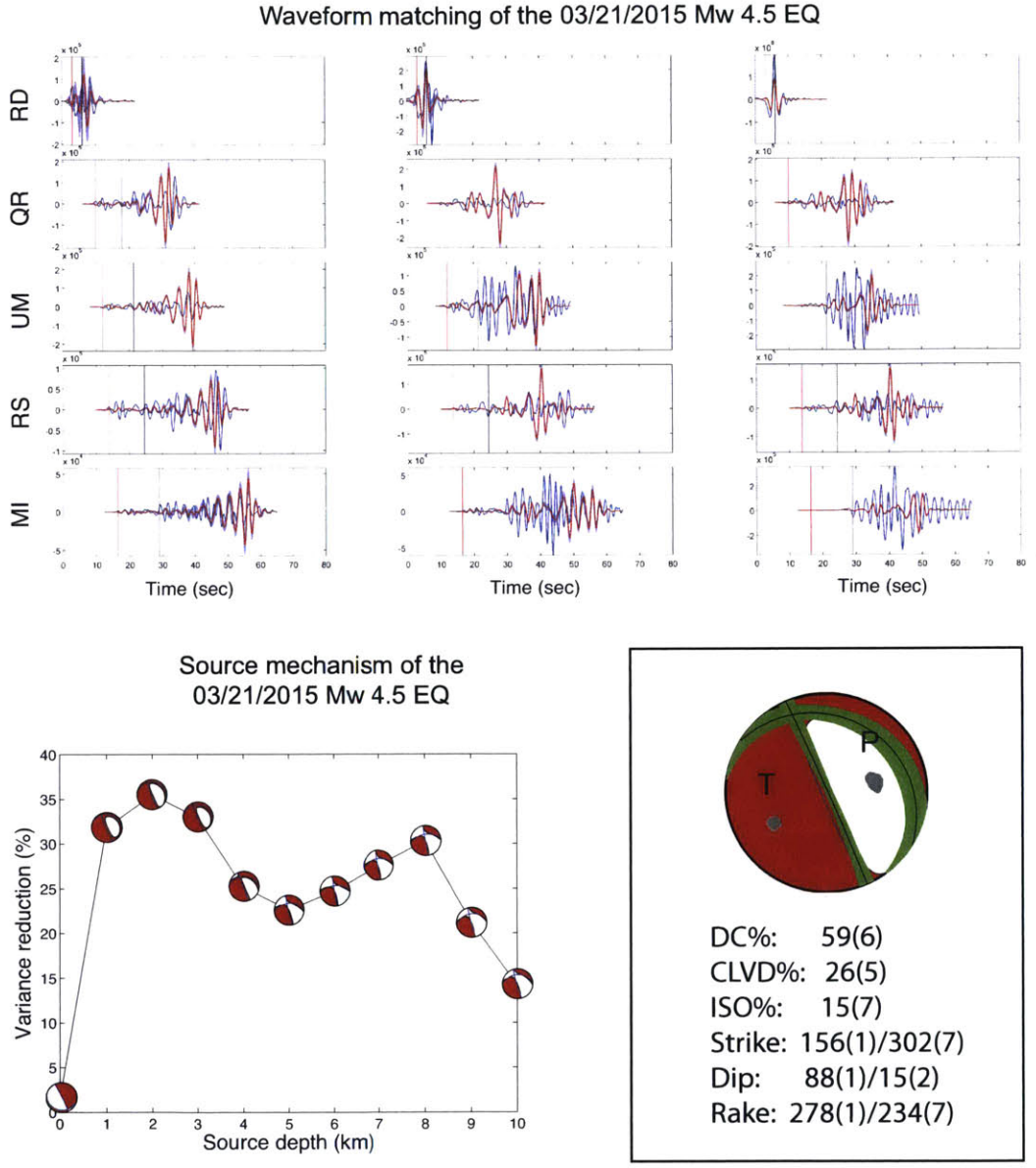

Figure 3-26: Results from VEL1 velocity model. Upper: The comparison of the real data (blue) and the mean posterior predicted waveform (red) for the Mw 4.5 earthquake at the best matching depth. The data are bandpass filtered by 0.1 to 0.5 Hz. Right: Variance reduction of waveform matching as a function of trial source depth. The resulted source mechanism of different trial depth are plotted as beach ball on the figure. The best source mechanism solution, presented as both beachball and text, is shown in the black frame.

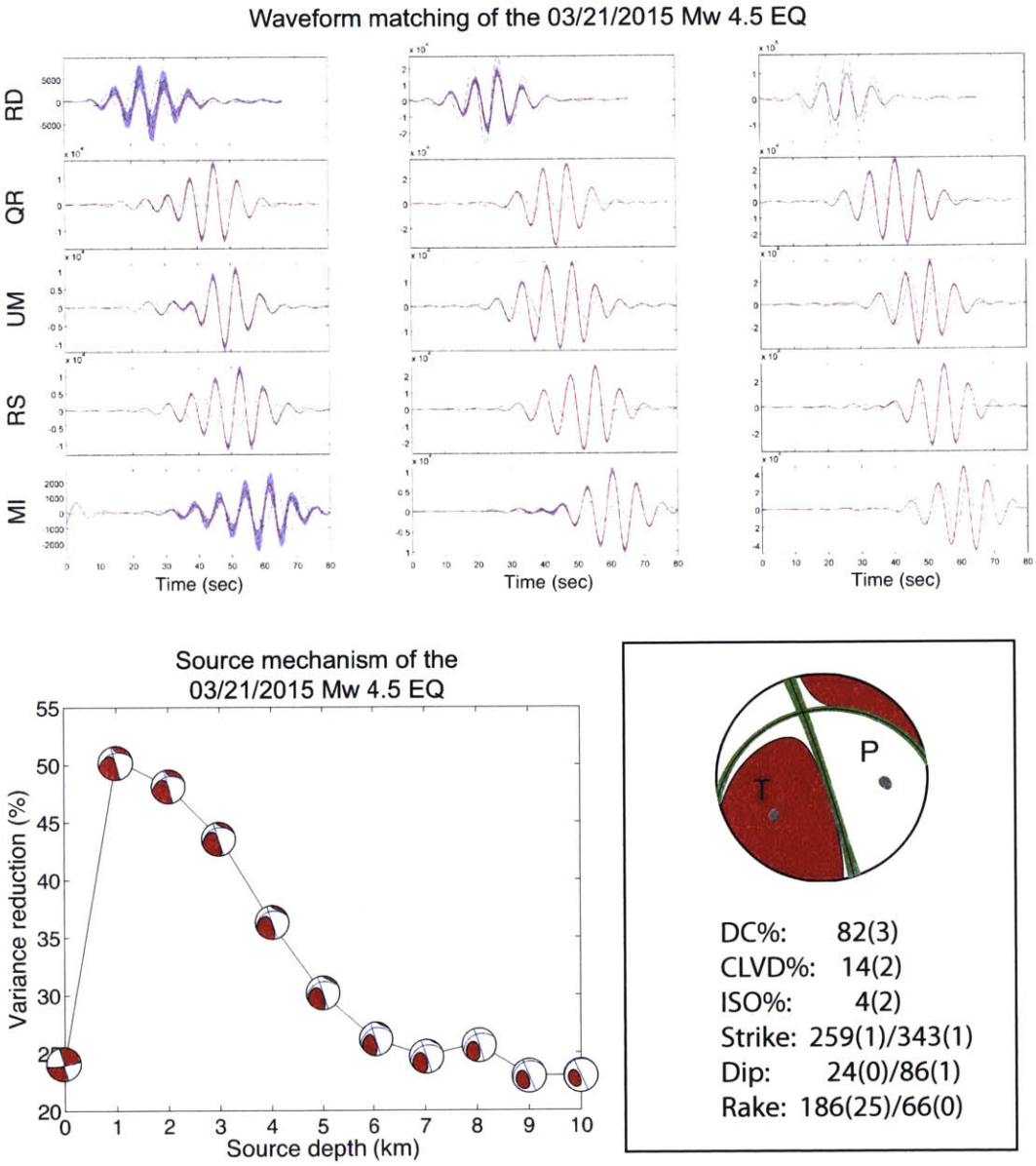

Figure 3-27: Results from VEL1 velocity model. Upper: The comparison of the real data (blue) and the mean posterior predicted waveform (red) for the Mw 4.5 earthquake at the best matching depth. The data are bandpass filtered by 0.1 to 0.15 Hz. Right: Variance reduction of waveform matching as a function of trial source depth. The resulted source mechanism of different trial depth are plotted as beach ball on the figure. The best source mechanism solution, presented as both beachball and text, is shown in the black frame.

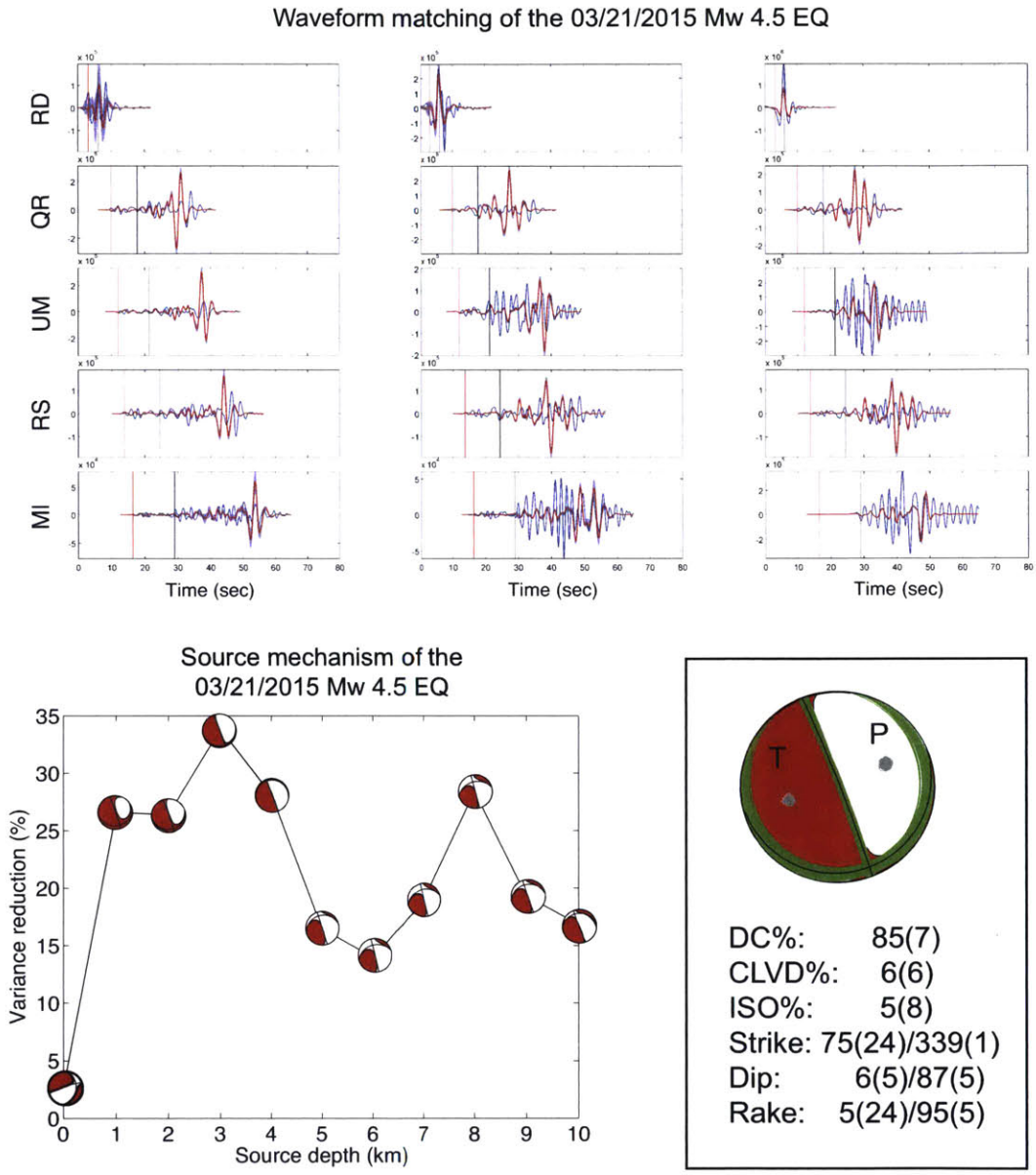

Figure 3-28: Results from VEL2 velocity model. Upper: The comparison of the real data (blue) and the mean posterior predicted waveform (red) for the Mw 4.5 earthquake at the best matching depth. The data are bandpass filtered by 0.1 to 0.5 Hz. Right: Variance reduction of waveform matching as a function of trial source depth. The resulted source mechanism of different trial depth are plotted as beach ball on the figure. The best source mechanism solution, presented as both beachball and text, is shown in the black frame.

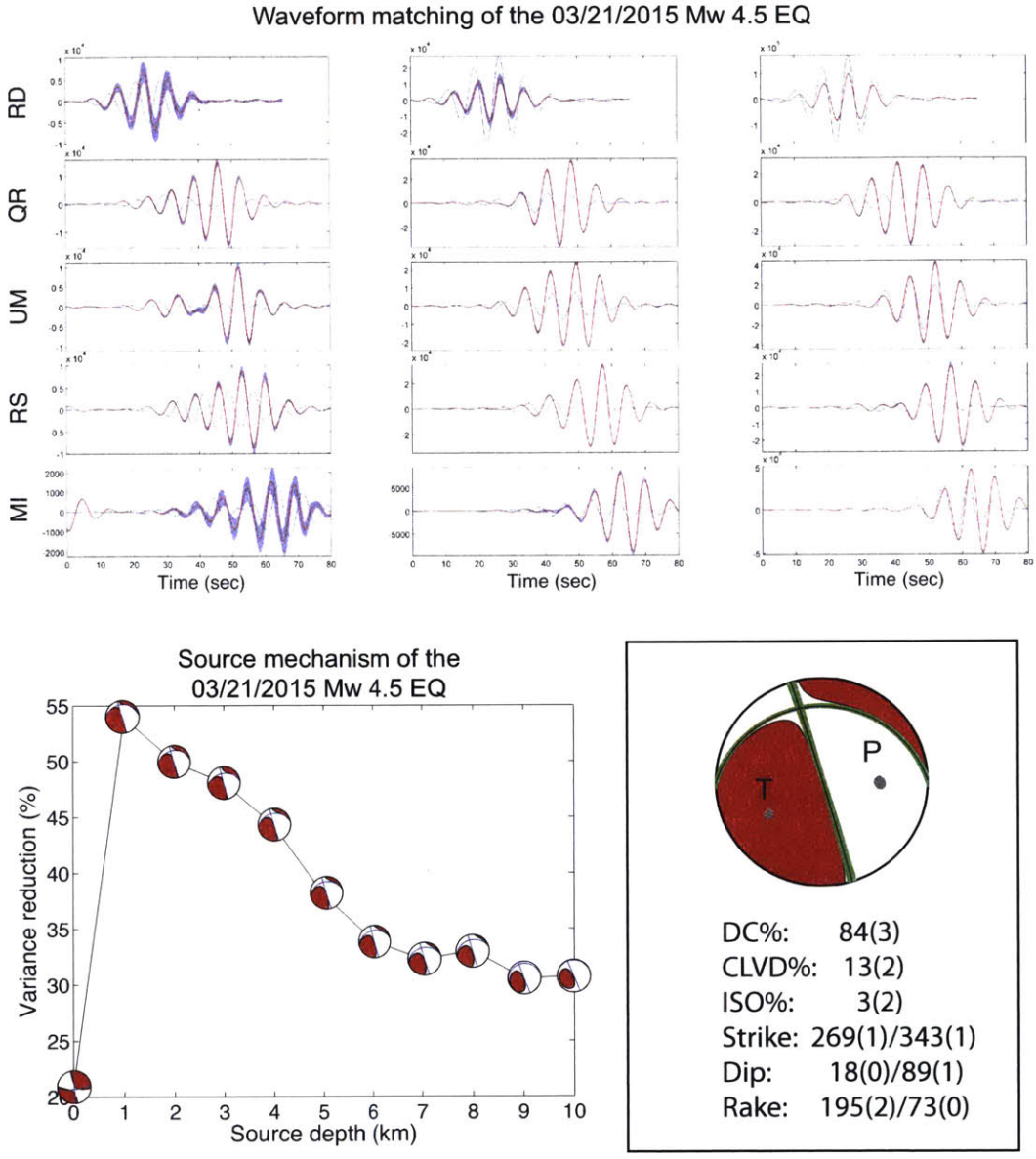

Figure 3-29: Results from VEL2 velocity model. Upper: The comparison of the real data (blue) and the mean posterior predicted waveform (red) for the Mw 4.5 earthquake at the best matching depth. The data are bandpass filtered by 0.1 to 0.15 Hz. Right: Variance reduction of waveform matching as a function of trial source depth. The resulted source mechanism of different trial depth are plotted as beach ball on the figure. The best source mechanism solution, presented as both beachball and text, is shown in the black frame.

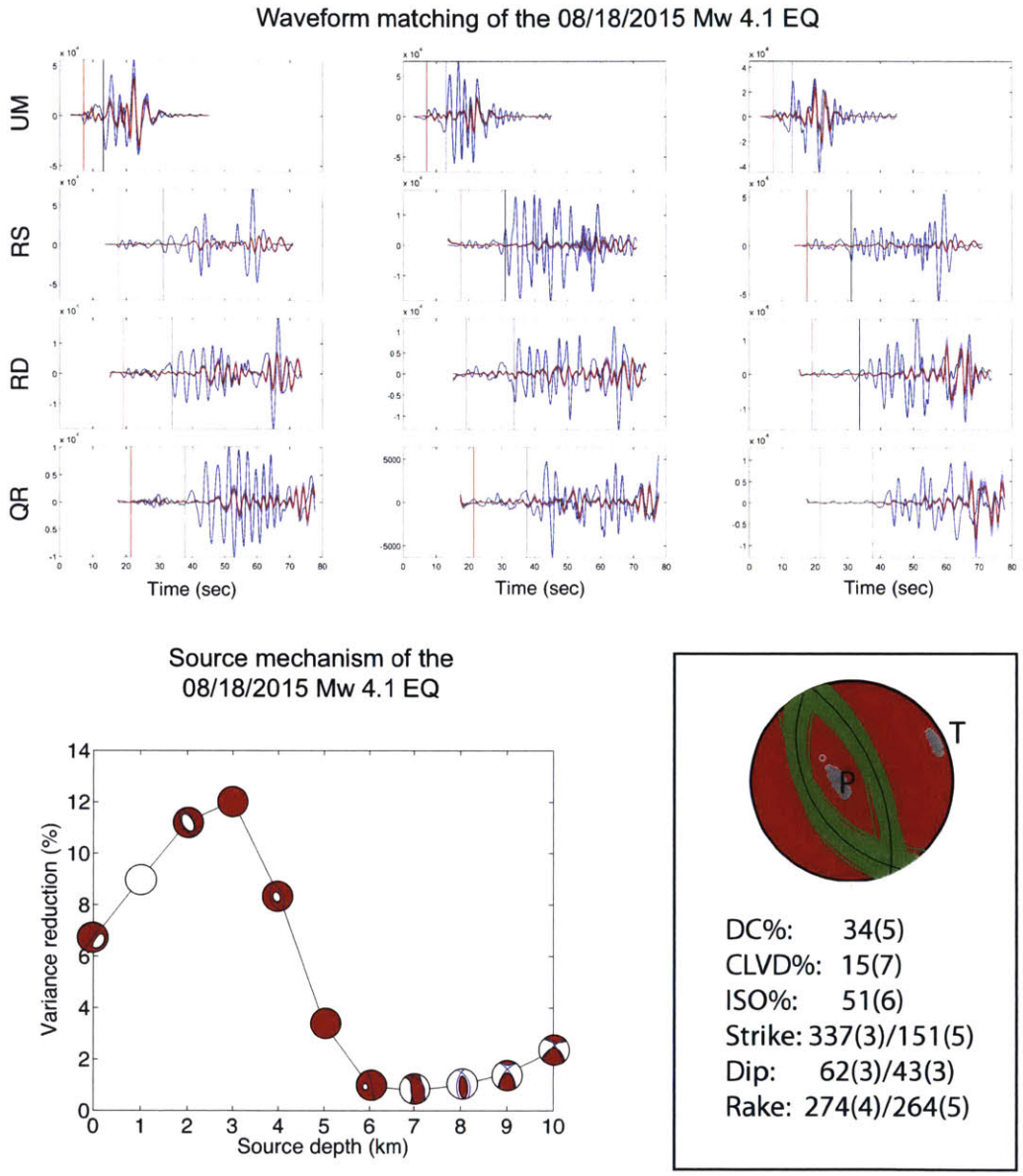

Figure 3-30: Results from KUW1 velocity model. Upper: The comparison of the real data (blue) and the mean posterior predicted waveform (red) for the Mw 4.1 earthquake at the best matching depth. The data are bandpass filtered by 0.1 to 0.5 Hz. Right: Variance reduction of waveform matching as a function of trial source depth. The resulted source mechanism of different trial depth are plotted as beach ball on the figure. The best source mechanism solution, presented as both beachball and text, is shown in the black frame.

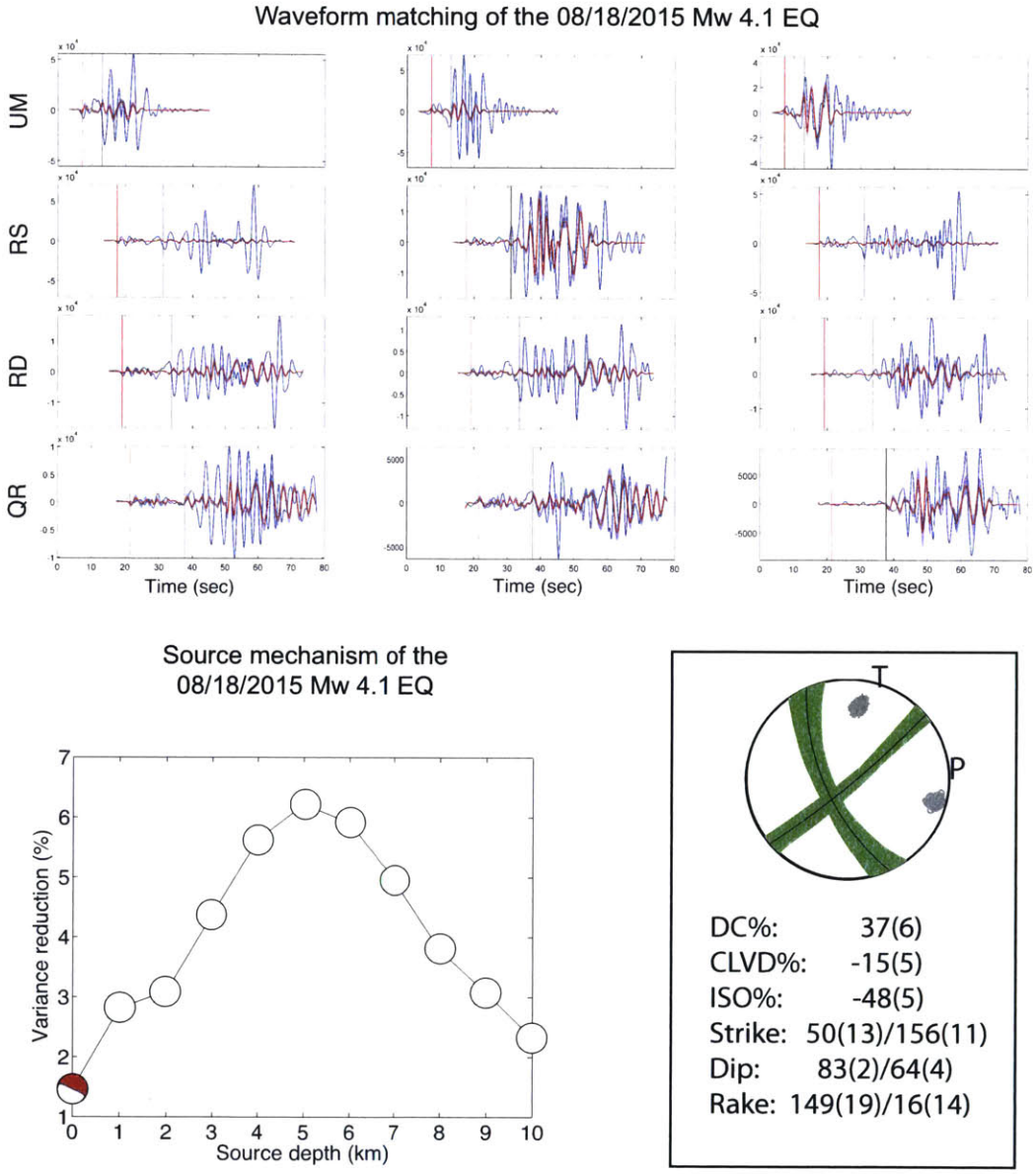

Figure 3-31: Results from VEL1 velocity model. Upper: The comparison of the real data (blue) and the mean posterior predicted waveform (red) for the Mw 4.1 earthquake at the best matching depth. The data are bandpass filtered by 0.1 to 0.15 Hz. Right: Variance reduction of waveform matching as a function of trial source depth. The resulted source mechanism of different trial depth are plotted as beach ball on the figure. The best source mechanism solution, presented as both beachball and text, is shown in the black frame.

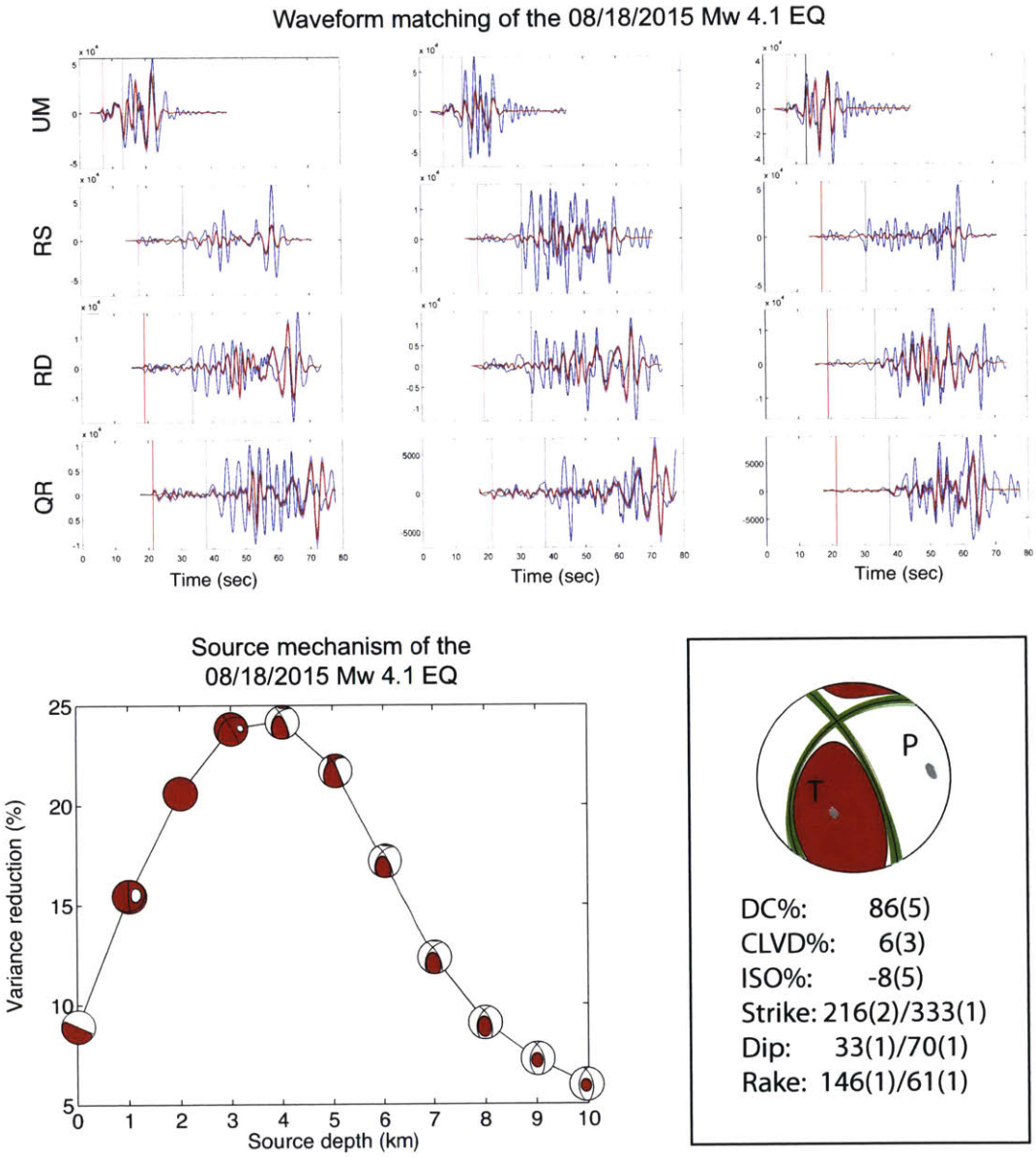

Figure 3-32: Results from VEL2 velocity model. Upper: The comparison of the real data (blue) and the mean posterior predicted waveform (red) for the Mw 4.1 earthquake at the best matching depth. The data are bandpass filtered by 0.1 to 0.5 Hz. Right: Variance reduction of waveform matching as a function of trial source depth. The resulted source mechanism of different trial depth are plotted as beach ball on the figure. The best source mechanism solution, presented as both beachball and text, is shown in the black frame.

3.3.3 Discussion

Triggering stress and damage of local earthquakes

Based on other examples, induced earthquakes oil field earthquakes generally occur on pre-existing faults and are triggered by pore pressure and stress changes caused by fluid injection or extraction (Sarkar, 2008; Li et al., 2011a,b). A detailed study of more than 5,000 earthquakes in an oil/gas field in Oman was carried out by Sarkar (2008), and Li et al. (2011a,b). It showed that the hypocenters of earthquakes were on pre-existing faults that were activated by stress changes due to fluid injection or withdrawal. The focal mechanisms were controlled by the regional tectonic stress fields (Li et al., 2011a,b).

Local earthquakes in Kuwait occurred generally close to oil fields in Northern and Southern Kuwait. These earthquakes occurred in Northern and Southern fields have similar waveforms. These best fitting depths (maximum variance reduction) are close to the typical reservoir depth – 2 to 4 km. The waveform-based Bayesian moment tensor inversion results of the 03/21/2015 Mw 4.5 and 08/18/2015 Mw 4.1 earthquakes show the northeast-southwest oriented maximum horizontal stress, which matches with the regional tectonic stress fields obtained from well log data. In addition, the strike direction of the fault plane solution - almost north-south - matches with the main structural elements in Kuwait. Thus, local earthquakes in Kuwait are most likely occurred on pre-existing faults and are induced by oil production activities. The fault mapped using the seismic reflection data cannot be obtained at the surface because of pliocene sediment cover. An unusual pattern of seismicity is the relative sparsity on Burgan field, the largest oil field in Kuwait. This may be due to the shallow depth of the reservoir, or relatively small production after the Iraq invasion.

The induced earthquakes, in regions where tectonic activity is low, are generally small events, with magnitudes Mw = 5 or less. However, these events, occurring in the reservoirs, generally are very shallow with focal depths. As a result, they could produce ground accelerations high enough to cause damage to local structures (Figure 3-33, 3-34,3-35). In Kuwait, where oil fields are close to populated areas, induced

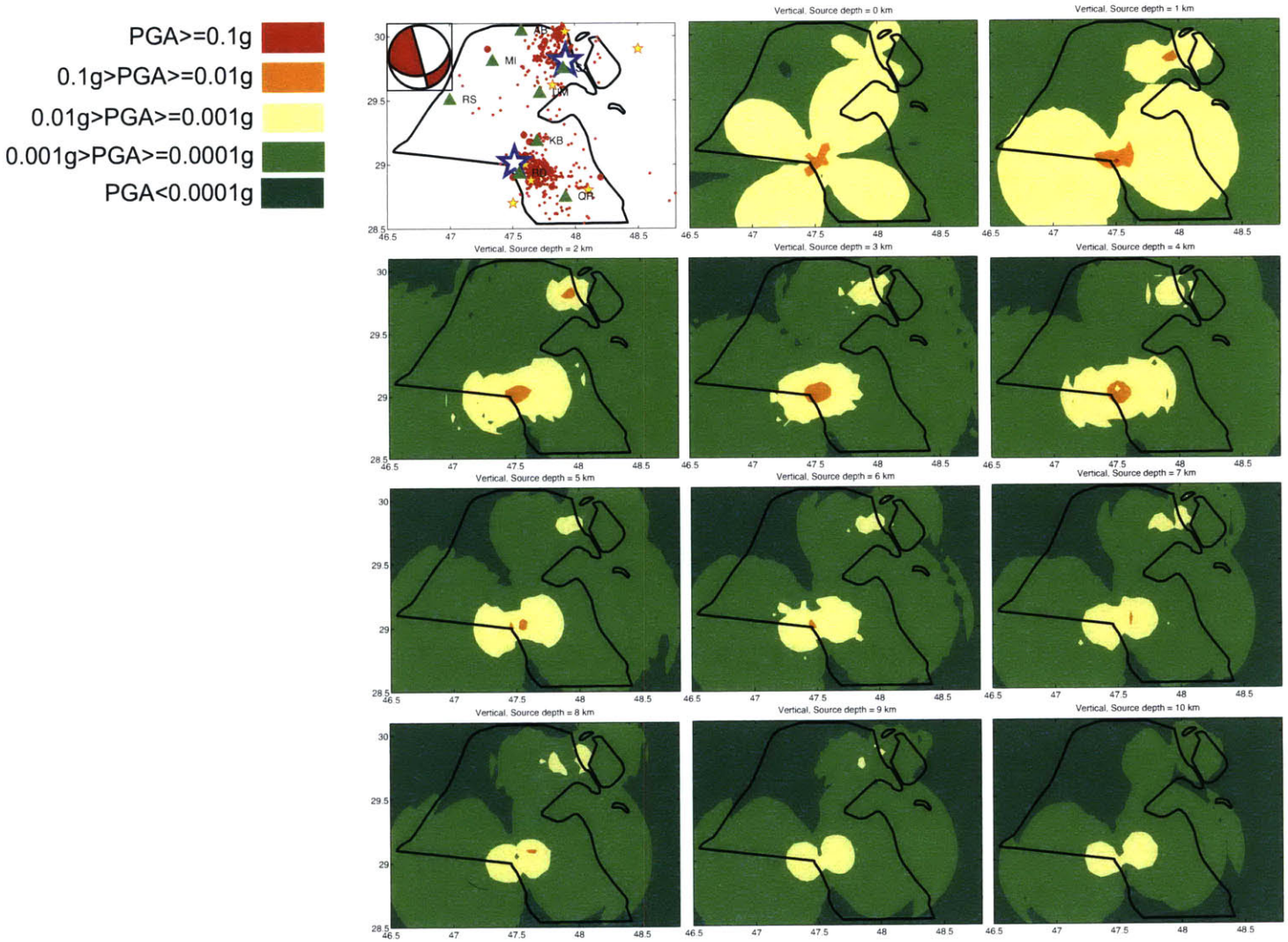

Figure 3-33: The vertical acceleration distribution in Kuwait due to a Mw 4.5 earthquakes in northern and southern a Mw 4.1 earthquake in Kuwait. The source depth varies from 0 km to 10 km.

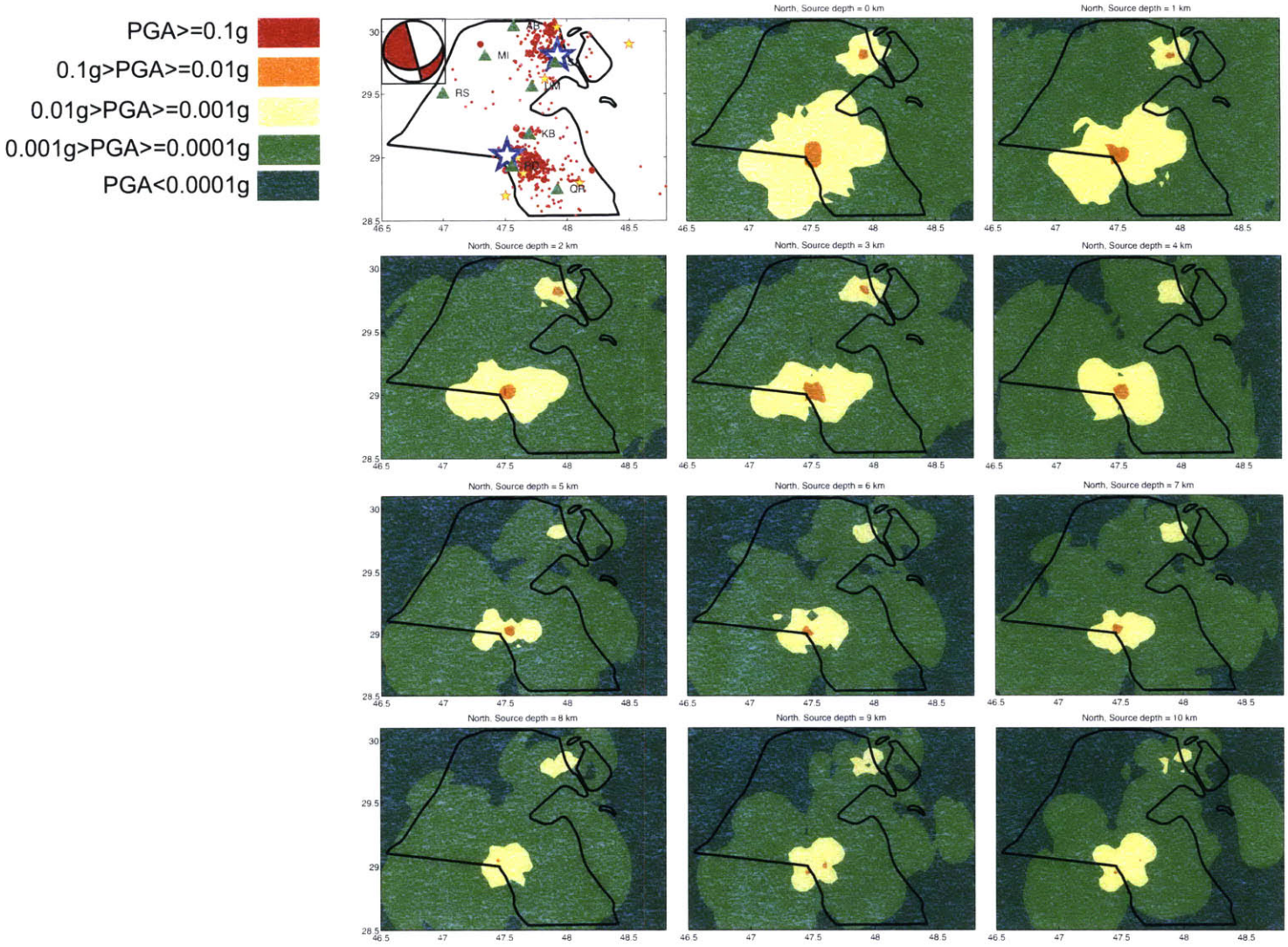

Figure 3-34: The north acceleration distribution in Kuwait due to a Mw 4.5 earthquakes in northern and southern a Mw 4.1 earthquake in Kuwait. The source depth varies from 0 km to 10 km.

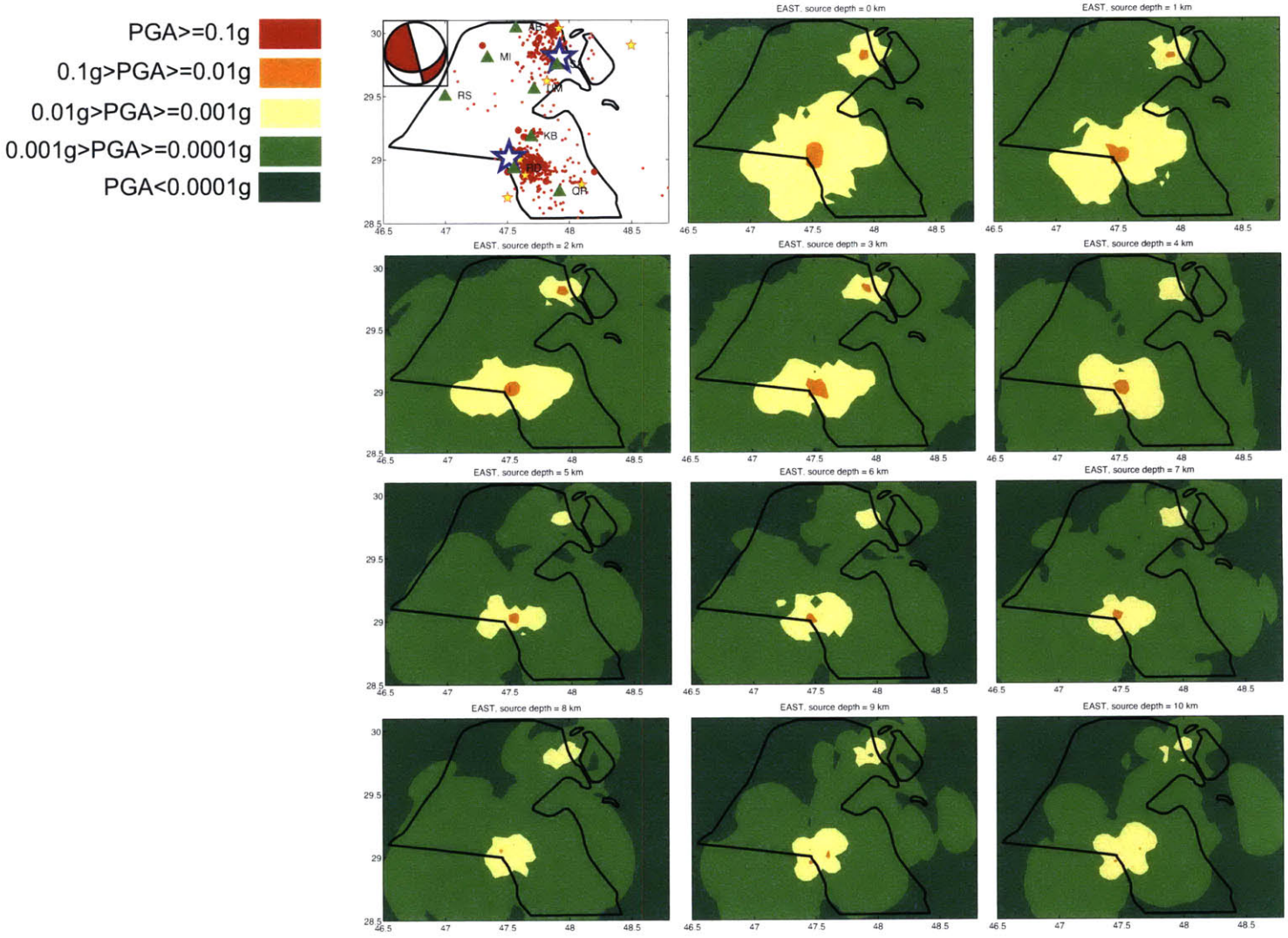

Figure 3-35: The east acceleration distribution in Kuwait due to a Mw 4.5 earthquakes in northern and southern a Mw 4.1 earthquake in Kuwait. The source depth varies from 0 km to 10 km.

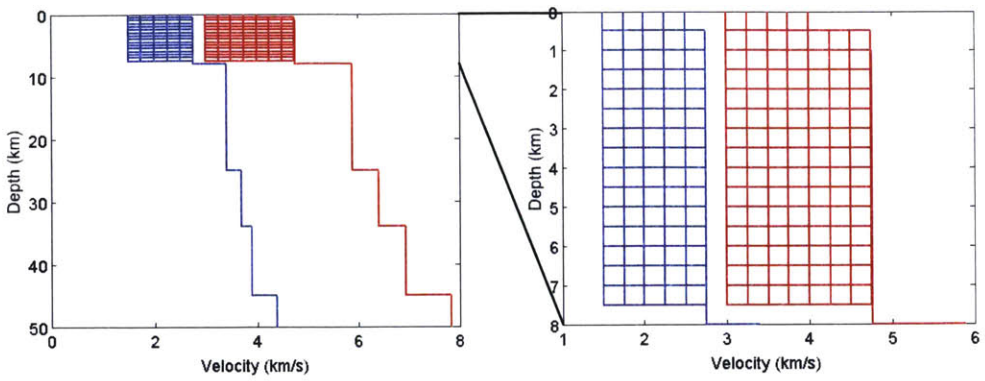

Figure 3-36: Left: The trial velocity model. We use KUW1 velocity model (Pasyanos et al., 2007) from 8 km to ∞. All the trial two-layer model from 0 to 8 km are plotted in the same figure; Right: Zoom in of the depth 0 to 8 km.

earthquakes could be hazardous to structures constructed without using seismic design criteria. The majority of older buildings in Kuwait could be affected by local earthquakes. However, we would not expect these induced earthquakes to be a hazard to new well-constructed structures.

Shallow structure in Kuwait

The shallow seismic structure in Kuwait needs to be better quantified. Based on the constraints from the sonic logging, all the possible trial velocity models are shown in Figure 3-36. The inclusion of the velocity model into the Bayesian moment tensor method would help to determine which velocity model is more likely to generate the typical seismograms in Kuwait.

Chapter 4

Characterization of Acoustic Emission During Fractures in Laboratory

4.1 Introduction

Fracturing of rock samples in the laboratory generates acoustic emissions (AE) – elastic energy related to very small "earthquakes". Acoustic emissions are of great importance in studying the fracturing mechanics because in laboratory experiments we can have the information about the stress conditions, the rock properties, and the fault plane geometry during the fracturing process. However, the low signal-to-noise ratio of the acoustic emission (AE) data, the high occurrence rate of AE events, and the difficulties of sensor calibrations make the event detection, locating, and source mechanism inversion difficult to implement.

The history of acoustic emission goes back to the middle of the 20th century, before the terminology "AE" was created. Obert and Duvall (1942) first detected small noise emitted from rock under compression and attributed these signals to microfractures in the rock. Kaiser (1950) recorded signals from the tensile specimens of metallic materials. Later, Schofield (1961) used the terminology AE in his work.

Since the 1960's, much subsequent work has contributed to the development of AE techniques and applied the AE techniques to to diverse engineering and scientific areas (Drouillard and Laner, 1978; Drouillard, 1987, 1996; Grosse and Ohtsu, 2008).

During the past 50 years, fracture characterization has become one of the most important application areas of AE techniques. Many early studies from 1960's to 1970's have used AE techniques to investigate fracturing and deformation processes of rocks (Savage and Mansinha, 1963; Scholz, 1967, 1968a,b; Lockner and Byerlee, 1977). Savage and Mansinha (1963) studied the radiation pattern of AE due to a tensile failure in a 2-D glass plate. Scholz (1968b) determined the microfracture frequencies by AE event detection, and AE was also located in space by Scholz (1968a) and found to locate fractures during the compression of granite. Lockner and Byerlee (1977) published the pioneering work of locate hydraulic fractures using AE. Since this early start of the laboratory study of seismic processes, much work has been done to learn the slip processes of tectonic earthquakes using the laboratory analog fracturing process, which was detected by AE (W Goebel et al., 2013; Kwiatek et al., 2014).

Recently, with the increasing interest in the hydraulic fracturing in unconventional oil/gas fields, AE-based laboratory hydraulic fracturing studies have drawn new attention in both academia and industry. Stanchits et al. (2011) studied the fracturing of porous rock induced by fluid injection. Ishida et al. (2012) injected supercritical liquid CO2 into a borehole inside rock samples and monitored the AE due to hydraulic fracturing. Fu et al. (2015) conducted an experimental study on the interaction between hydraulic fractures and partially-cemented natural fractures. Hampton et al. (2015) investigated the fracture dimension when the laboratory hydraulic fracture interacted with a natural discontinuity. Goodfellow et al. (2015) studied the hydraulic fracture energy budget from the laboratory AE study.

Efficient and reliable detection, location, and source analysis methods for AE are crucial to produce fast and accurate results. The similarity of AE and earthquakes suggests it a possible method to study earthquake mechanism (Scholz, 1968a). Also, methods developed in modern seismology can be used to improve the AE analysis.

For event detection, Swindell and Snell (1977) developed a processor automatic signal detection system. McEvilly and Majer (1982) introduced an automated seismic processor for microearthquake networks. Earle and Shearer (1994) used an automatic-picking algorithm to characterize global seismograms . Maeda (1985) suggested a method for reading and checking phase times in an auto-processing system of seismic wave data. Kao and Shan (2004) introduced the source-scanning algorithm to map the distribution of seismic sources in time and space. Kurz et al. (2005) summarized the strategies for reliable automatic onset time picking of AE. All the algorithms in that paper originated from seismic event detection.

For earthquake location, Lomax et al. (2000) developed a Bayesian location algorithm to determine the location, as well as the uncertainties. A double difference location algorithm was introduced to mitigate the effects of an inaccurate velocity model on location and improve the accuracy of the relative location (Waldhauser and Ellsworth, 2000). Recent studies for microseismicity and tremor earthquakes have produced more efficient location algorithms dealing with a large data set with low signal-to-noise ratio. Zhang et al. (2014) introduced a new method for earthquake depth determination by stacking multiple-station autocorrelograms. Zhang and Wen (2015) suggested an effective method for small event detection and location. Grigoli et al. (2013) developed an automated seismic event location by travel-time stacking. Frank and Shapiro (2014) introduced an automatic detection of low-frequency earthquakes (LFEs) based on a beamformed network response location.

For the AE source analysis, the most common method used the first-P polarity and the moment tensor inversion method using the first-P amplitude (Pettitt, 1998; Graham et al., 2010). Although the first-P amplitude moment tensor inversion methods are also used in seismology, many studies of microseismicity used the waveform-based moment tensor inversion method to determine the source mechanism (Li et al., 2011a,b; Song and Toksöz, 2011; Gu et al., submitted). The goal of this chapter is to characterize fractures in laboratory-scale rock samples ($\sim$ cm) using the analysis methods from seismology. In this study, I implemented several event detection, location, and moment tensor inversion algorithms to the AE data from the

fracturing experiment of Berea sandstone. That fracturing experiment was conducted using the newly-built triaxial compressional machine at MIT. The AE techniques has just been implemented in that machine, and the calibration and testing are just being done. The data shown in this chapter is the first AE aquisition from the new system.

4.2 Experimental Data

4.2.1 Laboratory system

The AE data are collected from the newly-built AutoLab 1500 laboratory system and the National Instrument (NI) data acquisition system at the rock mechanics lab at MIT (Figure 4-1a). The AutoLab 1500 includes: 1) A pressure vessel and the associated pressure intensifiers to generate confining stress and piston to generate stress on a test specimen (Figure 4-1b); 2) An electronics console that interfaces with the mechanical system to precisely control the state of stress and to condition and amplify signals from the transducers and devices measuring force, pressure, displacement, strain, temperature, velocity, and resistivity; and 3) A data acquisition system that generates reference signals to control the equipment, to acquire data, and to process the data collected on each experiment (New England Research: AutoLab 1500 Instruction Manual).

The pressure vessel is divided into two chambers separated by a moveable piston (Figure 4-1c). The specimen resides in the lower pressure chamber, which replicates the overburden pressure. The higher pressure in the upper chamber moves the piston into contact with the sample assembly. When the pressure in the upper chamber is greater than that in the lower chamber, a directional force is applied to the specimen.

The piezoelectric (PZT) sensors are attached to the rock sample, and connected to the NI data acquisition systems to collect AE data. The dominant response frequency range of the PZT crystal is between 300 kHz to 1 MHz.

4.2.2 Fracturing experiment

The AE data used in this Chapter were from Berea sandstone fracturing experiments. The sample was Berea sandstone machined to a cylinder with the diameter of 36.43 mm and length of 76.7 mm. The confining pressure and differential pressure applied to the sample as a function of time during the whole compression process is shown in Figure 4-2. The light blue rectanguler marked in Figure 4-2 shows the time period when the main fracturing happens. The large sound related to this fracturing was heard clearly in the lab. The P velocity, measured at the confining pressure (P_c) of 10.0 MPa, and differential stress (P_d) of 2.0 MPa, is 3800 m/s, and the average S velocity at the same pressure condition is 2300 m/s.

Eight PZT sensors were placed over the surface of the cylinder. The distribution of the position of sensors is shown in Figure 4-5. The AE data has been collected from the beginning of compression, i.e. time = 0 sec, until the time = 420 sec. We separated the whole AE signal series into 256 segments. Figure 4-6 shows the segments of the AE data including the main fracturing (left), and the segment just after the main fracturing (right). The large spike on the left corresponding to the main fracturing of the Berea sample.

To illustrate how the acoustic energy changed with the applied stress, we defined the acoustic intensity (AI) as

$$AI = \int_{T_{win}} u(t)^2 dt \tag{4.1}$$

where $u(t)$ is the AE signal as a function of time, and T_{win} is the integral time window. Comparing the trend AI and stress, it is obvious that the AI had a huge jump when the differential stress dropped (Figure 4-7). The AI measured by the eight sensors has a consistent trend, although the energy levels for different sensors are different. This may be because the eight sensors had different responses to the fracturing emitted acoustic waves, or due to differences of transducer coupling.

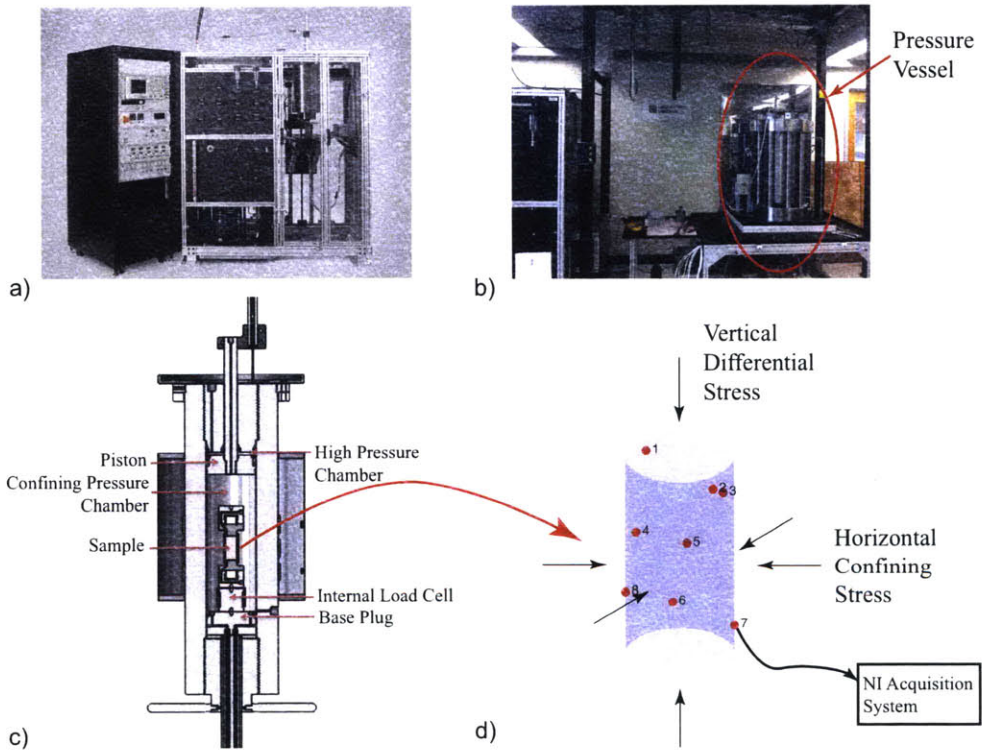

Figure 4-1: The schematic of the experimental system. a) The AutoLab 1500 laboratory system (New England Research: AutoLab 1500 Instruction Manual); b) The photo of the pressure vessel taken in the rock mechanics lab at MIT; c) The schematic of the pressure vessel (New England Research: AutoLab 1500 Instruction Manual). d) The schematic of the cylindrical rock sample. The red circles show the position of the sensors on the surface of the cylinder. The sensor is connected to the NI acquisition system to collect the AE signals.

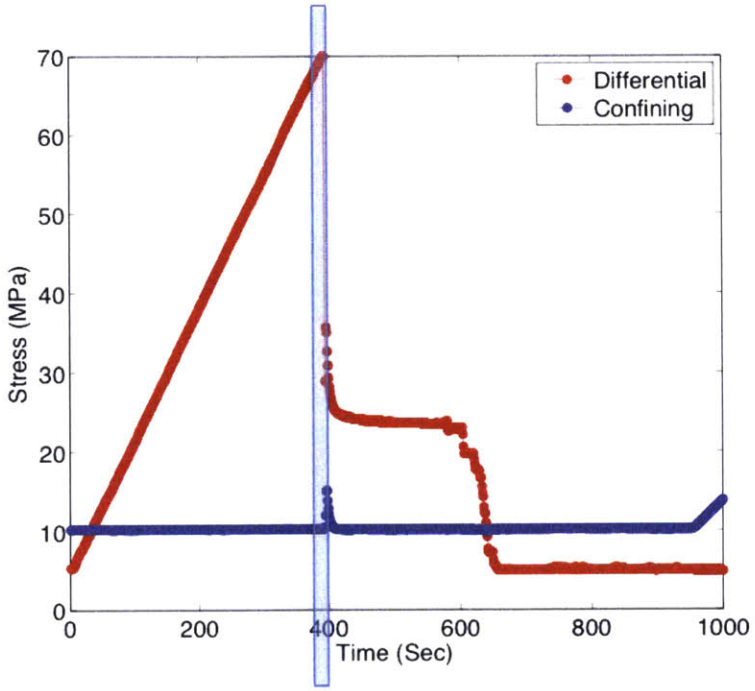

Figure 4-2: The confining pressure and differential pressure applied to the sample as a function of time during the whole compression process. The red line denotes the differential pressure, and the blue line denotes the confining pressure. The light blue rectanguler shows the time slot when the main fracturing happened.

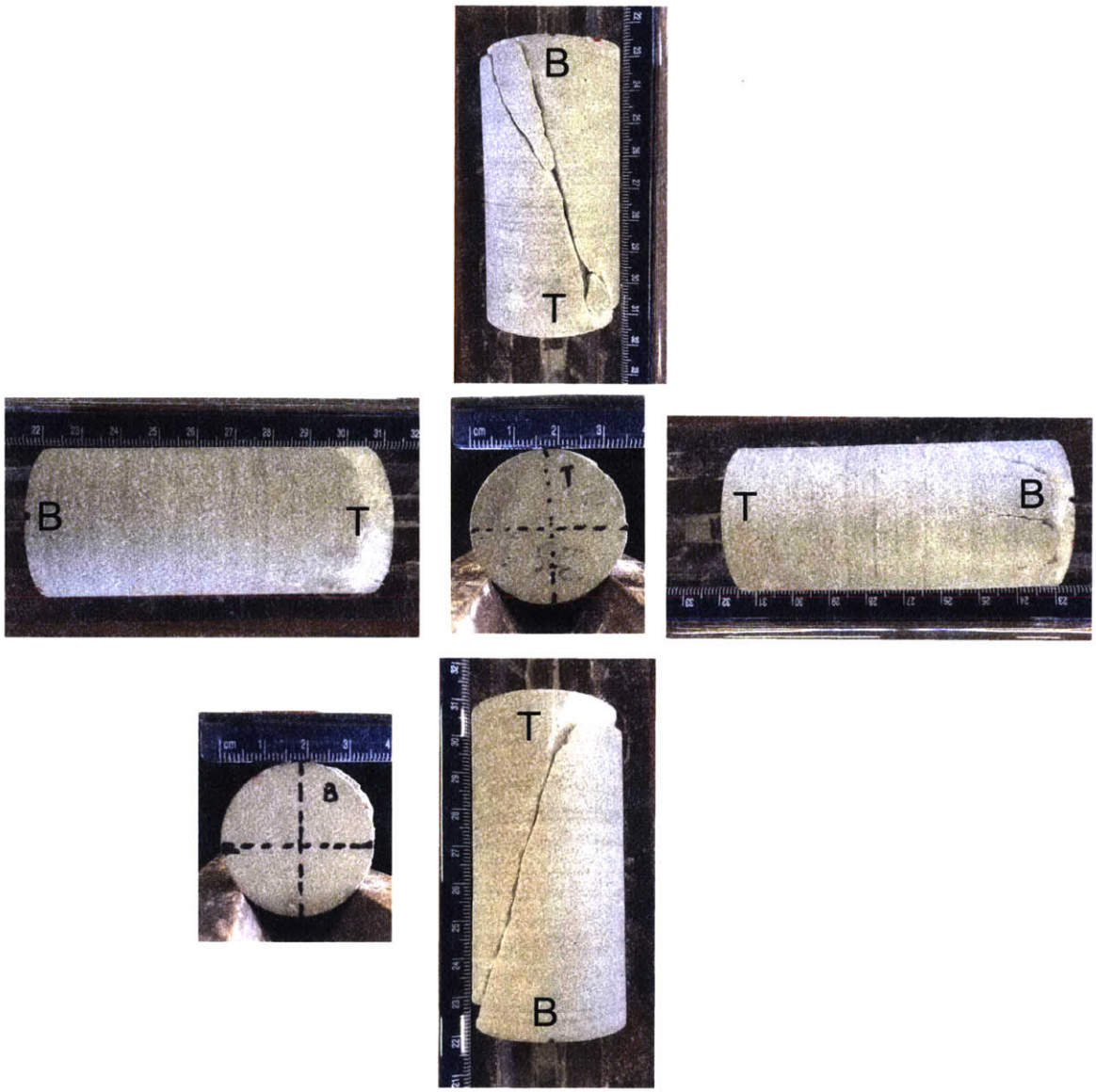

Figure 4-3: The photo of the fractured Berea sandstone in different views. "T" means the top part of the specimen, and "B" mans the bottom part of the specimen.

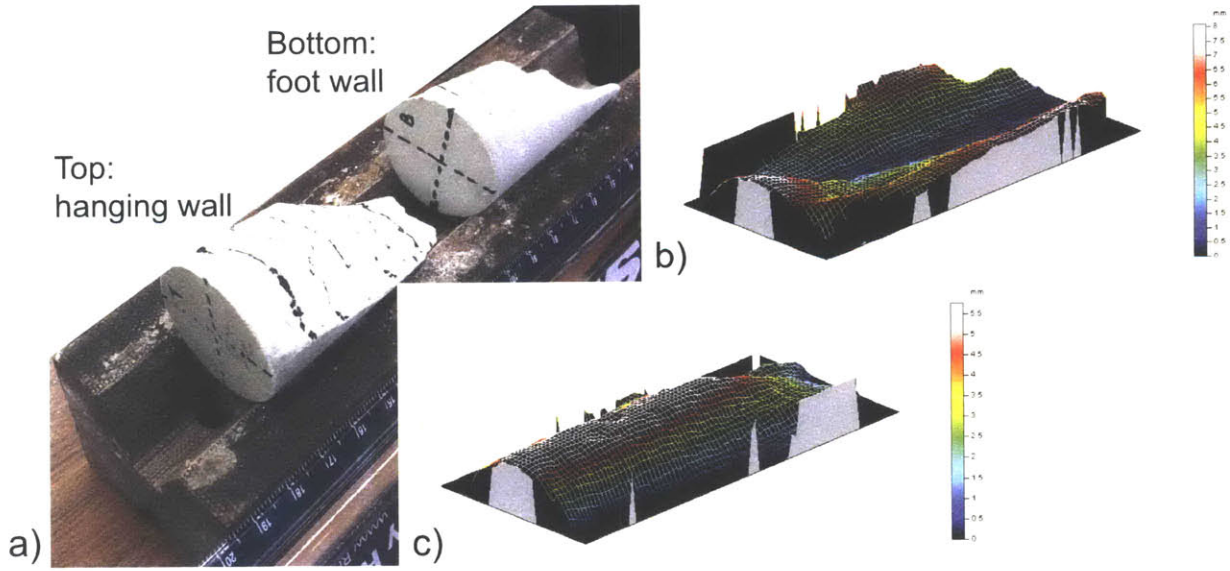

Figure 4-4: The fault plan scan for the top and bottom part of the sample. a) The photo of the top (hanging wall) and bottom (foot wall) part of the sample; b) The fault plane topographic scan of the hanging wall; c) The fault plane topographic scan of the foot wall.

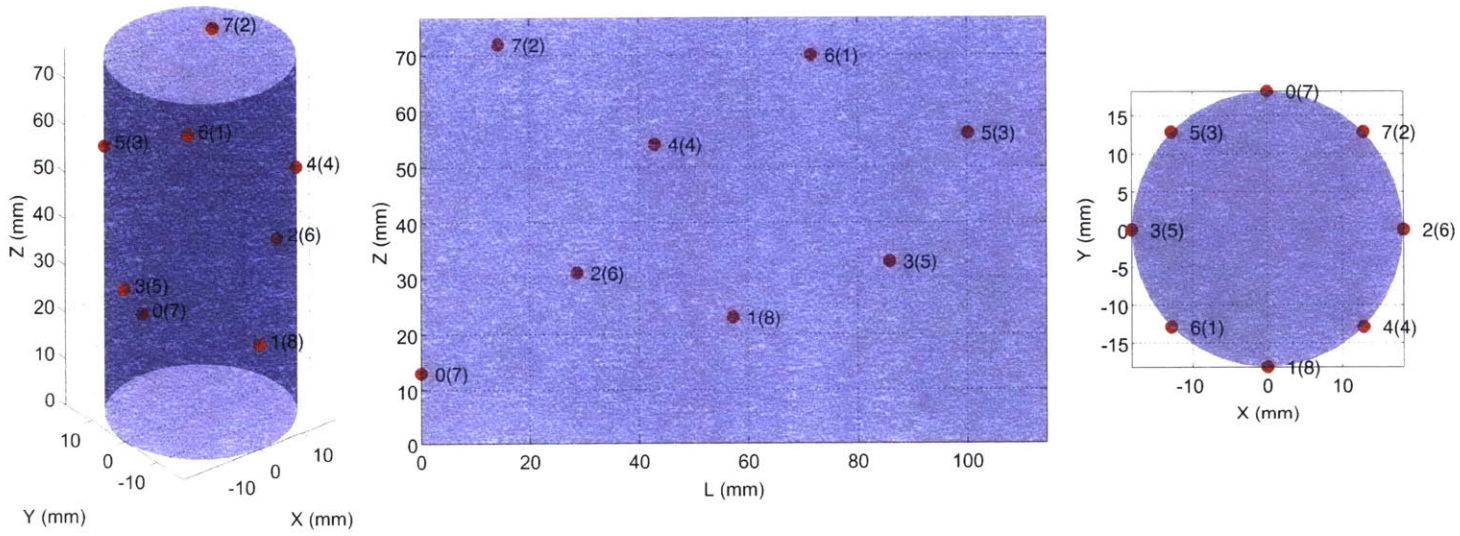

Figure 4-5: The scheme of the experimental system. Left: 3D view of the Berea cylinder. The red circles show the position of the eight PZT sensors; Middle: Flat view of the expansion of the cylinder; Right: Top view of the cylinder.

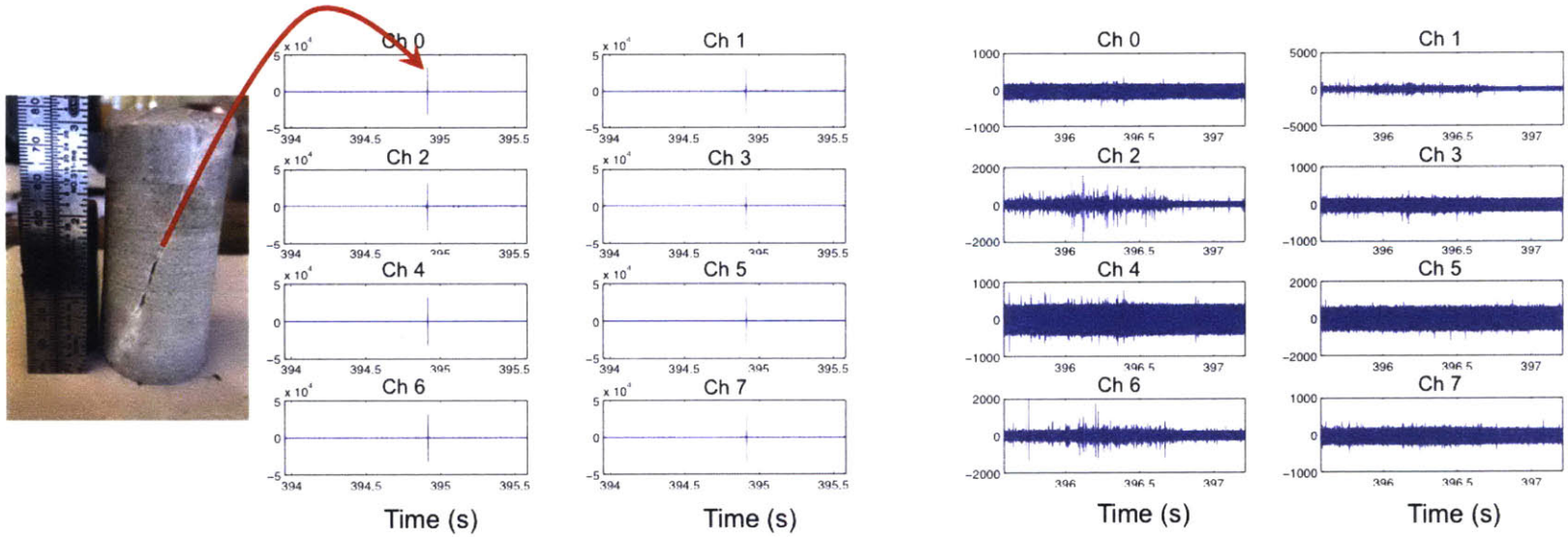

Figure 4-6: The example of AE waveform data. The inset of a fractured rock cylinder is the Berea sandstone. The left panel, containing eight waveform subplots, denotes the AE data from eight sensors corresponding to the time window when the rock was fractured. The right panel shows the AE data at the time window just after the fracturing window.

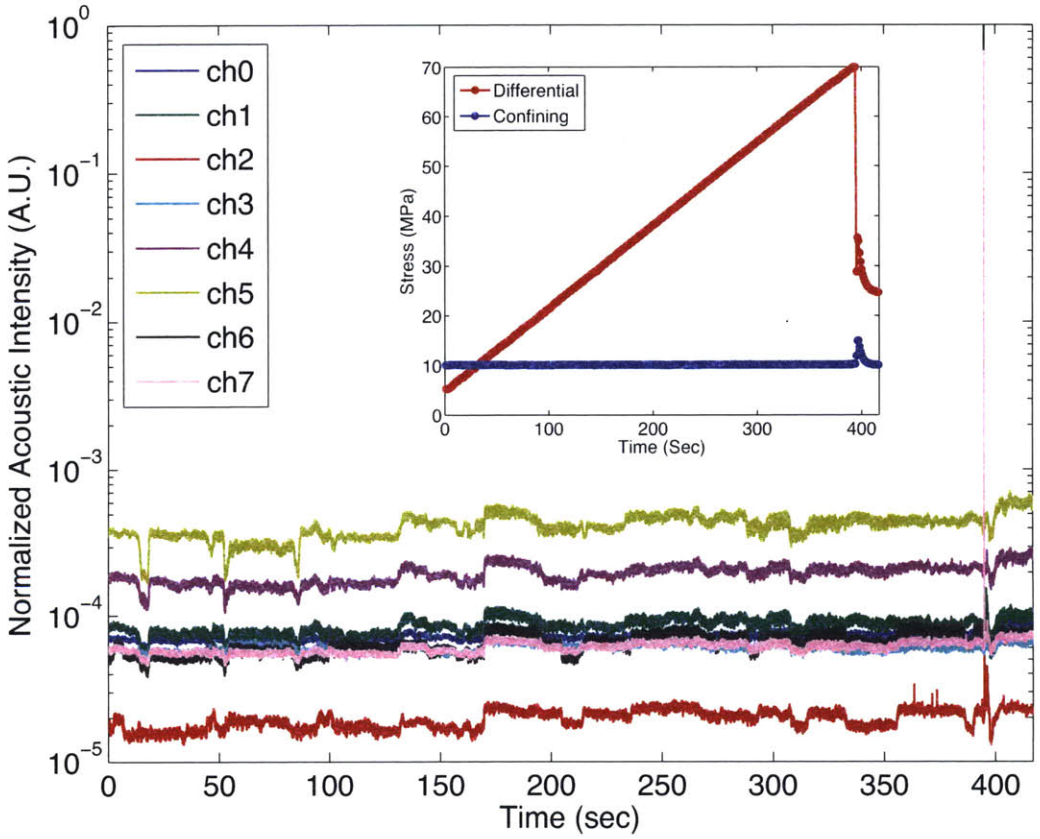

Figure 4-7: The AI of eight channels for the whole AE collection period. The confining pressure and differential pressure applied to the sample as a function of time during the AE signal collection period is shown in the inset.

4.3 Methodology

The processing and interpretation of the AE data implemented in this Chapter includes automatic event detection, location, and moment tensor inversion. We introduced three automatic event detection methods, three location methods, and two moment tensor inversion methods in this part.

4.3.1 Automatic event detection

STA/LTA

The STA/LTA method is widely used for event detection in both seismology and acoustic emission data analysis (Swindell and Snell, 1977; McEvilly and Majer, 1982; Earle and Shearer, 1994). The STA/LTA means the STA over LTA, where STA denotes the short-time average, and the LTA denotes the long-time average:

$$STA = \frac{1}{N_{STA}} \sum_{i=1}^{N_{STA}} |u_i| , \tag{4.2}$$

and

$$LTA = \frac{1}{N_{STA}} \sum_{i=1}^{N_{LTA}} |u_i| . \tag{4.3}$$

The selection of the STA and LTA window, and the threshold is important to obtain accurate onsets. Normally, the STA window should be short enough to resolve the event, and the LTA window should be long enough to average the local noise. The STA/LTA threshold is also tricky to detect the events. Low thresholds would result in the false alarm of arrivals, while high thresholds would result in missing the events. We applied the STA/LTA picker to a waveform sample containing four events (Figure 4-8). The picked onsets of the four events are picked accurately when the STA, LTA window and threshold are chosen reasonably.

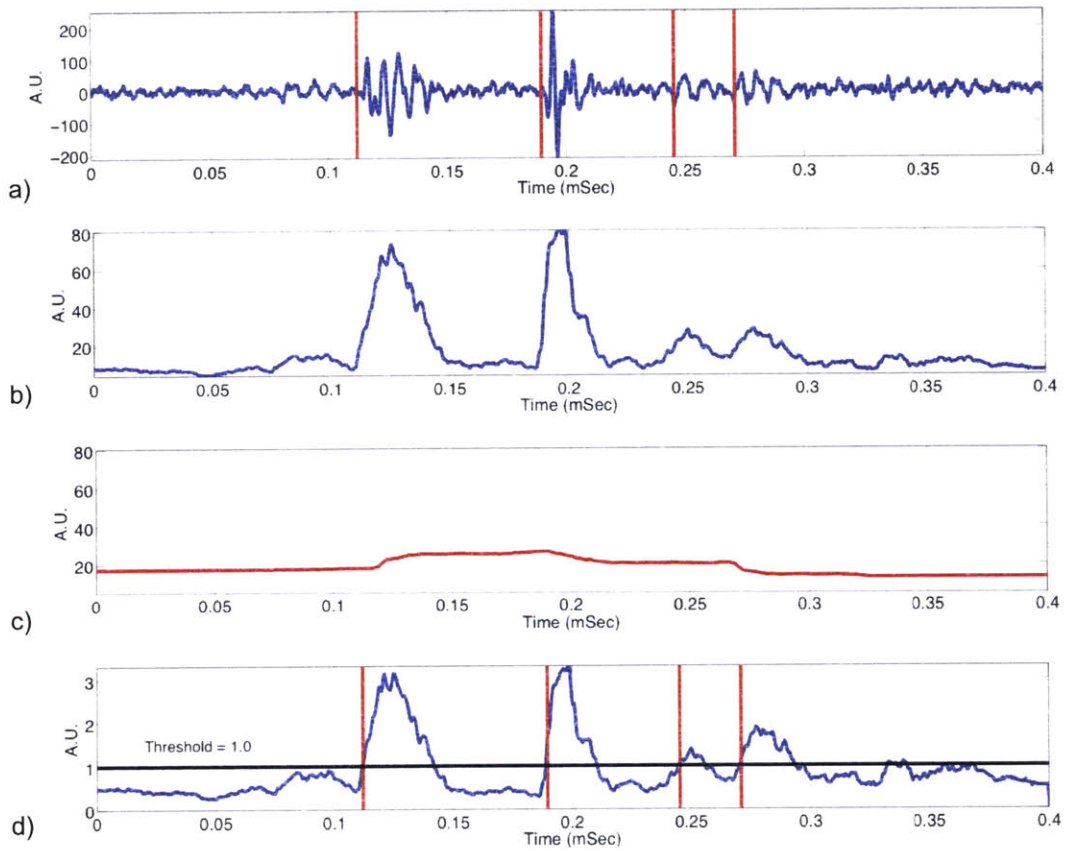

Figure 4-8: a) Event detection results from STA/LTA method. The red lines marked in the same figure of the waveform sample show the picked onset. b) STA as a function of time; c) LTA as a function of time; d) STA/LTA as a function of time.

AIC

The Akaike Informative Criteria (AIC) has been used to determine the onset of signal in seismology and acoustic emission (Maeda, 1985; Kurz et al., 2005). The equation of the AIC calculation is

$$AIC(t_w) = t_w \cdot \log(var(R_w(t_w, 1))) + (T_w - t_w - 1) \cdot \log(var(R_w(1 + t_w, T_w))), \quad (4.4)$$

where t_w is the time index, ranging from all the samples of the waveform R_w, the signal series in a window w. $R_w(t_w, 1)$ and $R_w(1 + t_w, T_w)$ denote the samples ranging from time index t_w to 1 and the samples ranging from time index $1 + t_w$ to T_w, respectively. The global minimum of the AIC function picked the onset of the signal. The AIC works well if we assume the waveform window only contains one onset (Figure 4-9a), i.e., single-event picking. The onset picked by AIC is almost the same as the manual picked one.

We also tried to apply the AIC calculation to the window, which contains several separate arrivals as in Figure 4-9b, and picked the local minimum of the smoothed AIC function. It is obvious that the picks are off the true onsets.

SSA

The SSA, referring to "Source Scanning Algorithm", is a waveform-based location algorithm used in seismic tremor location (Kao and Shan, 2004). Similar to AE, the tremor signal generally has low signal-to-noise ratio and is hard to detect and locate accurately. The SSA method constructs a brightness function

$$br(x, y, z, t) = \sum_{i=1}^{s} \frac{u_i^2(t + \Delta\tau_i(x, y, z))}{\sum_{t=1}^{t_w} u_i^2(t + \Delta\tau_i(x, y, z))} \quad (4.5)$$

where $br(x, y, z, t)$ is the brightness function dependent on the source location (x, y, z) and the arrival time t, $\Delta\tau_i(x, y, z))$ is the relative moveout of station i, s is the station number, and t_w is the length of the waveform window. A grid search was applied over

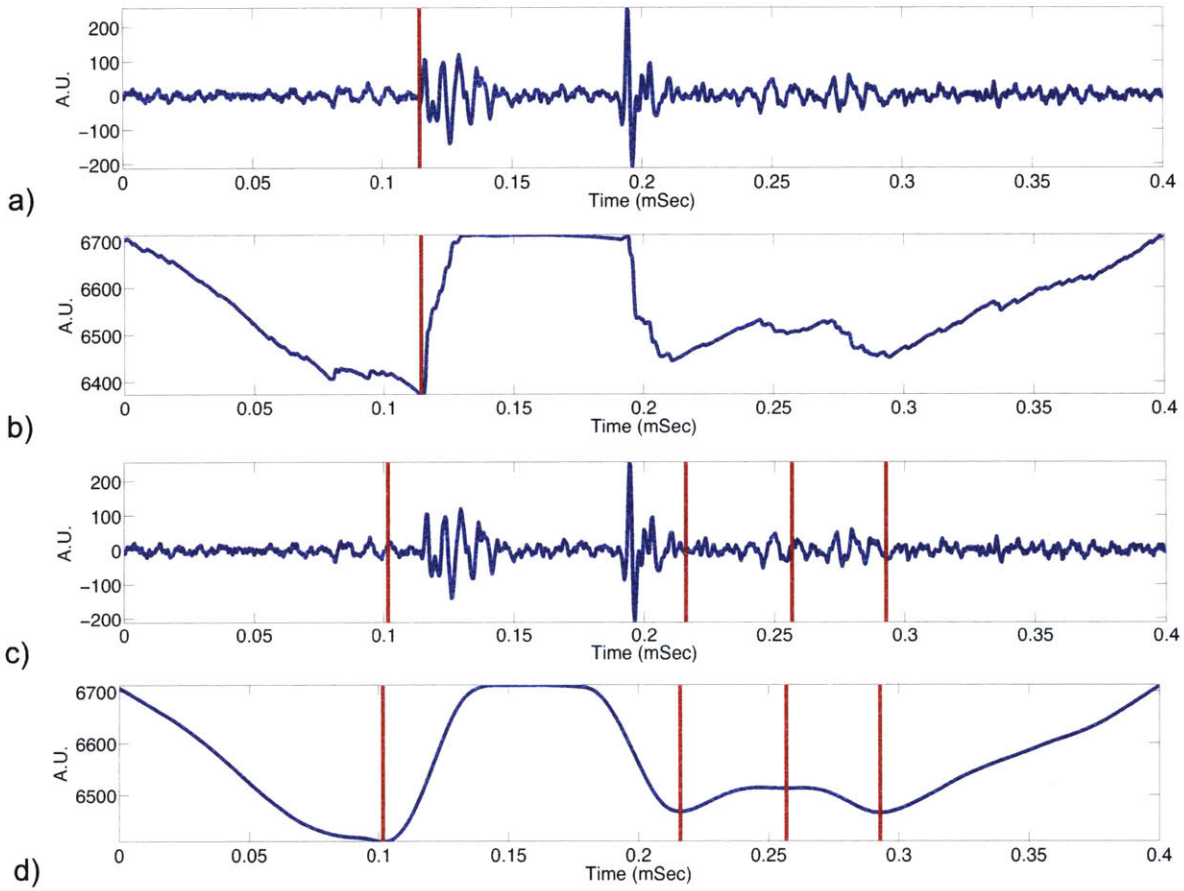

Figure 4-9: a) AIC picked onset marked with a red line on the waveform sample and AIC function with the global minimum marked by a red line for the single-event picking. b) IC picked onset marked with a red line on the waveform sample and AIC function with the global minimum marked by a red line for the multi-event picking.

Table 4.1: SSA Location results for the synthetic waveforms

	True Value	No Noise	50 % Gauss
X (mm)	-1.9	-2.2	-7.2
Y (mm)	-6.2	-6.2	-7.2
Z (mm)	32.6	32.0	37
t- pick (ms)	0.14	0.14	0.14

all the possible source location, and arrival time space. The $br(x, y, z, t)$ would have the maximum value when the trial location and arrival time is predicted correctly, since all the waveforms from different stations will be shifted by the accurate moveouts and aligned at the same time. The SSA can not only detect the event, but also locate the event.

I illustrated the SSA algorithm using synthetic tests. The synthetic AE system is shown in Figure 4-10. One synthetic event was set inside the modeled cylinder with the same size as the experiment. We synthesize the received waveforms of the eight sensors due to that event. The synthetic waveforms include one set without noise contamination, and one set with 50% Gaussian noise. The spatial brightness distribution at the best arrival time pick, the temporal brightness at the best location, and the alignment of the synthetic waveforms are shown in Figure 4-12 and 4-12. The recovered location and arrival time for denoised synthetic data and noisy synthetic data are compared in Table 4.1. We found that even with 50% Gaussian noise, the SSA can detect the event well and, meanwhile, locate the event with an error less than 5 mm in each of the three space dimensions.

4.3.2 Location

Grid search

The grid search is the simplest algorithm for AE location. We first grid the cylinder space (Figure 4-14), and calculate the theoretical travel time from each grid. Then, we construct an objective function to measure the difference between the theoretical

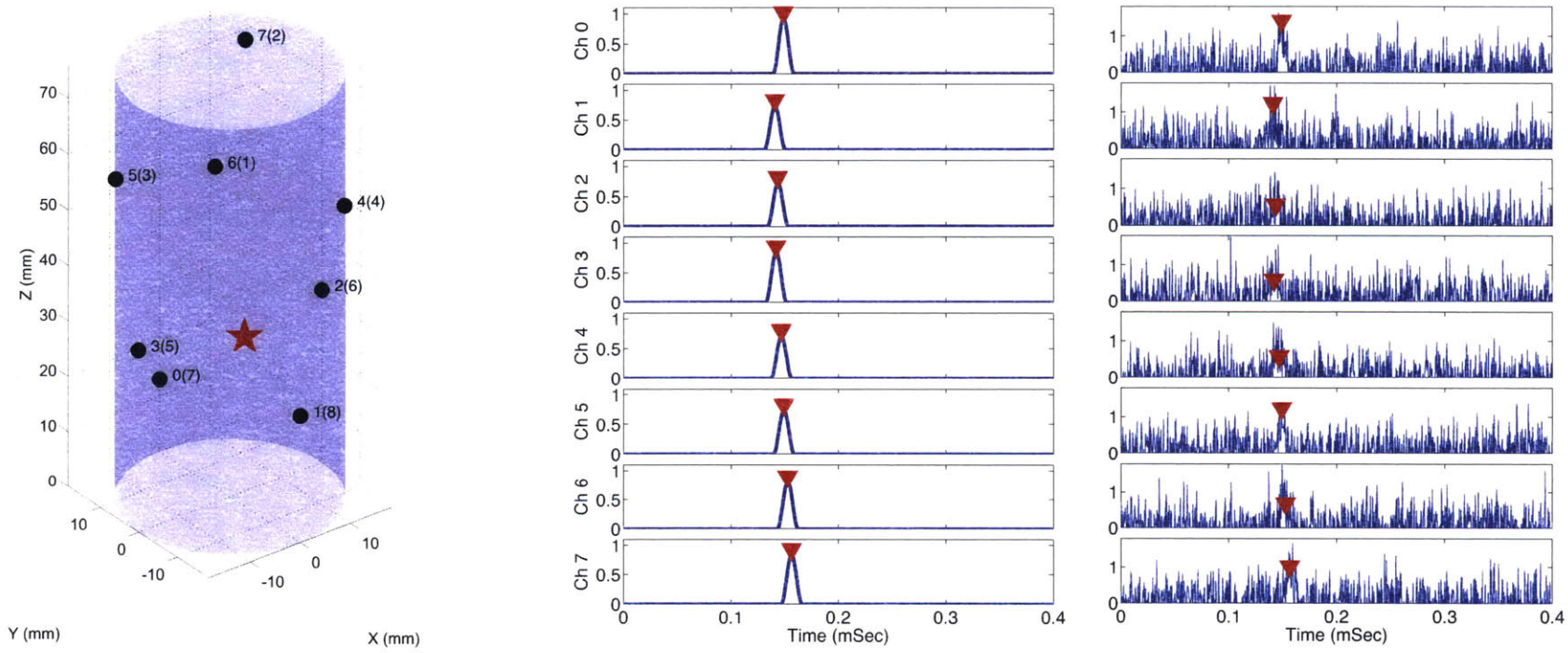

Figure 4-10: The synthetic system and AE waveforms for the SSA. Left: The cylindrical system with the synthetic event marked as a red star, and eight sensors marked as black cycles. Middle: The synthetic waveforms for the eight sensors without noise. Right: The synthetic waveforms for the eight sensors with 50% Gaussian noise.

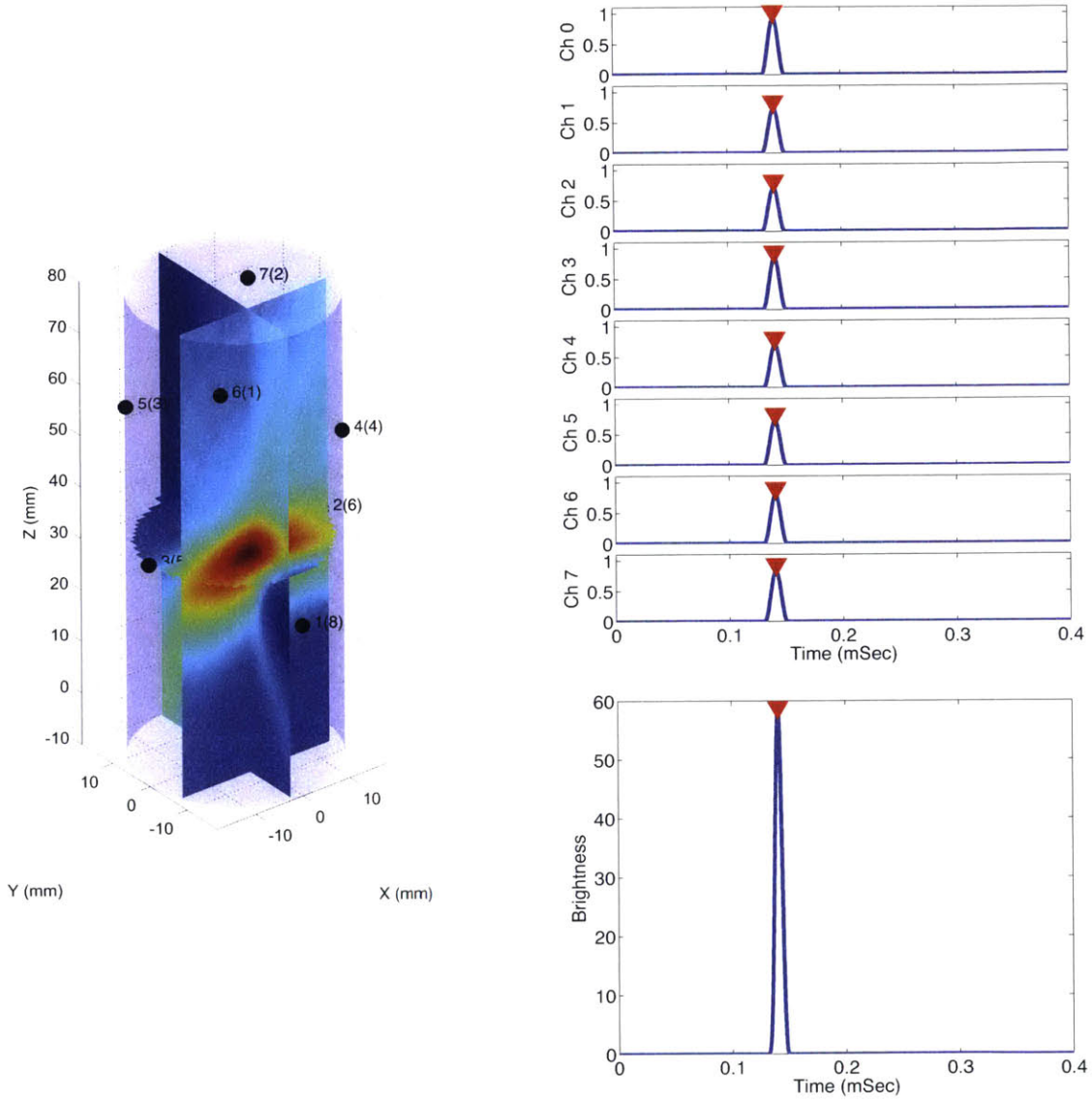

Figure 4-11: The SSA event detection and location results for the synthetic AE data without noise. Left: The 3-D view of the brightness distribution at the best picked arrival time; Right top: The alignment of the waveforms at the best location and picked arrival time; Right bottom: The brightness function at the best location. The red triangles denote the picked arrival time.

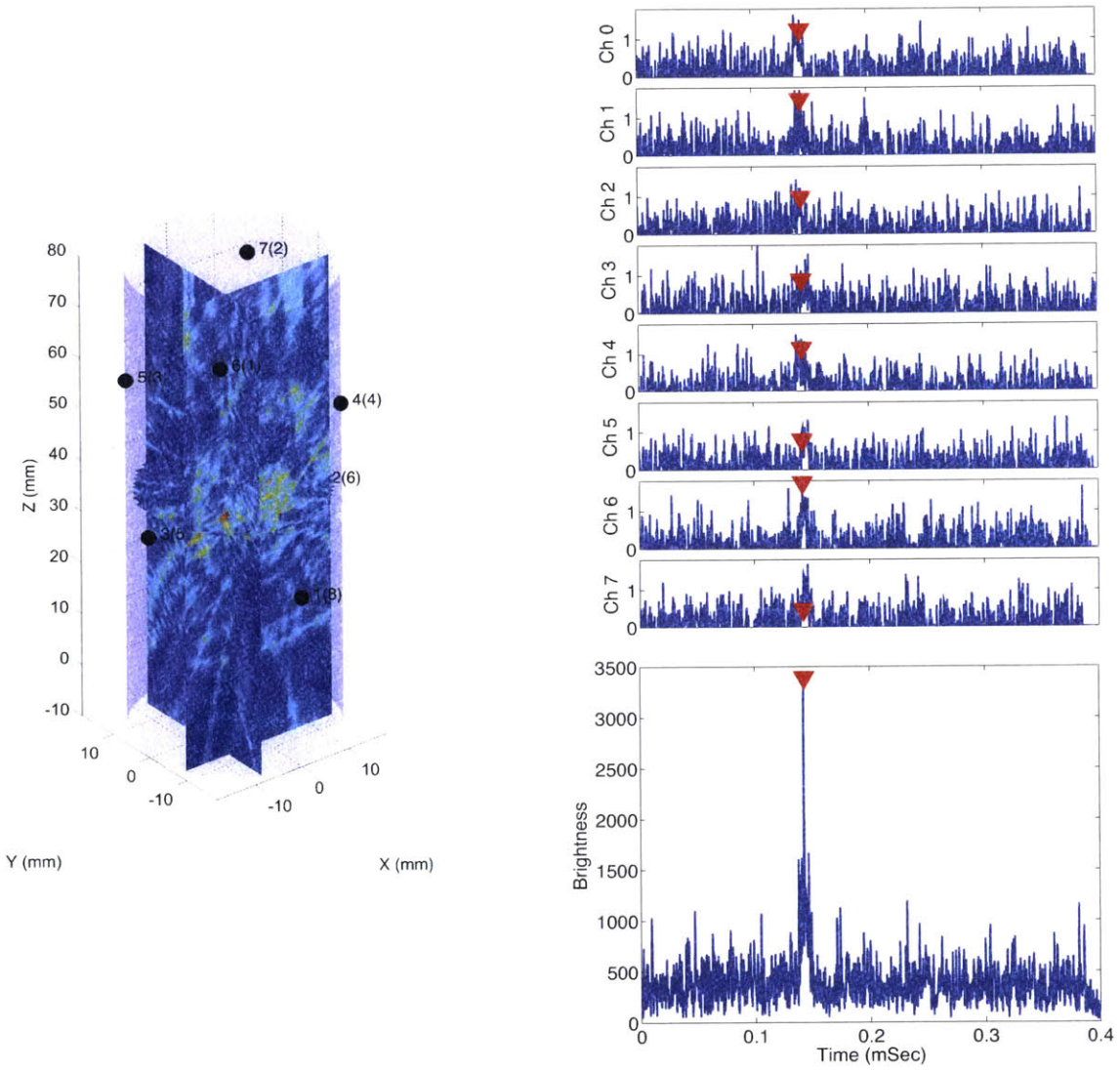

Figure 4-12: The SSA event detection and location results for the synthetic AE data with 50% Gaussian noise. Left: The 3-D view of the brightness distribution at the best picked arrival time; Right top: The alignment of the waveforms at the best location and picked arrival time; Right bottom: The brightness function at the best location. The red triangles denote the picked arrival time.

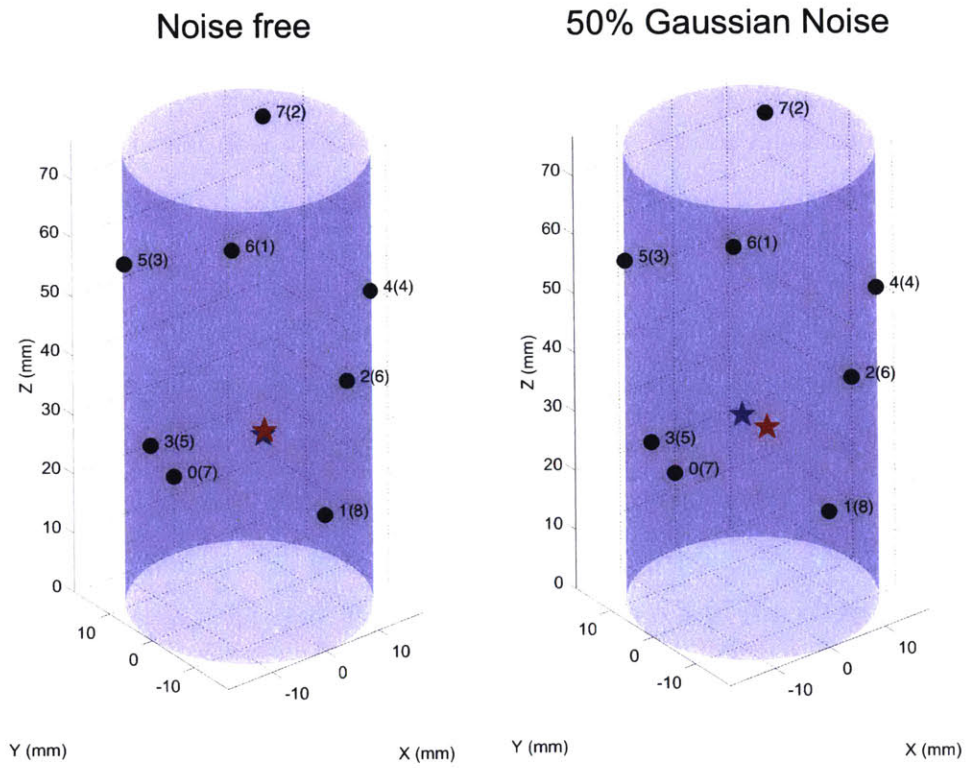

Figure 4-13: The comparison of the SSA location results for the synthetic AE data without noise (left) and with 50 % Gaussian noise (right). The red star shows the true location, and the blue star shows the recovered location.

and observed arrival time of one phase

$$\arg\min f(x_i, y_i, z_i, \tau_0) = \sum_{i=1}^{N_r} \|T_{obs}(x_r^i, y_r^i, z_r^i) - \tau_0 - T_{theo}(x_s, y_s, z_s, x_r^i, y_r^i, z_r^i)\|_2 \quad (4.6)$$

$$T_{theo}(x_s, y_s, z_s, x_r^i, y_r^i, z_r^i) = \frac{\sqrt{(x_r^i - x_s)^2 + (y_r^i - y_s)^2 + (z_r^i - z_s)^2}}{v^{ph}} \quad (4.7)$$

$f(x_s, y_s, z_s, \tau_0)$ is objective function, $T_{obs}(x_r^i, y_r^i, z_r^i)$ is observed arrival time of a phase for ith receiver, $T_{theo}(x_s, y_s, z_s, x_r^i, y_r^i, z_r^i)$ is the theoretical travel time of a phase from source to ith receiver, τ_0 is the origin time, $[x_s, y_s, z_s]$ is the source location, $[x_r^i, y_r^i, z_r^i]$ is the ith receiver location, v^{ph} is the velocity of the rock sample for one phase. The best location would be found when the objective function is minimized.

NonLinLoc

The NonLinLoc, referring to "nonlinear location", is a Bayesian-based location package (Lomax et al., 2000), which can not only locate the AE event, but also provide the uncertainties of the location. The uncertainties of the location $\boldsymbol{x}$ were presented as a posterior probability density function $P(\boldsymbol{x}|\boldsymbol{d})$, $\boldsymbol{d}$ is the arrival time data. In this chapter, we directly use the open source NonLinLoc package to study the location, as well as the uncertainties of the AE events.

SSA

The SSA location algorithm has been illustrated in the event detection part. For the implementation, we divide each AE data segment (e.g., 243) into 4070 small windows, and apply the SSA to each window assuming there is only one event in each window. In reality, some windows only contains noise and cannot contribute to map the microfractures in the specimen. The greatest differences between the window contains noise and the window contains obvious fracturing related event are that the maximum value of the brightness function. The noisy window, in general, has low maximum brightness value, and vice versa. To leave out the noise events, I set an SSA brightness threshold, and only considered the "bright" windows to the AE event

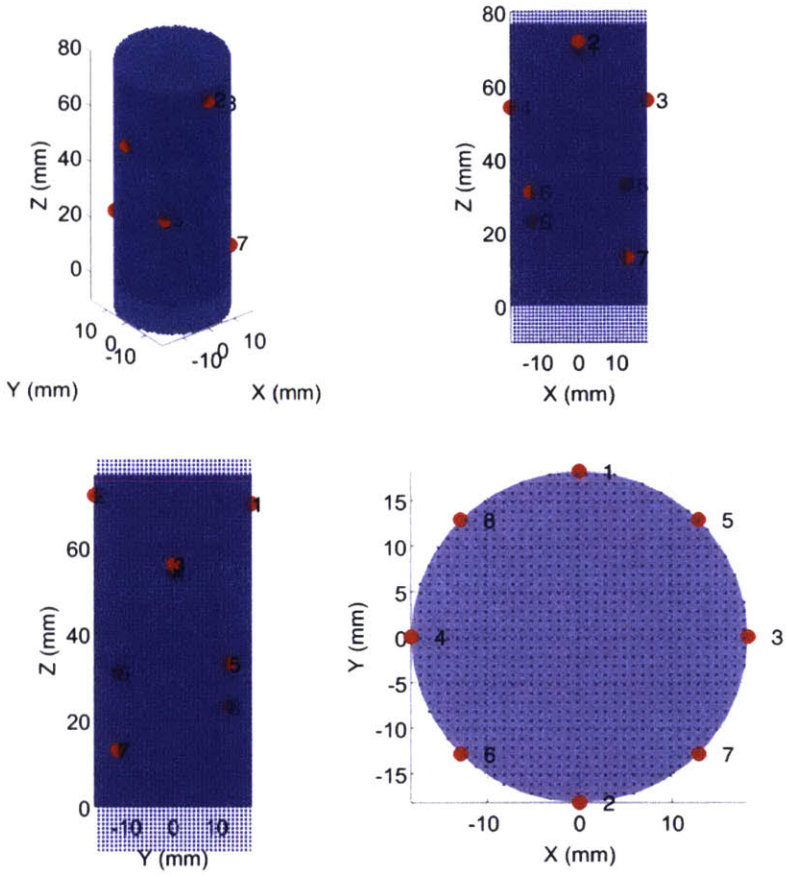

Figure 4-14: The distribution of grids in 3-D, side, and top views. The grid space is 1 mm.

count.

4.3.3 Full moment tensor inversion (FMTI)

Here I applied the full moment tensor inversion (FMTI) method to the equation used in Chapter 2, I first obtain the marginal posterior probability distribution $P(\boldsymbol{x}^*|\boldsymbol{d})$ for any given $\boldsymbol{x}^*$

$$\begin{aligned}
P(\boldsymbol{d}|\boldsymbol{x}^*) &= \frac{1}{\sqrt{(2\pi)^N \det \boldsymbol{\Sigma_e}}} \int_{-\infty}^{\infty} \exp\left[-\frac{1}{2}\left(\boldsymbol{d}-\boldsymbol{G}(\boldsymbol{x})\boldsymbol{m}\right)^T \boldsymbol{\Sigma_e}^{-1}\left(\boldsymbol{d}-\boldsymbol{G}(\boldsymbol{x})\boldsymbol{m}\right)\right] d^6\boldsymbol{m} \\
&= \frac{\exp\left[-\frac{1}{2}\sum_{i=1}^{N}\left(\boldsymbol{\Sigma_e}^{-1}\right)_{ii} d_i^2\right]}{\sqrt{(2\pi)^N \det \boldsymbol{\Sigma_e}}} \int_{-\infty}^{\infty} \exp\left[-\frac{1}{2}\sum_{j,k=1}^{6} A_{j,k} m_j m_k + \sum_{j=1}^{6} B_j m_j\right] d^6\boldsymbol{m} \\
&= \frac{\exp\left[-\frac{1}{2}\sum_{i=1}^{N}\left(\boldsymbol{\Sigma_e}^{-1}\right)_{ii} d_i^2\right]}{\sqrt{(2\pi)^N \det \boldsymbol{\Sigma_e}}} \sqrt{\frac{(2\pi)^N}{\det \boldsymbol{A}}} e^{\frac{1}{2}\boldsymbol{B}^T \boldsymbol{A}^{-1} \boldsymbol{B}} \\
&= \frac{\exp\left[-\frac{1}{2}\sum_{i=1}^{N}\left(\boldsymbol{\Sigma_e}^{-1}\right)_{ii} d_i^2\right]}{\sqrt{\det \boldsymbol{\Sigma_e} \det \boldsymbol{A}}} e^{\frac{1}{2}\boldsymbol{B}^T \boldsymbol{A}^{-1} \boldsymbol{B}},
\end{aligned} \tag{4.8}$$

where

$$\boldsymbol{A} = \sum_{i=1}^{N}\left(\boldsymbol{\Sigma_e}^{-1}\right)_{ii} \begin{bmatrix}
G_{i1}^2 & G_{i1}G_{i2} & G_{i1}G_{i3} & G_{i1}G_{i4} & G_{i1}G_{i5} & G_{i1}G_{i6} \\
G_{i2}G_{i1} & G_{i2}^2 & G_{i2}G_{i3} & G_{i2}G_{i4} & G_{i2}G_{i5} & G_{i2}G_{i6} \\
G_{i3}G_{i1} & G_{i3}G_{i2} & G_{i3}^2 & G_{i1}G_{i4} & G_{i1}G_{i5} & G_{i3}G_{i6} \\
G_{i4}G_{i1} & G_{i4}G_{i2} & G_{i4}G_{i3} & G_{i4}^2 & G_{i1}G_{i5} & G_{i4}G_{i6} \\
G_{i5}G_{i1} & G_{i5}G_{i2} & G_{i5}G_{i3} & G_{i5}G_{i4} & G_{i5}^2 & G_{i5}G_{i6} \\
G_{i6}G_{i1} & G_{i6}G_{i2} & G_{i6}G_{i3} & G_{i6}G_{i4} & G_{i6}G_{i5} & G_{i6}^2
\end{bmatrix}, \tag{4.9}$$

Table 4.2: Simplified Green's functions for six moment element

	Simplified Green's function
G_{i1}	$\frac{1}{4\pi\rho v_p^3 r_i}\sin^2\theta_i\cos^2\phi_i$
G_{i2}	$\frac{1}{4\pi\rho v_p^3 r_i}\sin^2\theta_i\sin^2\phi_i$
G_{i3}	$\frac{1}{4\pi\rho v_p^3 r_i}\cos^2\phi_i$
G_{i4}	$\frac{1}{4\pi\rho v_p^3 r_i}\sin^2\theta_i\cos 2\phi_i$
G_{i5}	$\frac{1}{4\pi\rho v_p^3 r_i}\sin 2\theta_i\sin\phi_i$
G_{i6}	$\frac{1}{4\pi\rho v_p^3 r_i}\sin 2\theta_i\cos\phi_i$

and

$$\boldsymbol{B} = \sum_{i=1}^{N} \left(\boldsymbol{\Sigma}_{\boldsymbol{e}}^{-1}\right)_{ii} d_i \begin{bmatrix} G_{i1} \\ G_{i2} \\ G_{i3} \\ G_{i4} \\ G_{i5} \\ G_{i6} \end{bmatrix}. \tag{4.10}$$

The posterior distribution of $\boldsymbol{m}$ given $\boldsymbol{d}$ can be extracted as

$$P(\boldsymbol{m}|\boldsymbol{d}) = \int P(\boldsymbol{m}|\boldsymbol{x}^*, \boldsymbol{d}) P(\boldsymbol{x}^*|\boldsymbol{d}) d\boldsymbol{x}^*. \tag{4.11}$$

P-amplitude based FMTI

The P-amplitude based moment tensor inversion (FMTI) uses simplified Green's function to generate the forward Green's functions of each moment elements (Table 4.2). This simplification assumes a homogenous and isotropic media in the space where the elastic waves propagate. The data for the inversion are the amplitude of the P waves.

Waveform based FMTI

If we assume the instrument response for all the sensors is the same at the frequency domain in which we are interested, and we can directly apply the waveform-based Bayesian moment tensor inversion method to the AE waveforms as illustrated in Chapter 2.

4.4 Results

We first apply the three event detection methods, and the three location methods to the two example waveform segments (Figure 4-6). The comparison of the counts of the detected events for the period of strong AE event occurrence is shown in Figure 4-15. We also applied the grid search location algorithm to the automatic picked first-P arrival time from the STA/LTA and AIC algorithms to obtain the initial location of the AE events. For the SSA method, we divided each segment into 4070 windows, and apply the SSA for each small window by assuming each window only contained one event. However, since some windows may just have noise, and the located event is not trustable. We setup a threshold to leave out the noisy windows. The event location distribution with the inference of the fault plane based on the event location are shown in Figure 4-16. The location results from SSA with the threshold of 0.1 are compared with other detection methods in Figure 4-15. We also try to present the SSA location of the segment 244 by assigning the located event more solid color when the maximum brightness value is high, while assigning the located event more transparent color when the maximum brightness value is low (Figure 4-18).

Then, we applied the location algorithm to 42 testing events using grid search and NonLinLoc method. The location results from the grid search and NonLinLoc method were shown in Figure 4-18 and 4-19. For the NonLinLoc method, leaving out those events with large uncertainties, only 32 events were located. By comparing the event location and the scanned fault plane geometry, we can see that the location results map the fracture well.

After testing all the algorithm using a sub data set, we then go through the whole 420 sec AE data. For the event detection, to combine the strength of different methods, we used the STA/LTA to do the first-round scanning of the whole real-time AE data, and extracted single events from the AE recording. After that, for each single-event window, we apply the AIC, and SSA detection/location to that window. This strategy combine the efficiency of STA/LTA, and the accuracy of the AIC-picker. In addition, the SSA provided the initial location guess, and help to infer the fracture

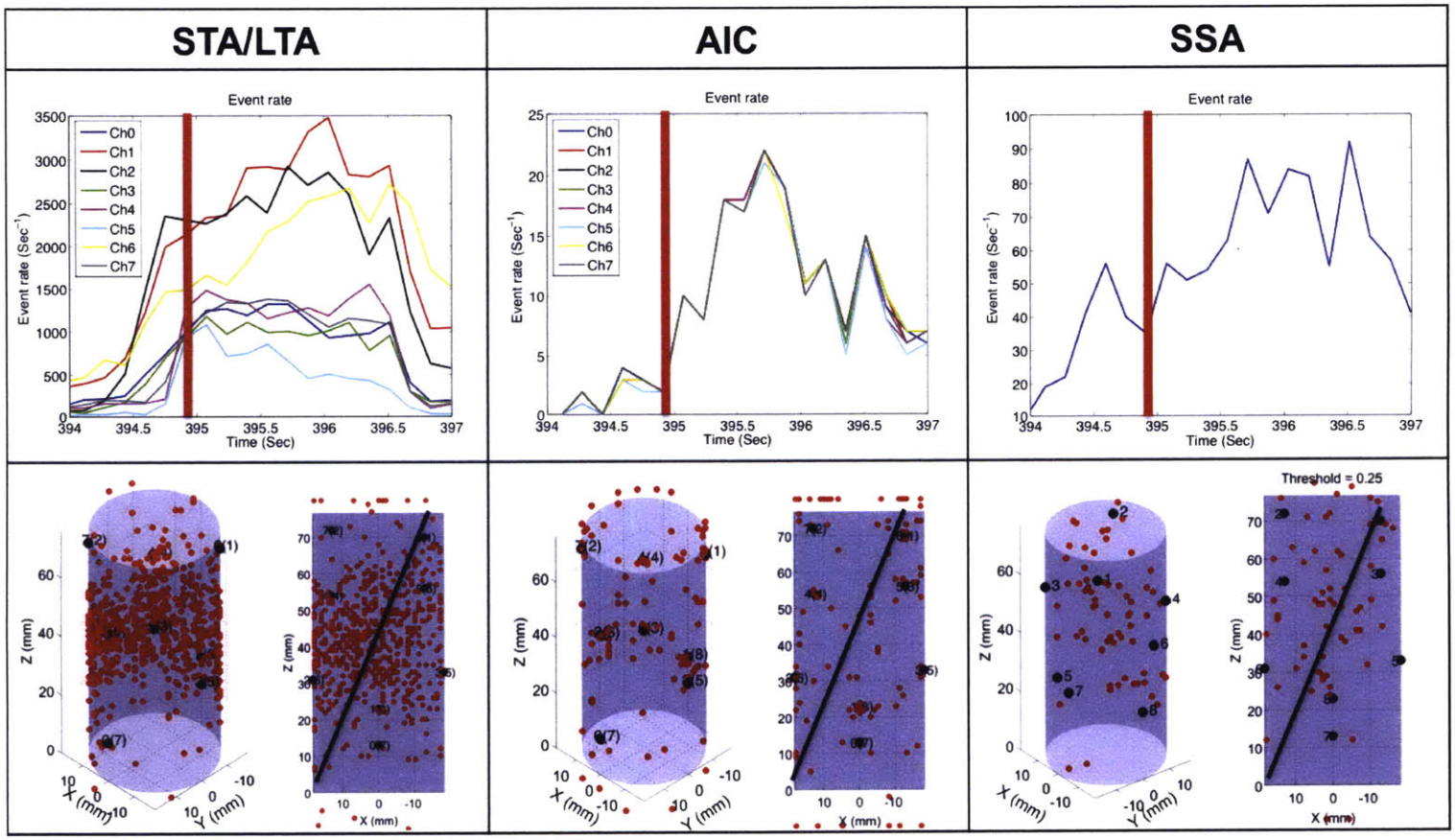

Figure 4-15: The event detection results for AE data in Figure 4-6 using the three detection method. The first row of the table shows the AE rates and accumulated event counts. The second row shows the location results using the automatic picked arrival time.

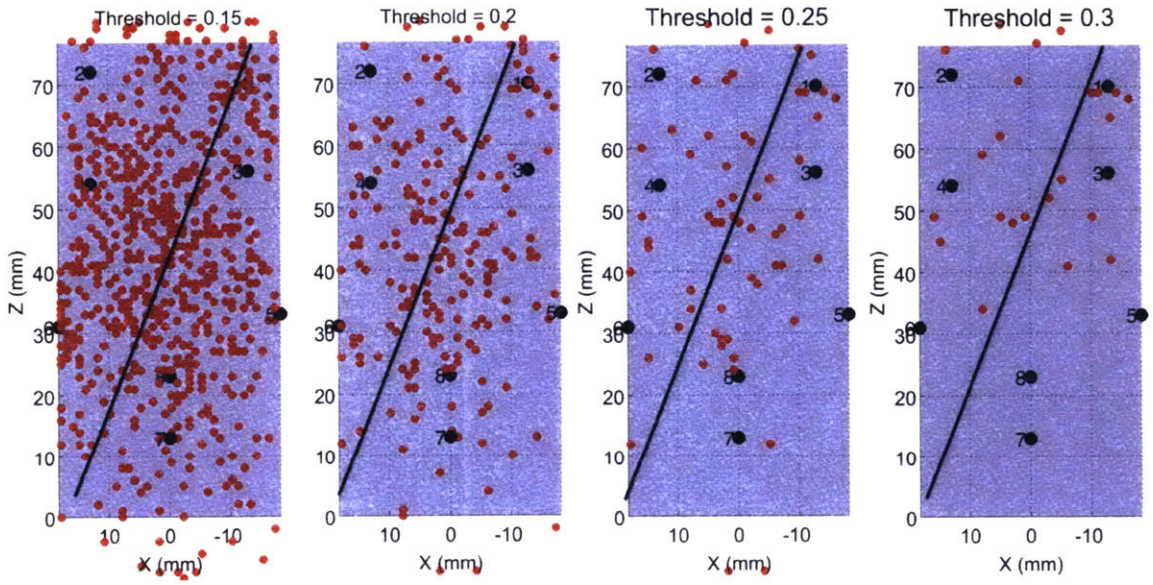

Figure 4-16: The SSA location results in the side view with different thresholds. The black line shows the best alignment direction of the located events.

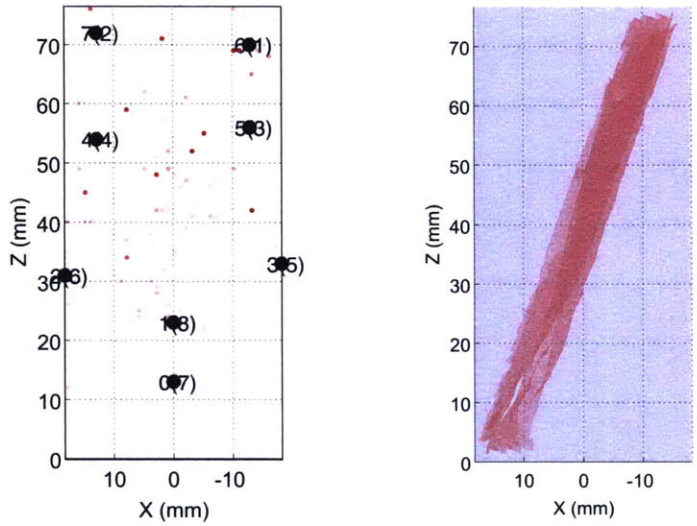

Figure 4-17: The SSA location results for the 4070 windows of the example waveform segment 244. The red circles show the event location. The maximum brightness values are presented as the transparency of the circles. The larger the brightness, the less transparency the dots are shown. The scanned fault plane topography from both the fracture topography of the top and bottom part is shown on the right.

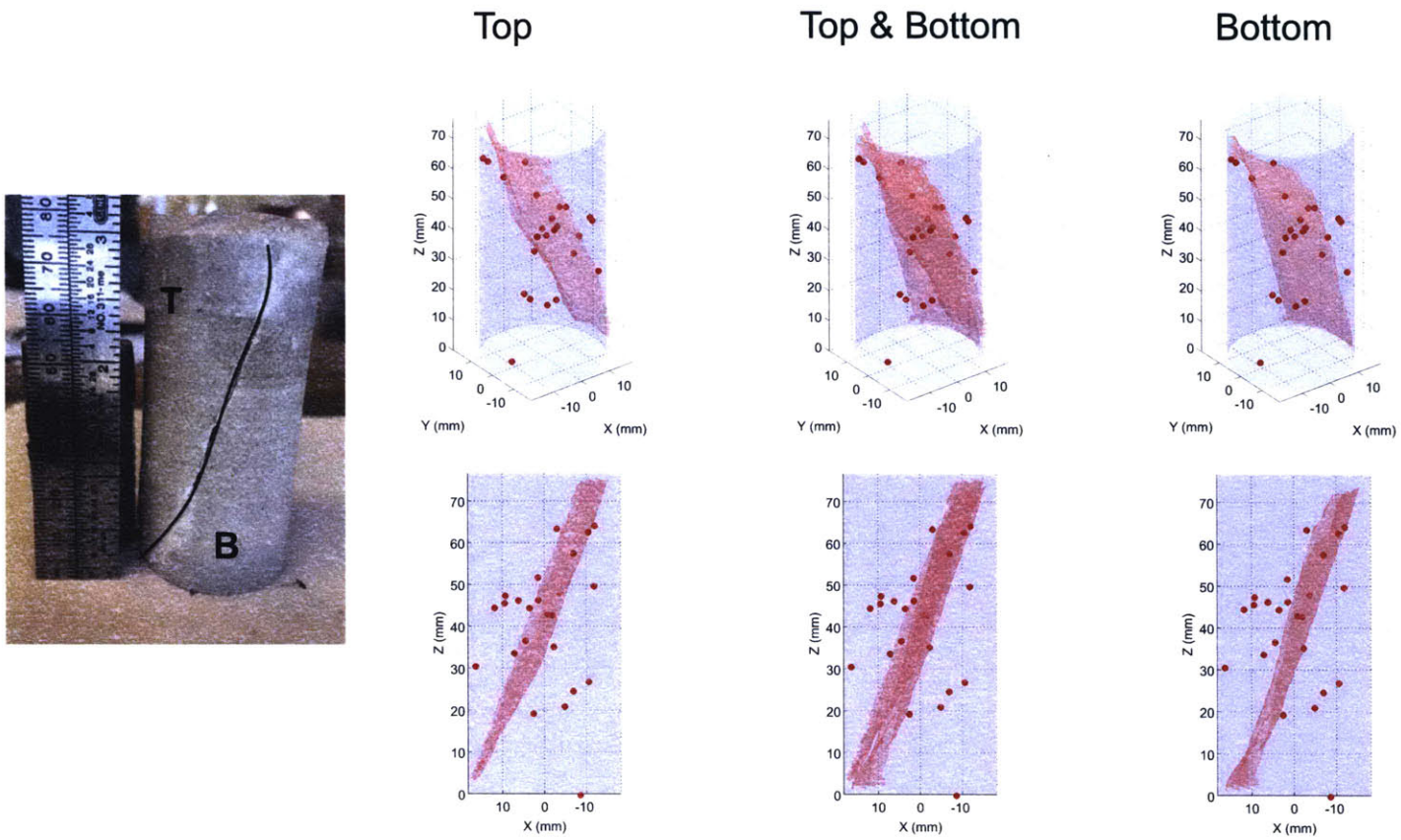

Figure 4-18: The location results of 42 events with good waveforms using the grid search method. The red circles show the event location. The scanned fault plane topography from the top and bottom part of fractured sample, plotted as transparent planes, are shown with the event location. The two planes are not fully matched because of the complexity of the fracture geometry. "Top" means that only the fracture topography of the top part is shown, "Bottom" means that only the fracture topography of the bottom part is shown, and "Top & Bottom" means that both the fracture topography of the top and bottom part is shown.

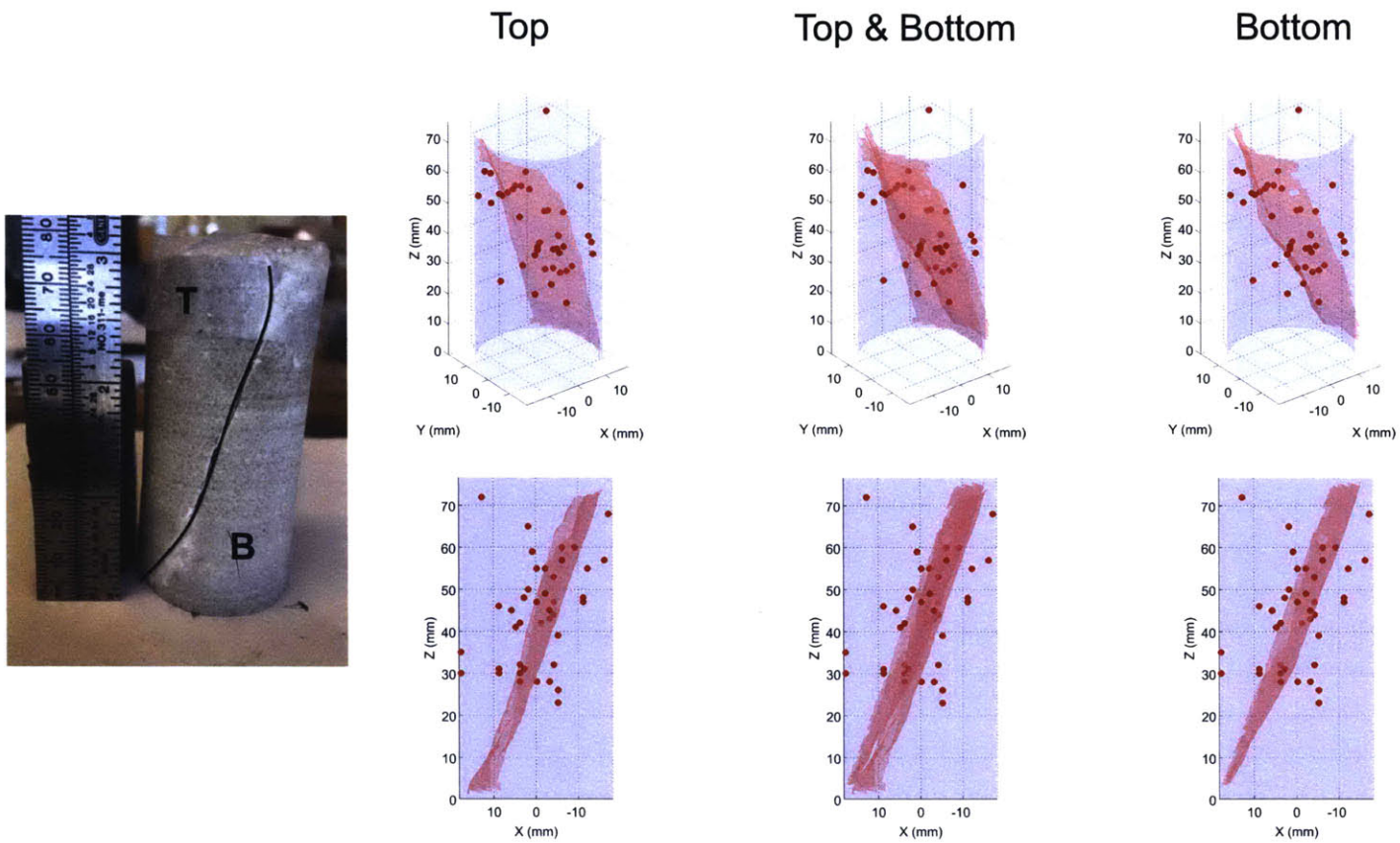

Figure 4-19: The location results of 32 events with good waveforms using the NonLinLoc method. The red circles show the event location. The scanned fault plane topography from the top and bottom part of fractured sample, plotted as transparent planes, are shown with the event location. The two planes are not fully matched because of the complexity of the fracture geometry. "Top" means that only the fracture topography of the top part is shown, "Bottom" means that only the fracture topography of the bottom part is shown, and "Top & Bottom" means that both the fracture topography of the top and bottom part is shown.

geometry.

The event rate and accumulated event count from the STA/LTA detection for the raw data and the raw data bandpass filtered by 10kHz to 500 kHz are shown in Figure 4-20 and 4-22. The trend of the event rate as a function of time are generally similar, however, since the algorithm detected more events for the filtered data before the main fracture happened, the accumulated event number for the filtered data did not show a huge increase as it is shown for the unfiltered data. We plotted the detected P-arrivals of the eight channels for each detected events and mark the events with at least four P-arrival picks with a black lines (Figure 4-21 and 4-24).

In this Chapter, to better quality control the detection, we focused on the 5837 events detected by the STA/LTA method using the unfiltered raw data. The automatic picked first-P arrivals for a common event (Event 2137) from the STA/LTA, AIC, and SSA were shown in Figure 4-21, Figure 4-24, and Figure 4-25. Visually checking the quality of the picking, the AIC method provided the most accurate picking comparing to STA/LTA and SSA (e.g., Event 2137). The SSA, although do not picked the phase arrival accurately, provided the initial guess of the location and could delineate the rough fracture shape while finishing the event detection (Figure 4-26).

To quality control the AIC-picker, I manually picked the P arrivals for 5738 events detected by the STA/LTA method. I showed the location results based on the P arrival times from the AIC and manual arrival picking in Figure 4-27 and 4-28), the nucleation processes of AE events are generally similar, which shows the accuracy of the AIC picking. I divided the fracturing processes into three parts – the pre-main-fracturing stage, main-fracturing stage, and post-main-fracturing stage. At the pre-main-fracturing stage, events occurred sparsely all over the specimen. Then, at the main-fracturing stage, the events had a rapid increase of occurrence rate and presented a trend of nucleation at the late main-fracturing stage. However, the events generally still scattered all over the specimen. This either because the microfractures were distributed all over the sample, or the large location errors of small events. Based on the test location study showing in Figure 4-18 and Figure 4-19, the large events with good waveforms correlated well with the fault plane.

After locating the AE events, I chose 12 events along the main fracture plane and applied the full moment tensor inversion to them (Figure 4-29). The moment tensor results are shown from Figure 4-30 to 4-31. The moment tensor analysis of the AE data shows a general dip-slip source mechanisms for the selected events with good waveforms along the main fracture, and a vertical maximum compressional stress. The strike of events were consistent with the fault plane geometry, which is roughly in north-south direction when the event was close to the center of the fault plane, and turned to the east-west direction when the event is close to the fault edges. However, some events indicated a horizontal maximum compressional stress, which may be because of the inhomogeneity of the specimen, or errors because the waveform amplitudes without calibration.

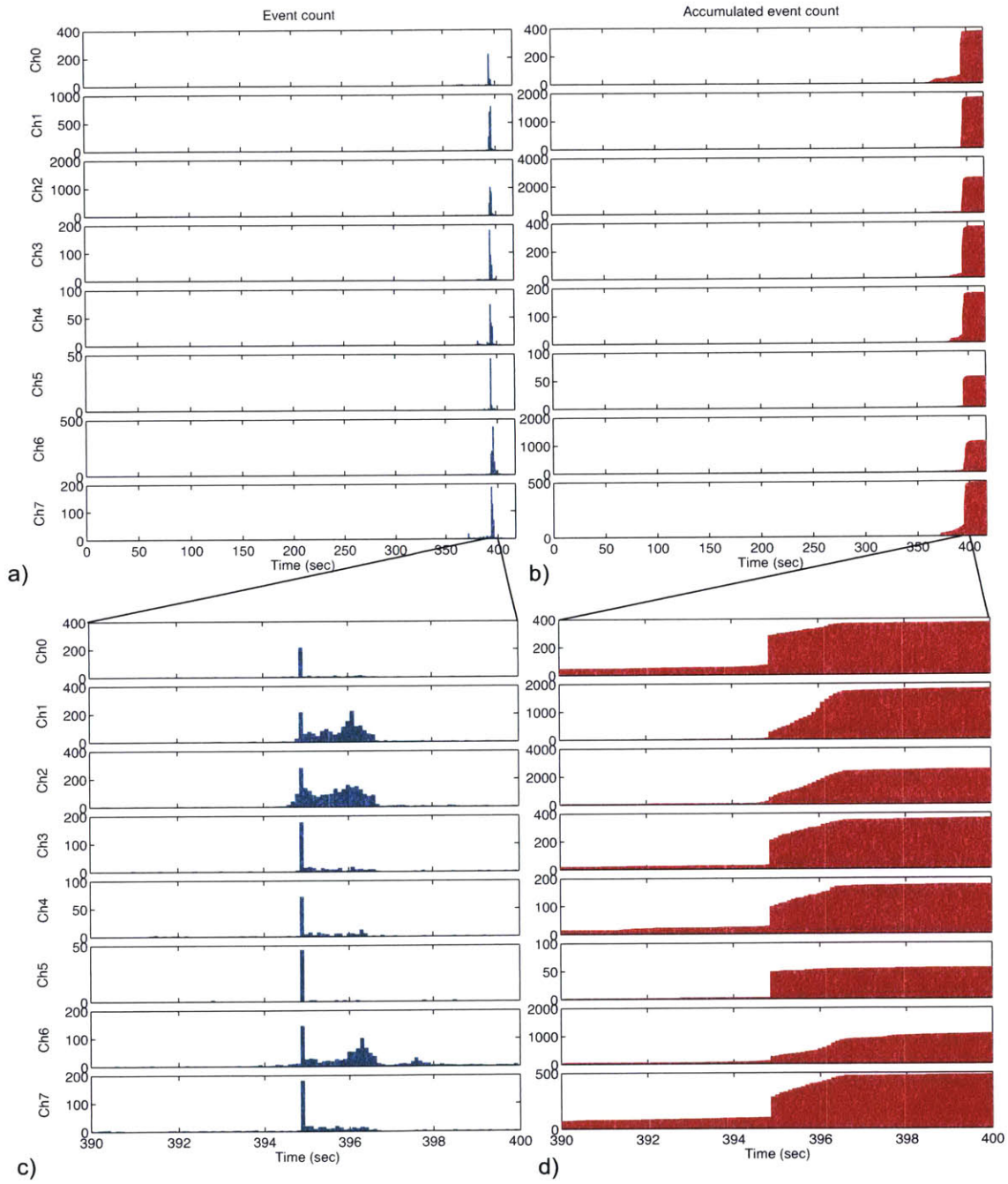

Figure 4-20: The STALTA event detection results for the unfiltered AE data. a) The event count at each second during the whole AE acquisition period; b) The accumulated event count at each second during the whole AE acquisition period; c) The zoom-in of the event count at each second during the period of high AE tensity – 390 sec to 400 sec; d) The zoom-in of the accumulated event count at each second during the period of high AE tensity – 390 sec to 400 sec.

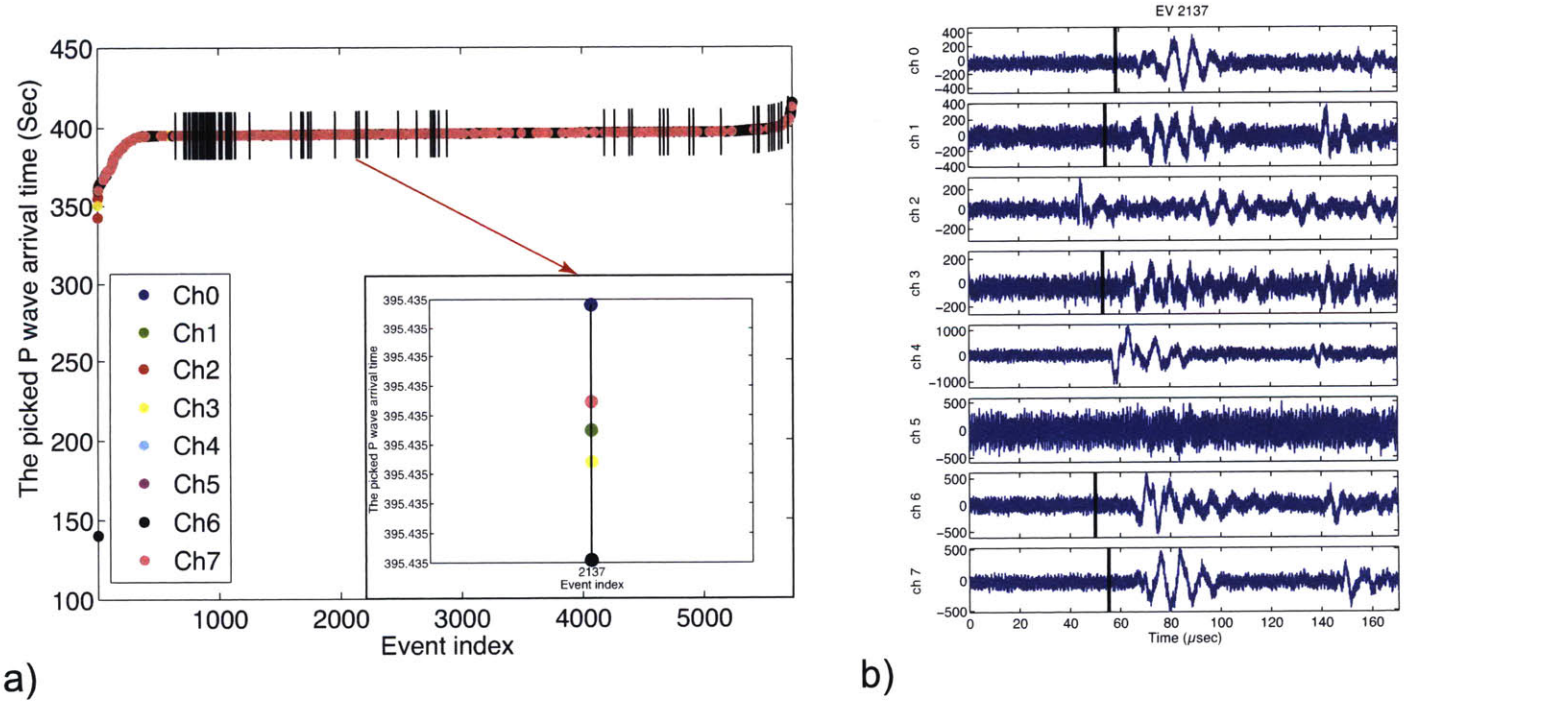

Figure 4-21: The picked P arrival time from the STALTA method for the unfiltered AE data. a) The P arrival time for the eight channels for the 5738 detected events. The black lines show the event with at least four picked P arrivals. The inset show an example of the five picked P arrival times for EV2137; b) The unfiltered waveform from Event2137. The black lines mark the picked P arrivals.

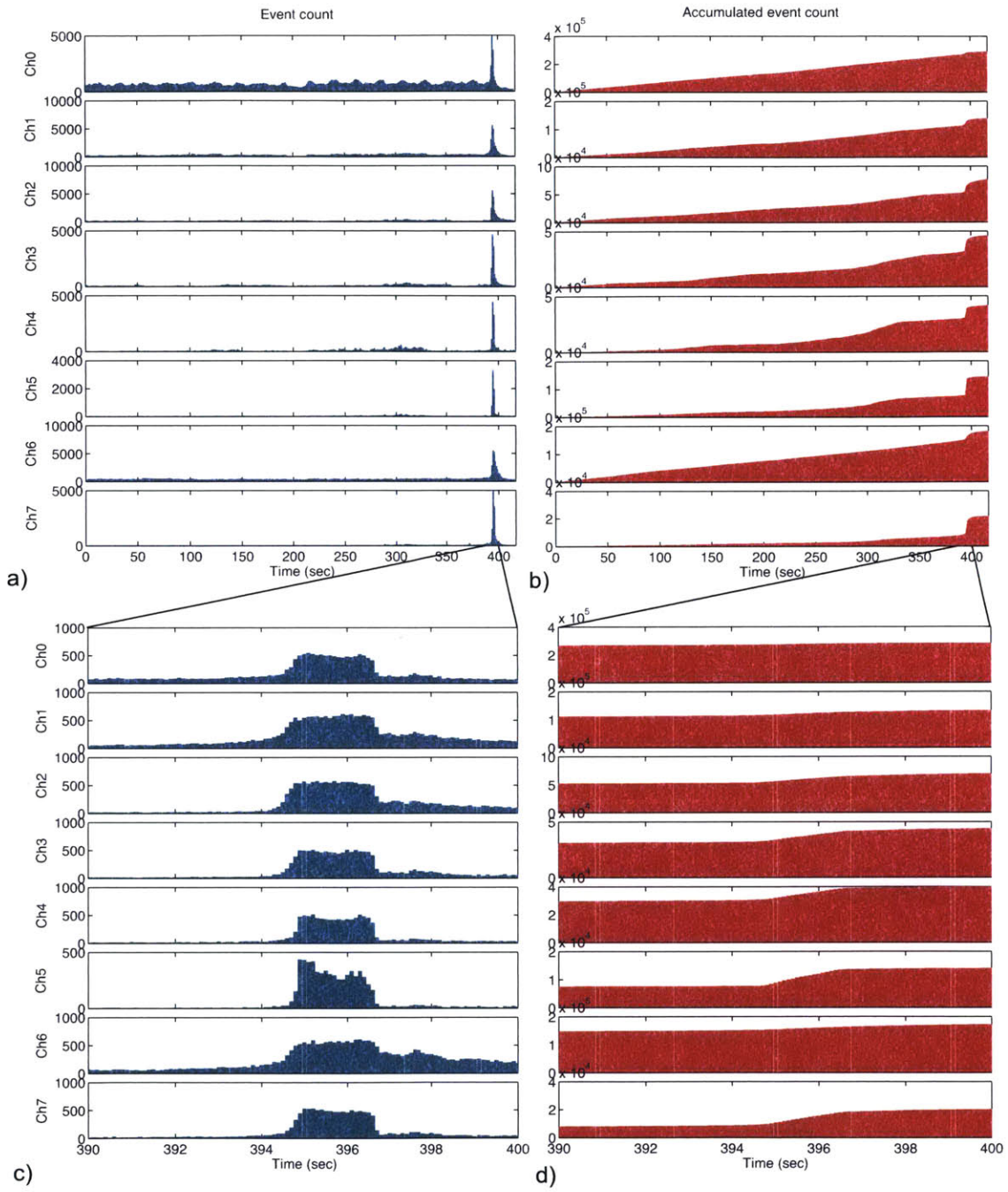

Figure 4-22: The STALTA event detection results for the AE data bandpass filtered by 10 kHz to 500 kHz. a) The event count at each second during the whole AE acquisition period; b) The accumulated event count at each second during the whole AE acquisition period; c) The zoom-in of the event count at each second during the period of high AE tensity – 390 sec to 400 sec; d) The zoom-in of the accumulated event count at each second during the period of high AE tensity – 390 sec to 400 sec.

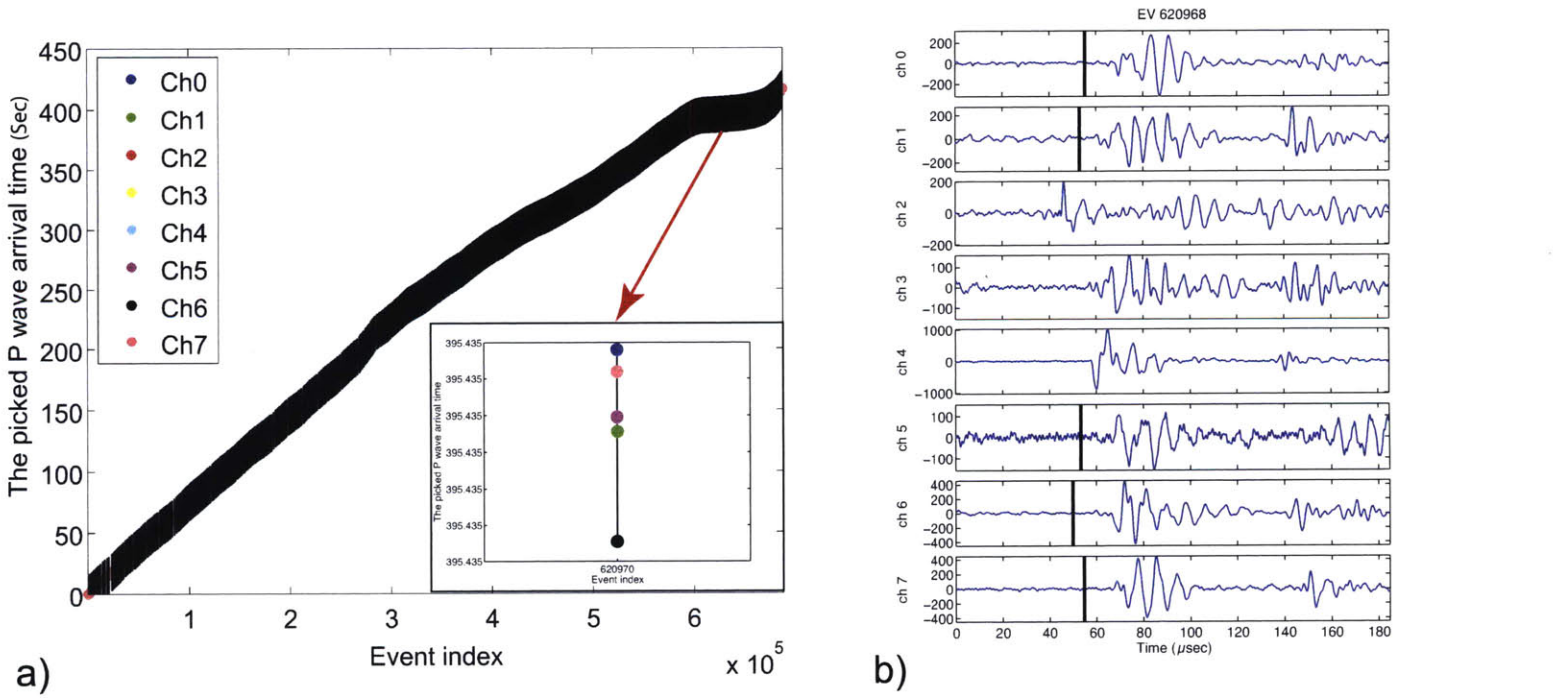

Figure 4-23: The picked P arrival time from the STA/LTA method for the AE data bandpass filtered by 10 kHz to 500 kHz. a) The P arrival time for the eight channels for the 688489 detected events. The black lines show the event with at least four picked P arrivals. The inset show an example of the five picked P arrival times for EV620968; b) The unfiltered waveform from Event 620968, which is the same event of the Event620968 in Figure **??**. The black lines mark the picked P arrivals.

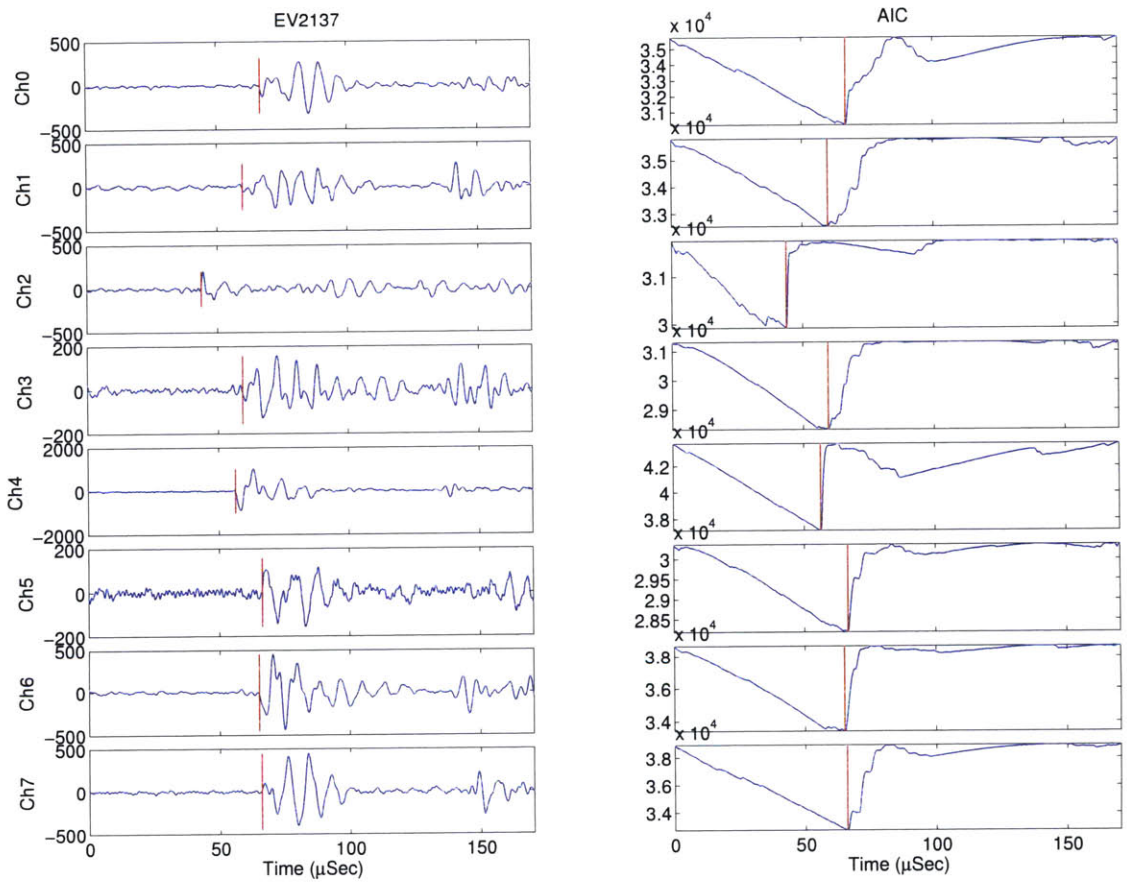

Figure 4-24: The AIC-picked P arrival time for Events2137 from the STALTA detection for the unfiltered AE data. The waveforms are bandpass filtered by 10kHz to 500kHz before applying the AIC method. Left: The P arrival time for the eight channels for the 5738 detected events. The red lines show the event picked P arrival times for EV 2137; Right: The AIC as a function of time for Event2137. The red lines mark the global minimum of the AIC function.

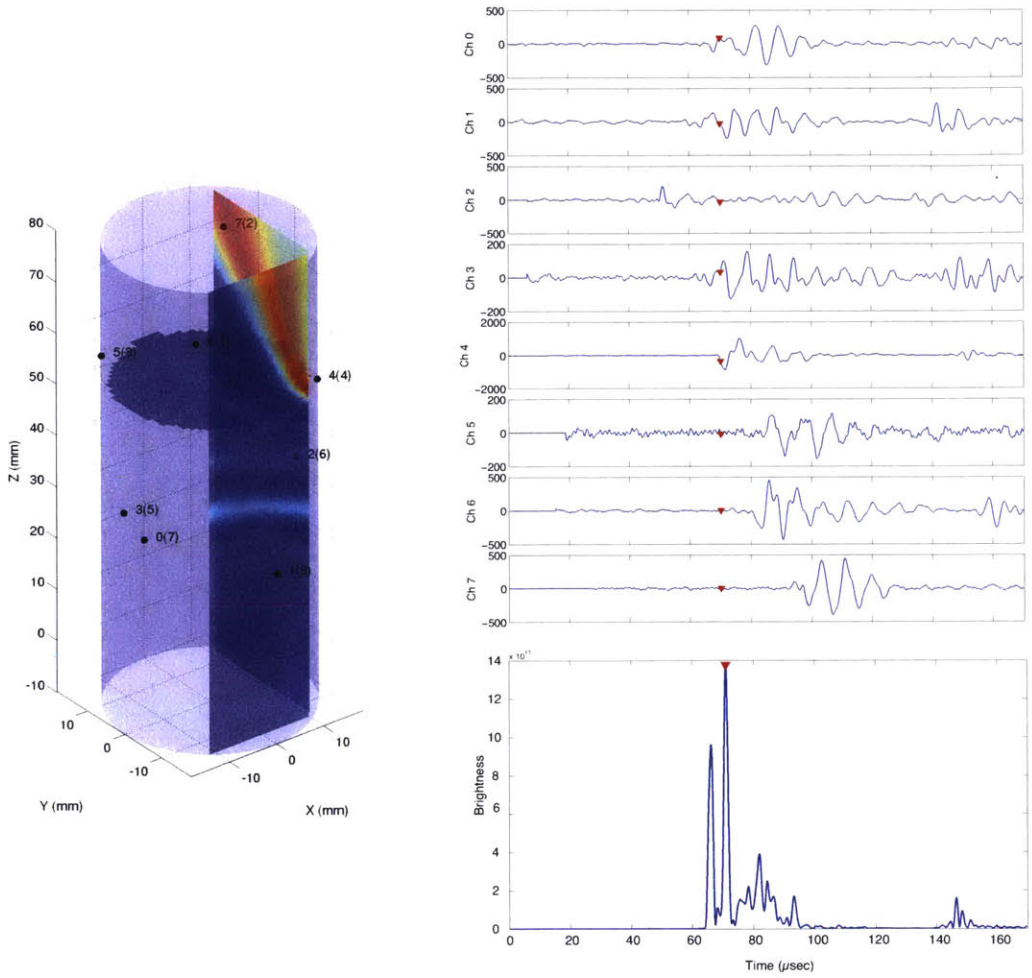

Figure 4-25: The SSA event detection and location results for the Event 2137. Left: The 3-D view of the brightness distribution at the best picked arrival time; Right top: The alignment of the waveforms at the best location and picked arrival time; Right bottom: The brightness function at the best location. The red triangles denote the picked arrival time.

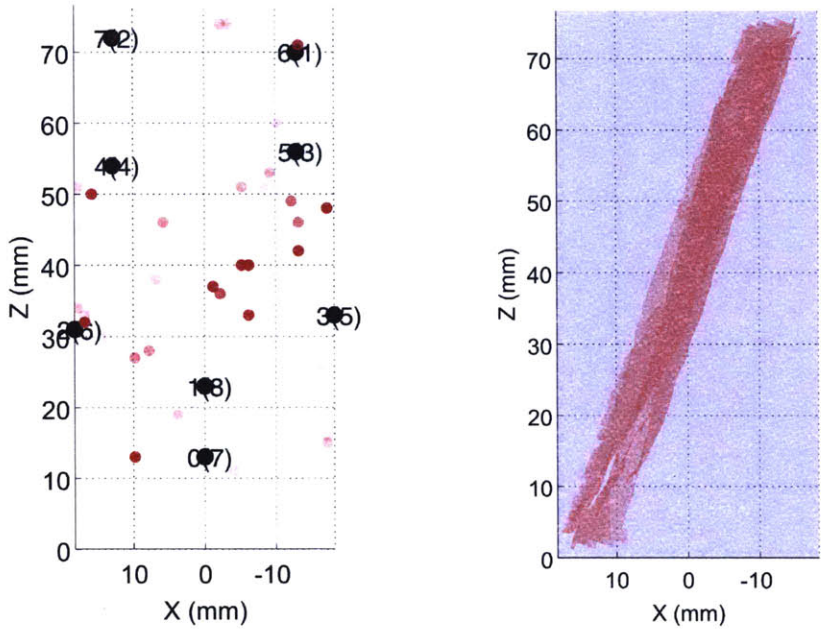

Figure 4-26: The SSA location results for the STA/LTA selected windows during the whole 420 sec. The red circles show the event location. The maximum brightness values are presented as the transparency of the circles. The larger the brightness, the less transparency the dots are shown. The scanned fault plane topography from both the fracture topography of the top and bottom part is shown on the right.

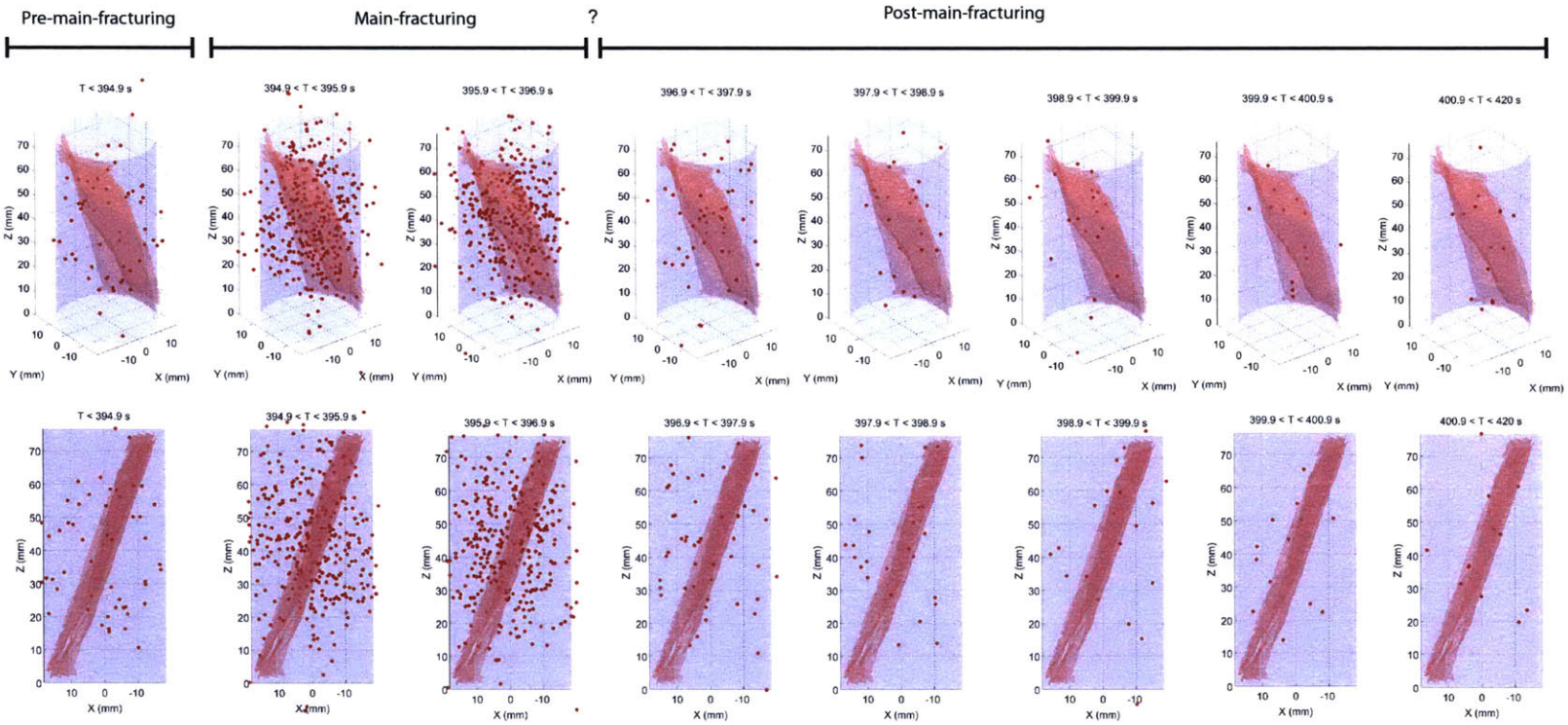

Figure 4-27: The location from the automatic AIC picking during the whole 420 sec. Top: 3-D view. Bottom: side view. The transparent red planes show the scanned fault plane geometry.

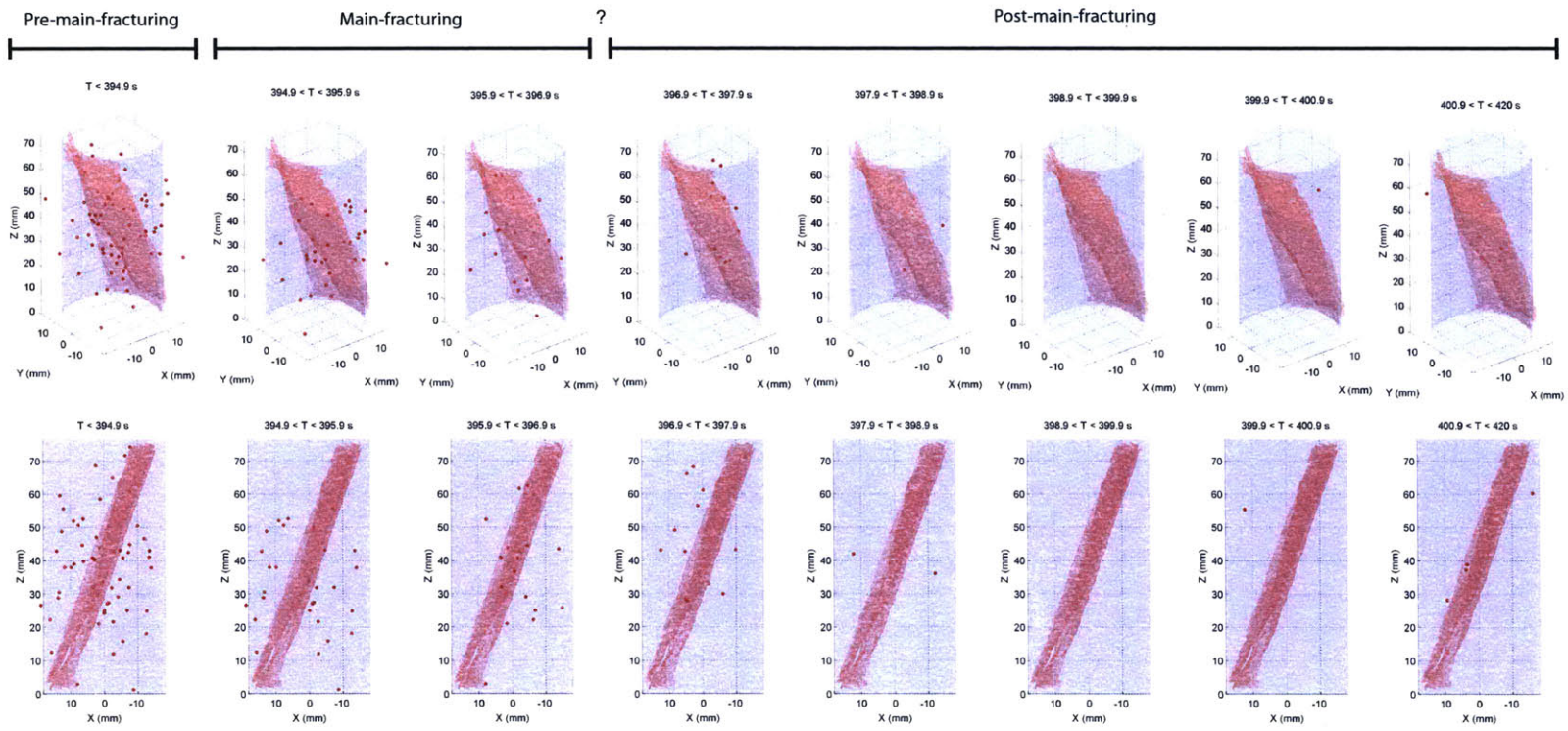

Figure 4-28: The location from the manual picking during the whole 420 sec. Top: 3-D view. Bottom: side view. The transparent red planes show the scanned fault plane geometry.

4.5 Discussion

4.5.1 Location calibration

An important question about the AE characterization is the accuracy of the event location. To address the error bound of the location, an active source location experiment was conducted for a Lucite (PMMA) specimen. The sample was machined to a cylinder with the diameter of 38.10 mm and length of 77.47 mm. Eight PZT sensors were placed over the surface of the cylinder. The distribution of the position of sensors is shown in Figure 4-42. The velocity of the P-wave was 2770 m/s, and the S-wave velocity was 1395 m/s.

We connected the triggering source to each sensor, and use other sensors as receivers. For example, if connected channel 0 to the source, then channel 2, 3, 4, 5, 6.7 were used as receivers. Channel 1 did not work since it was at the same port as channel 1. We can only connect the triggering source to the port. Thus, we had six P-wave arrivals to determine the location of the channel connected to the triggering source. The S-waves were observed, however, since the size of the sample is small, the separation of P- and S-waves was generally comparable to the dominant period for the P- and S-waves ($\sim 10\mu s$), it was hard to pick the S-wave arrivals accurately. The location error from a simple grid-search location algorithm is shown in Table 4.3 and Figure 4-43. The comparison of the observed and theoretical P-wave arrivals is shown in Figure 4-44. The maximum residuals of the P-wave arrivals is around 1 μs. The recorded waveforms the eight active source tests, as well as the theoretical P-wave travel time as a function of source-receiver distance, is presented in Figure 4-45.

The location calibration results show that the error of the source are generally in an order of mm, this could also be estimated by the maximum residual of the observed and theoretical P-wave arrival time – 1 μs. Since the P-wave velocity is around 3000 m/s, a mis-pick of 1 μs for one channel could result in a mislocation around 3 mm. If we consider the AE sampling rate of 25 MHz, 1 μs phase arrival error equals to 25 samples. For a typical period of P-wave, which is around 10 μs

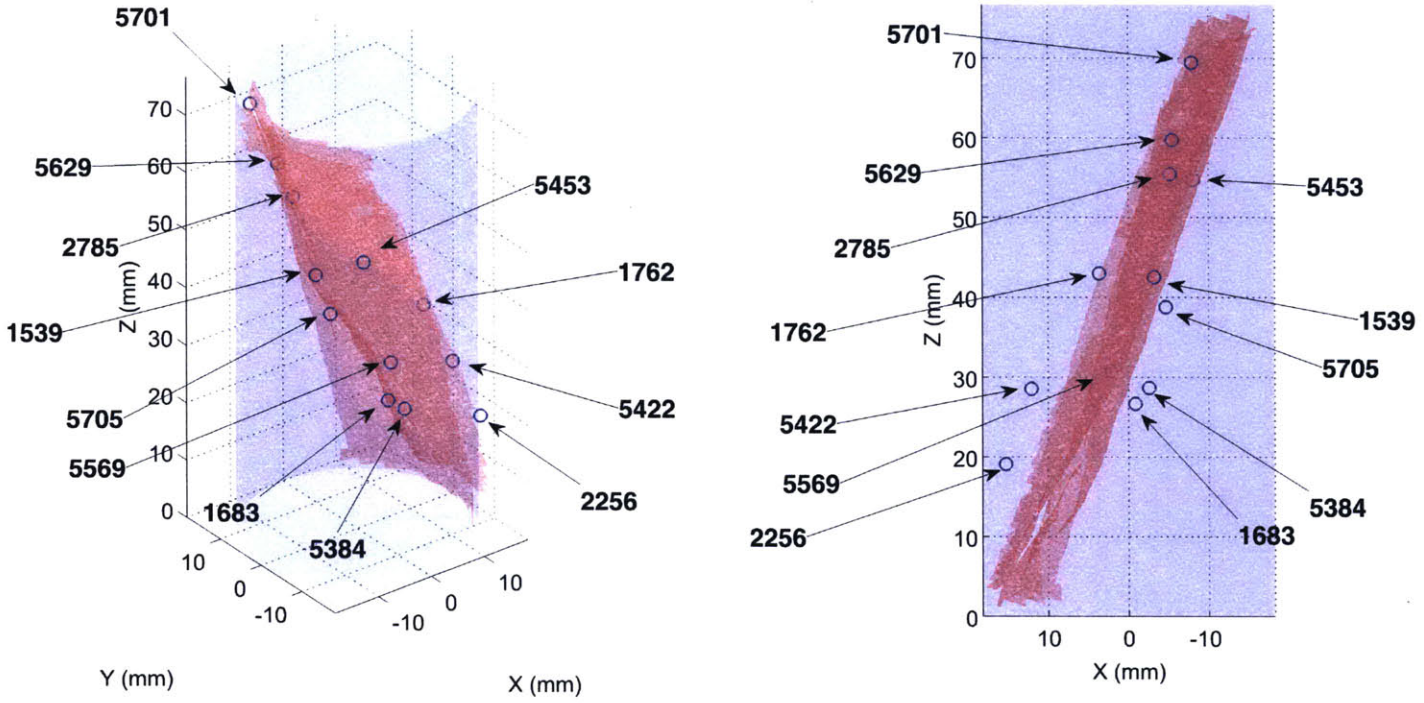

Figure 4-29: Left: Selected events for moment tensor inversion. Left: 3-D view. Right: side view.

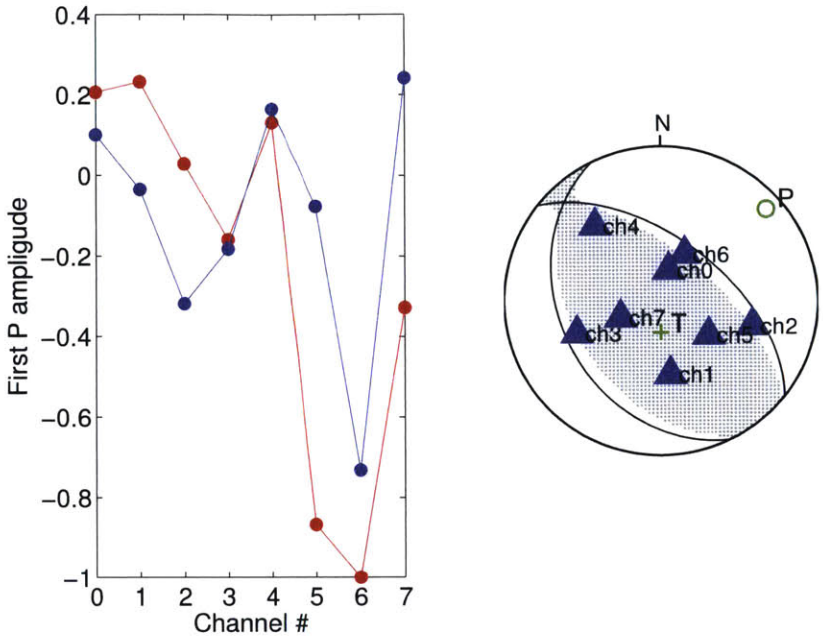

Figure 4-30: Moment tensor results for event 1539. Left: The first-P amplitude matching (Red: observed. Blue: synthetic). Right: The moment tensor solution.

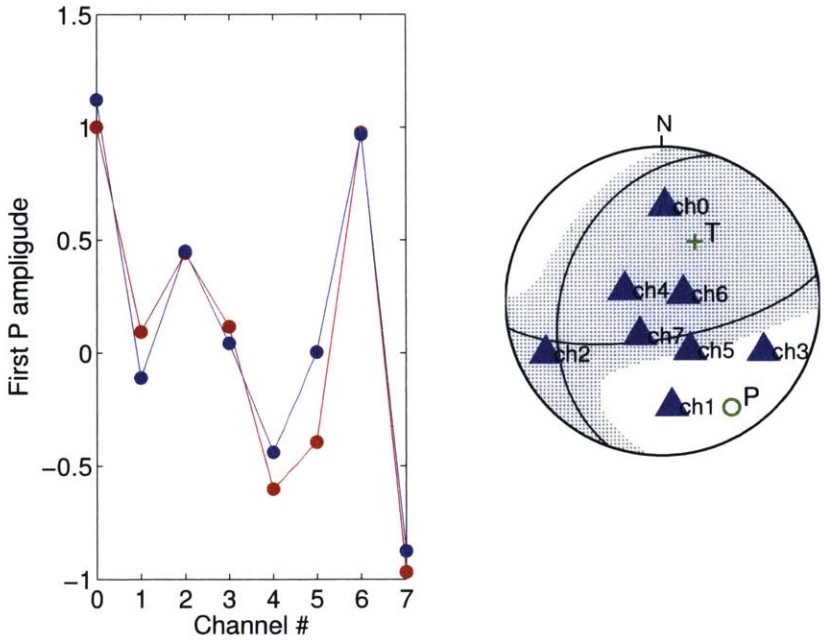

Figure 4-31: Moment tensor results for event 1683. Left: The first-P amplitude matching (Red: observed. Blue: synthetic). Right: The moment tensor solution.

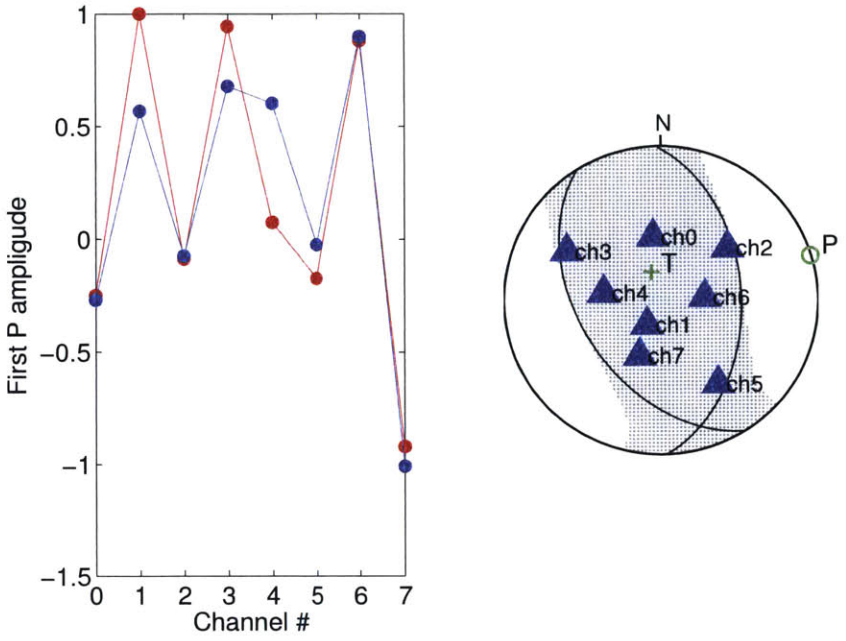

Figure 4-32: Moment tensor results for event 1762. Left: The first-P amplitude matching (Red: observed. Blue: synthetic). Right: The moment tensor solution.

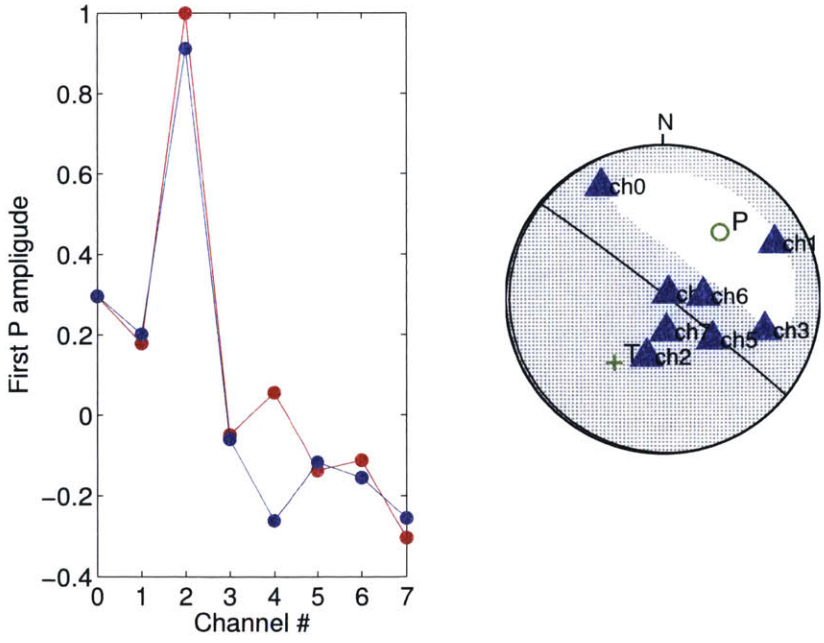

Figure 4-33: Moment tensor results for event 2256. Left: The first-P amplitude matching (Red: observed. Blue: synthetic). Right: The moment tensor solution.

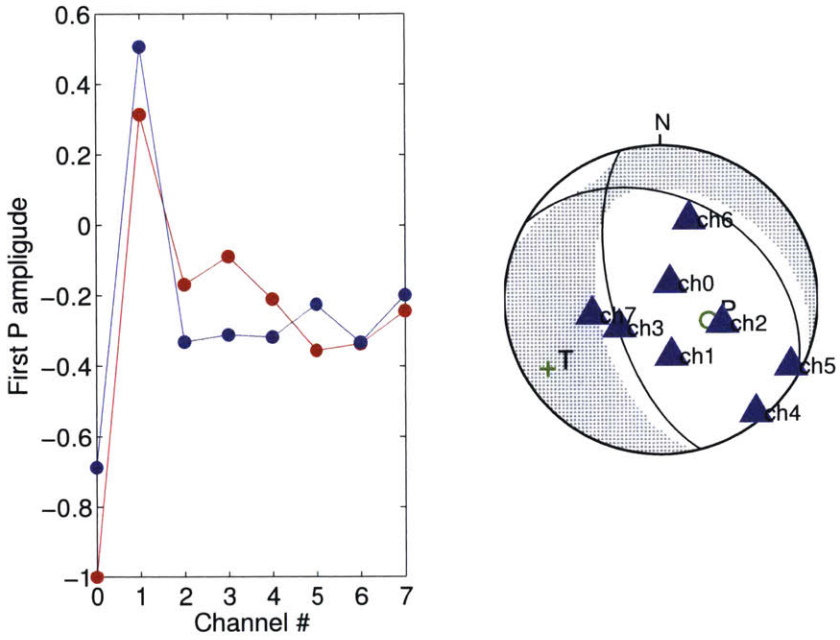

Figure 4-34: Moment tensor results for event 2785. Left: The first-P amplitude matching (Red: observed. Blue: synthetic). Right: The moment tensor solution.

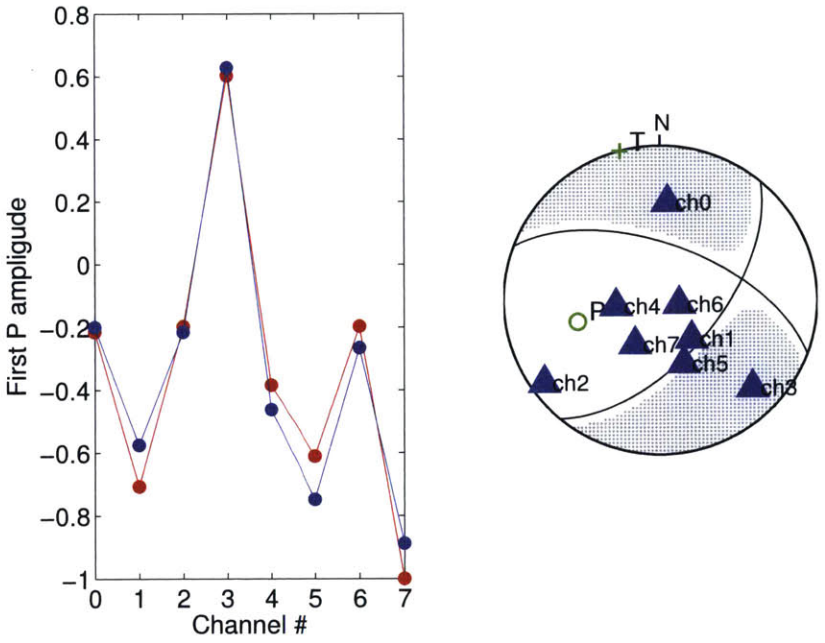

Figure 4-35: Moment tensor results for event 5384. Left: The first-P amplitude matching (Red: observed. Blue: synthetic). Right: The moment tensor solution.

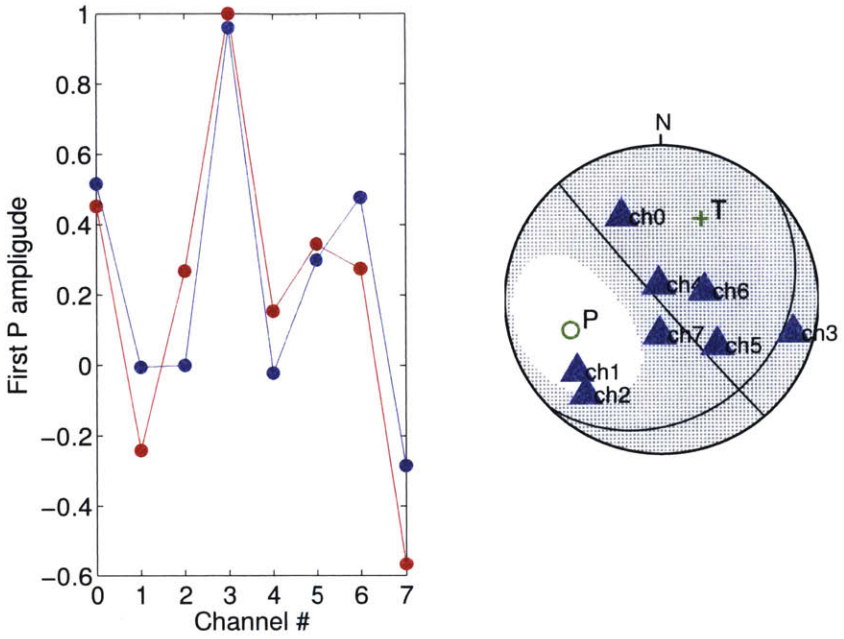

Figure 4-36: Moment tensor results for event 5422. Left: The first-P amplitude matching (Red: observed. Blue: synthetic). Right: The moment tensor solution.

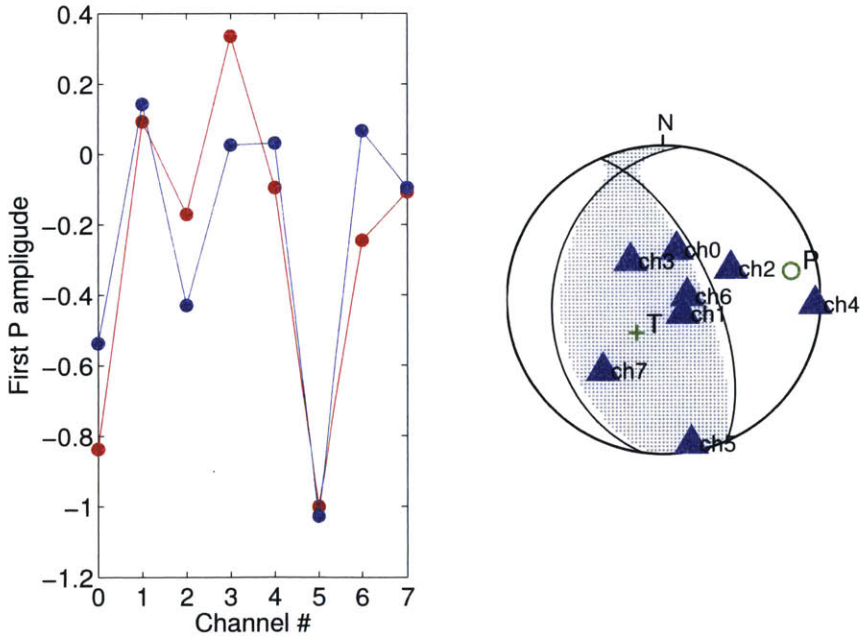

Figure 4-37: Moment tensor results for event 5453. Left: The first-P amplitude matching (Red: observed. Blue: synthetic). Right: The moment tensor solution.

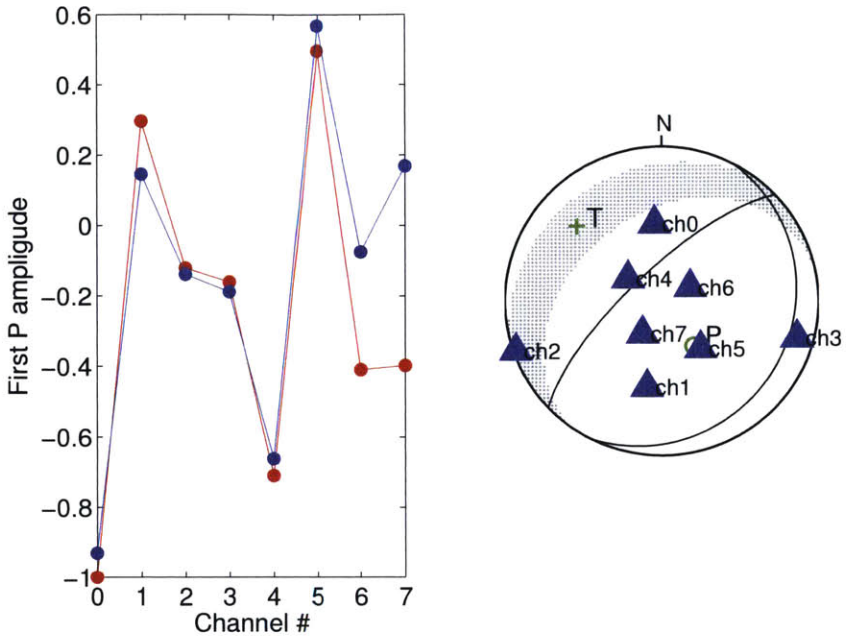

Figure 4-38: Moment tensor results for event 5569. Left: The first-P amplitude matching (Red: observed. Blue: synthetic). Right: The moment tensor solution.

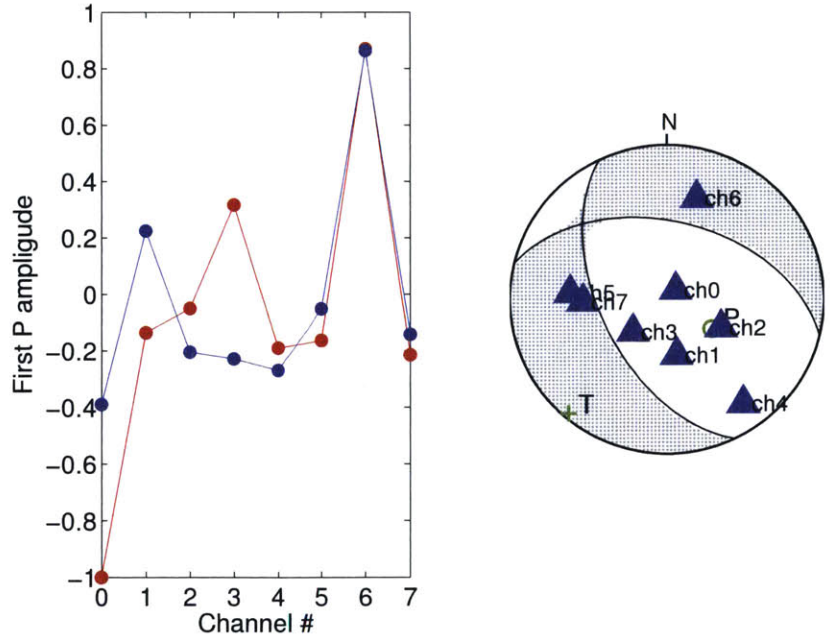

Figure 4-39: Moment tensor results for event 5629. Left: The first-P amplitude matching (Red: observed. Blue: synthetic). Right: The moment tensor solution.

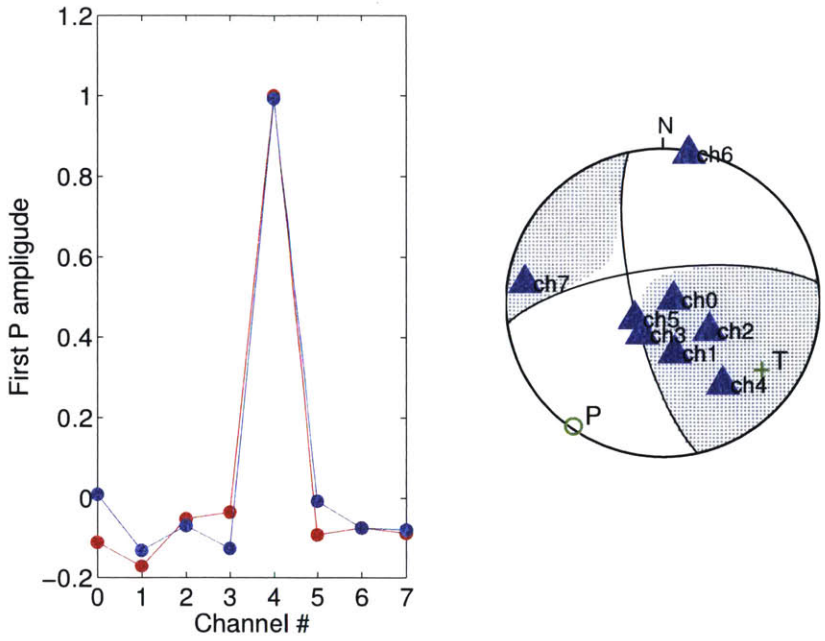

Figure 4-40: Moment tensor results for event 5701. Left: The first-P amplitude matching (Red: observed. Blue: synthetic). Right: The moment tensor solution.

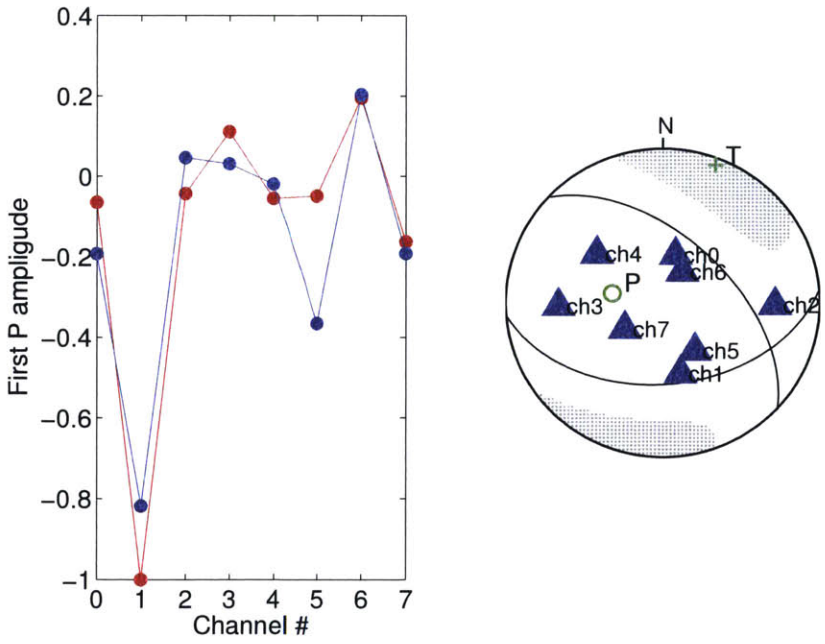

Figure 4-41: Moment tensor results for event 5705. Left: The first-P amplitude matching (Red: observed. Blue: synthetic). Right: The moment tensor solution.

Table 4.3: Location error from the active source experiment

Ch #	ΔX(mm)	ΔY(mm)	ΔZ(mm)
0	1.0	1.0	9.0
1	4.5	5.5	0.1
2	5.5	6.5	0.8
3	1.0	4.0	3.5
4	1.0	1.0	1.5
5	3.5	2.5	2.3
6	3.5	6.5	3.2
7	1.0	1.0	3.0

and equals to 250 samples. The arrival time picking error is only 1/10 of the typical wave length of the P-wave.

The order of 1 mm for the location is acceptable compared to the sample size, but what if we decrease the location error to the order of 0.1 mm? In order to decrease the location error to an order of 0.1 mm, we need to decrease the picking error of the P-wave arrivals to a couple of samples, or equally 1/100 of the typical wave period of the P-wave. This picking error is hard to achieve. A more realistic way is to increase use the high frequency PZT sensors to increase the dominant frequencies of the recorded AE data.

4.5.2 Sensor calibration

Sensor calibration is of great importance to apply any amplitude based analysis, e.g., moment tensor inversion. Although we applied the full moment tensor inversion to the AE data from the fracturing experiment, and the moment tensor results make some sensor considering the real fracturing processes, at the time when we recorded the AE data from Berea sandstone, the sensors were not calibrated. We actually had no idea about the real physical meaning of received signals, whether it was displacement, velocity, or acceleration. In addition, we assumed the instrument response and the coupling between the specimen and sensors were same for all the eight sensors. In order to calibrate the sensor, McLaskey et al. (2015) introduced a calibration technique using an *in situ* ball drop system during AE experiments. Since the momentum of a dropped ball is measurable, an *in situ* ball drop during the AE experiments could

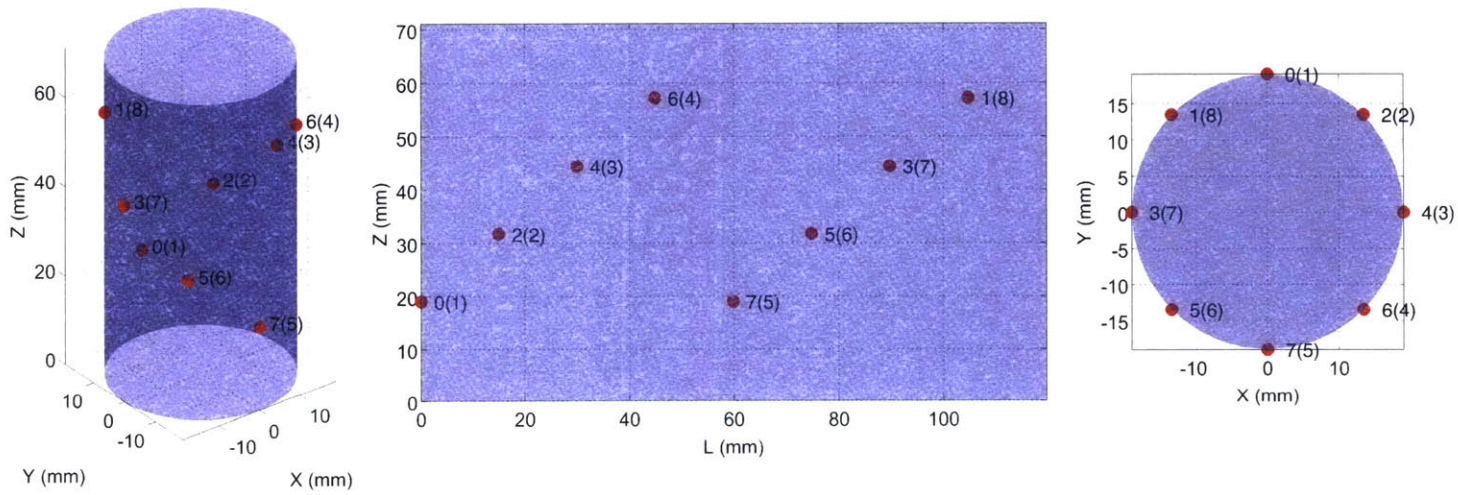

Figure 4-42: The scheme of the experimental system. Left: 3D view of the Lucite cylinder. The red circles show the position of the eight PZT sensors; Middle: Flat view of the expansion of the cylinder; Right: Top view of the cylinder.

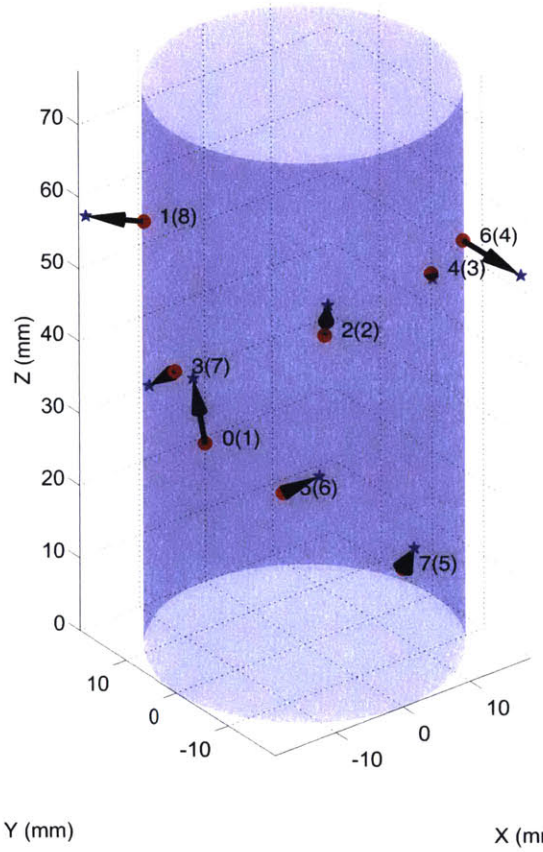

Figure 4-43: The recovery of the location of active sources. The blue star shows the located sensor position, the red circles show the true positions of the sensors, and the black arrow shows the discrepancies between the recovered the sensor positions and the true values.

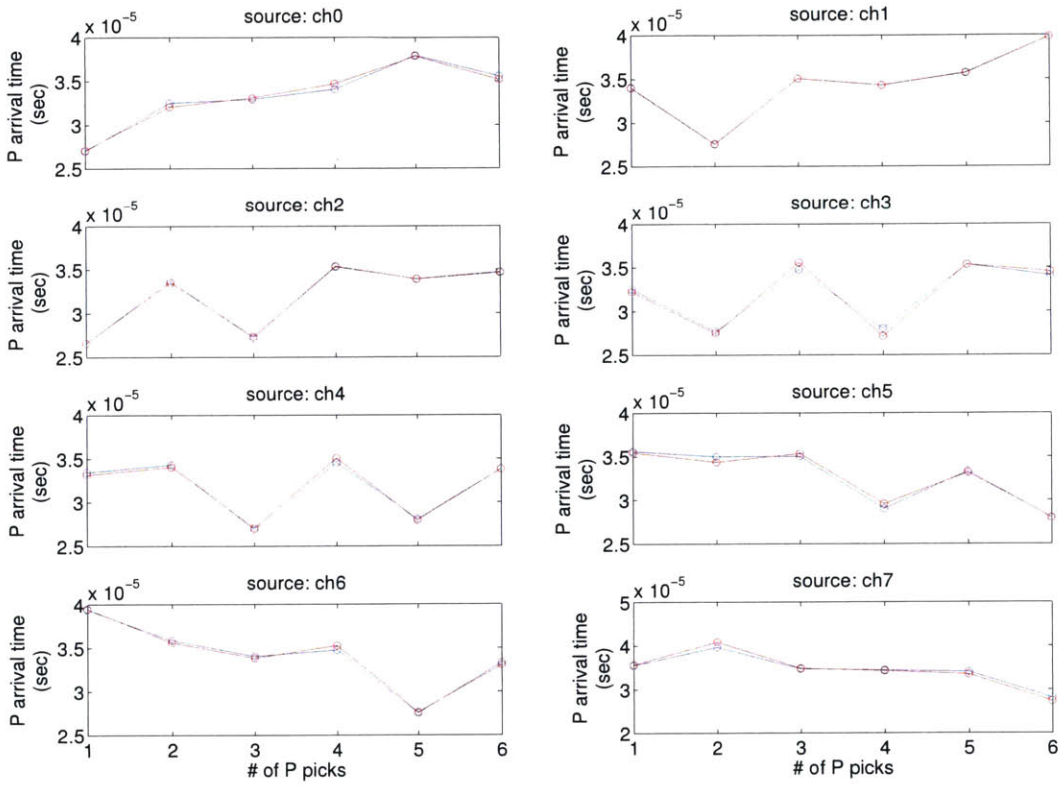

Figure 4-44: The comparison of the theoretical (blue) and observed (red) P-wave arrival time for eight active source tests.

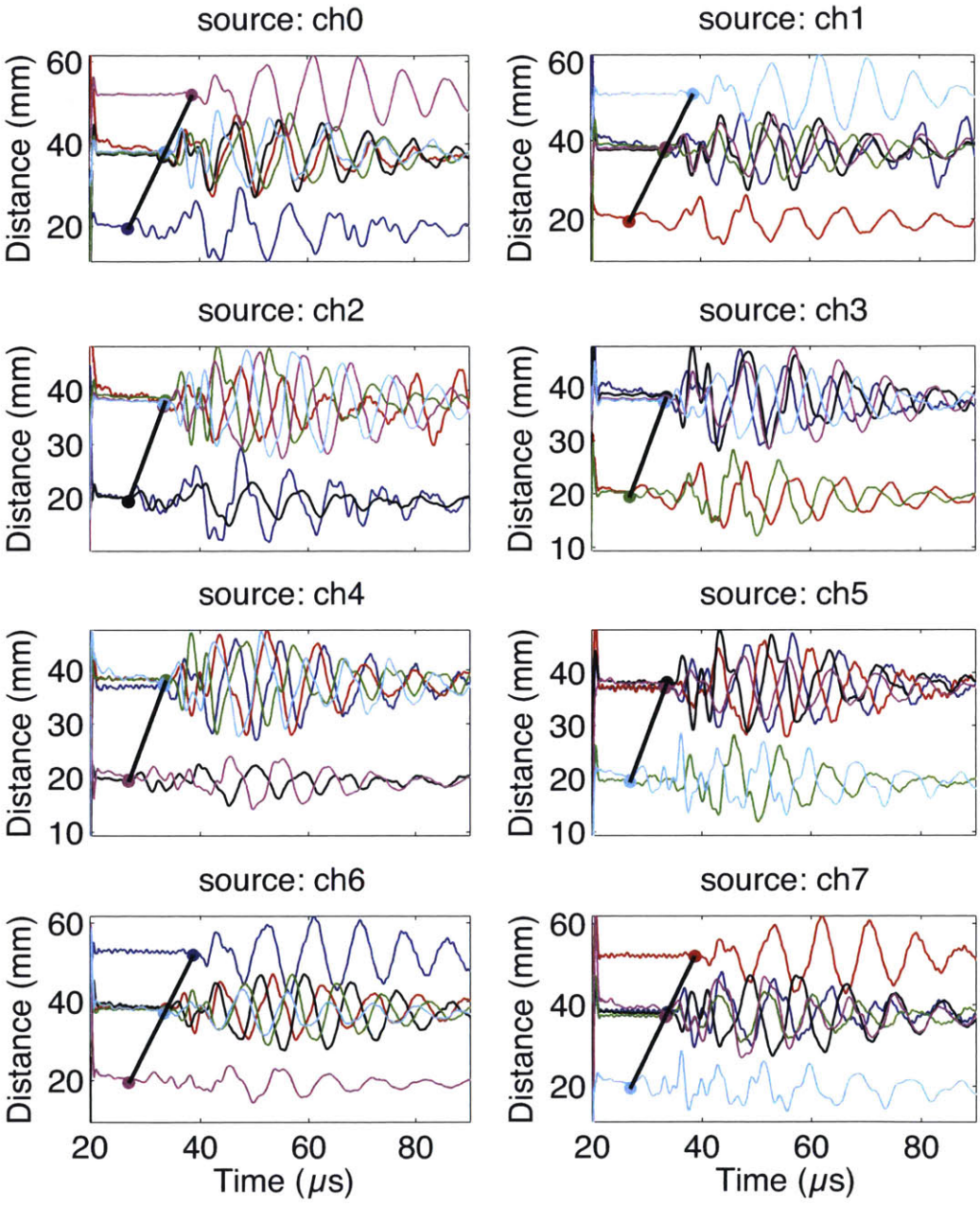

Figure 4-45: The waveforms from the eight active source tests. In each subplot, the waveforms are listed from the bottom to top, as the increase of the distance from the active source sensor. The black lines present the theoretical travel time Vs. distance for P-waves, which means the slope of the curves is the slowness of the P- and S-waves of Lucite.

convert the amplitude of any other AE sources, e.g. fracturing, to the momentum of the ball. The building of the *in situ* AE calibration system is still actively in progress in our lab.

Chapter 5

Conclusions

In Chapter 2, we introduced a waveform based Bayesian moment tensor inversion method. The method works well for recovering the source mechanisms and locations of earthquakes and enable us to obtain the uncertainties of the source parameters and locations from the posterior distributions of these parameters. We tested the Bayesian method using synthetic data and found that the fault geometry and DC component of the MT are determined most accurately. The uncertainties of isotropic and CLVD components were relatively larger than those of the DC components. Based on the synthetic simulation and the study of an induced seismic event from an oil/gas field, we can state that the uncertainty quantification of full moment tensor solutions is a powerful tool to estimate how reliable the source mechanism model is.

Future work could be done to further develop the Bayesian moment tensor inversion method in Chapter 2. First, a Gaussian error model was assumed to efficiently generate the marginal probability density function of seismic location giving waveform data. A more realistic error model based on the noise recording in the seismograms would be valuable to test. Second, an improper prior probability density function ($\boldsymbol{\pi_0}$ = constant) was assume. I could use stronger priors to better constrain the moment tensor and location parameters, e.g., the P-wave polarity, the P/S amplitude ratio, the phase travel time, or the characteristic marks from the waveform features. Third, I did not include the velocity model into the inversion, a more completed study in the future would provide a full description of the probability distribution of moment

tensor, location, and velocity model, based on observed seismograms.

Chapter 3 focused on the ground motion simulation in Kuwait due to regional and local earthquakes. In the regional earthquakes section, we calculated the potential largest ground motions, about 5 cm, due to a maximum Mw = 7. The regional velocity model has been validated by the good matching of the observed seismograms of the 08/18/2014 Mw 6.2 Iran-Iraq-borer earthquake with the synthetic seismograms. In addition, the amplification effects of soil layers on ground motions were discussed by conducting a finite difference model. A factor of two or three amplification can occur when a soil layer is placed on the top of original crustal material. In the second part, we focused on the local earthquakes in Kuwait, which have had an increasing occurrence rate recently. These earthquakes happen repeatedly in the same locations close to the oil/gas fields in Kuwait. We applied the source mechanism inversion to two local earthquakes (Mw4.5 in 03/21/2015 and Mw4.1 in 08/18/2015), which were recorded by both the Incorporated Research Institutions for Seismology (IRIS) and KNSN, and widely felt by people in Kuwait. The earthquakes are generally small (Mw $<$ 5) and are shallow, with focal depths of about 2 to 8 km. The depths for most of the local earthquakes are consistent with the reservoir depth – 2 to 4 km. We determined the location and source mechanism of these local earthquakes, with the uncertainties, using a Bayesian inversion method. Our results show that most likely these local earthquakes occurred on pre-existing faults and may have been triggered by oil field activities. In Kuwait, where oil fields are close to populated areas, these induced earthquakes could produce ground accelerations high enough to cause damage to sturctures near the earthquake epicenters.

More work could be done for the ground motion simulation for the whole Arabian penisula due to earthquake in the Zagros belts. This could provide a general picture of ground motion distribution in Arabian penisula and help the countries near the Zagros belt to generate more realistic building codes. For local earthquakes in Kuwait, a detailed shallow structure model would be inferred from the local seismic data, in order to determine the location and source mechanisms more accurately.

Chapter 4 applied three different event detection and three different location algo-

rithms to the acoustic emission (AE) data derived from the fracturing experiments in a cylindrical Berea sandstone sample (Diameter: 36.43 mm; Height: 76.7 mm). The first P-amplitude and waveform-based Bayesian moment tensor inversion algorithms have been applied to the AE data to study the source mechanisms of this fracturing related pico-seismicity. The migration of the AE event locations as a function of time showed a spatial and temporal evolution of microfractures in the specimen. At the beginning of the fracturing processes, a few AE events occurred randomly in the specimen. While, as the main fracturing, which was indicated by a rapid differential stress drop, occurred, the AE events increased significantly and tend to nucleate along the fracture. After the main fracturing processes, fewer events could be detected and these events are generally along the formed fracture planes, the geometry of which has been recovered by laser scanning the fractured specimen surface. One thing we should notice from the AE location during the main fracturing is that the events generally scatter all over the specimen although the trend of nucleation can be observed. This may be due to large errors on the smaller events or there could be many microfractures all over the samples. The larger evens with good waveforms during the main fracturing correlated well with the fractures. These may be because large events are occurring on the fracture are signal to noise ratio is high enough to locate them very accurately. The moment tensor analysis of the AE data shows a general dip-slip source mechanism for the selected events with good waveforms along the main fracture, and a vertical maximum compressional stress. However, some events indicated a horizontal maximum compressional stress, which may be because of the inhomogeneity of the specimen, or errors because the waveform amplitudes are without good sensor calibration.

The AE characterization for laboratory rock fracturing is of great challenge due to the large data size and the difficulties of amplitude calibration. On the other hand, because of the controllable laboratory fracturing process and the recoverable fracture geometry, the AE study has its own advantages for studying fracturing physics compared to using real earthquake data. For future work, I will develop a more efficient and automatic algorithm to analyze AE data accurately and reduce the labor work

such as phase picking. In addition, the AE data should be calibrated to present exact physical meaning. With these two prerequisites, we may design AE experiments mimicking real fracturing processes and develop the concepts to better describe the fracturing processes under geological conditions or human activities, e.g., hydraulic fracturing.

Bibliography

N Abrahamson and K Shedlock. Overview of ground motion attenuation relationships. *Seismological Research Letters*, 68(1), 1997.

J Al-Awadhi and V Midzi. The seismicity of the kuwaiti subregion. *Seismological Research Letters*, 72(4):462–473, 2001.

Abdulaziz M Almuhaidib and M Nafi Toksöz. Numerical modeling of elastic-wave scattering by near-surface heterogeneities. *Geophysics*, 79(4):T199–T217, 2014.

Firyal Bou-Rabee. Site selection for the field stations of the kuwait national seismic network. *Seismological Research Letters*, 70(6):712–717, 1999.

Firyal Bou-Rabee. Seismotectonics and earthquake activity of kuwait. *Journal of seismology*, 4(2):133–141, 2000.

Firyal Bou-Rabee and Amos Nur. The 1993 m4. 7 kuwait earthquake: Induced by the burning of the oil fields. *Kuwait J. Sci. Eng*, 29(2):155–163, 2002.

Firyal Bou-Rabee and Erik VanMarcke. Seismic vulnerability of kuwait and other arabian gulf countries: information base and research needs. *Soil Dynamics and Earthquake Engineering*, 21(2):181–186, 2001.

Michel Bouchon. A simple method to calculate green's functions for elastic layered media. *Bulletin of the Seismological Society of America*, 71(4):959–971, 1981.

Michel Bouchon. A review of the discrete wavenumber method. *Pure and applied Geophysics*, 160(3-4):445–465, 2003.

George J Carman. Structural elements of onshore kuwait. *GeoArabia*, 1(2):239–266, 1996.

M Çelebi and H-P Liu. Before and after retrofit–response of a building during ambient and strong motions. *Journal of Wind Engineering and Industrial Aerodynamics*, 77:259–268, 1998.

Mehmet Çelebi, Nafi Toksöz, and Oral Büyüköztürk. Rocking behavior of an instrumented unique building on the mit campus identified from ambient shaking data. *Earthquake Spectra*, 30(2):705–720, 2014.

G Cespuglio, P Campus, and J Šílenỳ. Seismic moment tensor resolution by waveform inversion of a few local noisy recordsii. application to the phlegraean fields (southern italy) volcanic tremors. *Geophysical Journal International*, 126(3):620–634, 1996.

MA Denolle, EM Dunham, GA Prieto, and GC Beroza. Ground motion prediction of realistic earthquake sources using the ambient seismic field. *Journal of Geophysical Research: Solid Earth*, 118(5):2102–2118, 2013.

MA Denolle, EM Dunham, GA Prieto, and GC Beroza. Strong ground motion prediction using virtual earthquakes. *Science*, 343(6169):399–403, 2014.

TF Drouillard. Introduction to acoustic emission technology. *Nondestructive testing handbook*, 5, 1987.

TF Drouillard. A history of acoustic emission. *Journal of acoustic emission*, 14(1): 1–34, 1996.

Thomas F Drouillard and Frances J Laner. Acoustic emission. a bibliography with abstracts. *IFI/Plenum,*, page 787, 1978.

Jing Du and Norm R Warpinski. Uncertainty in FPSs from moment-tensor inversion. *Geophysics*, 76(6):WC65–WC75, 2011.

Zacharie Duputel, Luis Rivera, Yukitoshi Fukahata, and Hiroo Kanamori. Uncertainty estimations for seismic source inversions. *Geophysical Journal International*, 190 (2):1243–1256, 2012.

Paul S Earle and Peter M Shearer. Characterization of global seismograms using an automatic-picking algorithm. *Bulletin of the Seismological Society of America*, 84 (2):366–376, 1994.

I El-Hussain, A Deif, K Al-Jabri, AME Mohamed, G Al-Rawas, MN Toksöz, N Sundararajan, S El-Hady, S Al-Hashmi, K Al-Toubi, et al. Seismic microzonation for muscat region, sultanate of oman. *Natural hazards*, 69(3):1919–1950, 2013.

William L Ellsworth. Injection-induced earthquakes. *Science*, 341(6142):1225942, 2013.

Sean R Ford, Douglas S Dreger, and William R Walter. Identifying isotropic events using a regional moment tensor inversion. *Journal of Geophysical Research: Solid Earth (1978–2012)*, 114(B1), 2009a.

Sean R Ford, Douglas S Dreger, and William R Walter. Source analysis of the memorial day explosion, kimchaek, north korea. *Geophysical Research Letters*, 36 (21), 2009b.

Colin Fox and Richard A Norton. Fast sampling in a linear-gaussian inverse problem. *arXiv preprint arXiv:1507.01614*, 2015.

WB Frank and NM Shapiro. Automatic detection of low-frequency earthquakes (lfes) based on a beamformed network response. *Geophysical Journal International*, 197 (2):1215–1223, 2014.

W Fu, BC Ames, AP Bunger, AA Savitski, et al. An experimental study on interaction between hydraulic fractures and partially-cemented natural fractures. In *49th US Rock Mechanics/Geomechanics Symposium*. American Rock Mechanics Association, 2015.

SD Goodfellow, MHB Nasseri, SC Maxwell, and RP Young. Hydraulic fracture energy budget: Insights from the laboratory. *Geophysical Research Letters*, 42(9):3179–3187, 2015.

Caroline C. Graham, Sergei Stanchits, Ian G. Main, and Georg Dresen. Comparison of polarity and moment tensor inversion methods for source analysis of acoustic emission data. *International journal of rock mechanics and mining sciences*, 47(1): 161–169, 2010. ISSN 1365-1609.

Francesco Grigoli, Simone Cesca, Maurizio Vassallo, and Torsten Dahm. Automated seismic event location by travel-time stacking: An application to mining induced seismicity. *Seismological Research Letters*, 84(4):666–677, 2013.

Christian U Grosse and Masayasu Ohtsu. *Acoustic emission testing*. Springer Science & Business Media, 2008.

Chen Gu, Youssef M. Marzouk, and M. Nafi Toksöz[1]. Waveform-based bayesian full moment tensor inversion and uncertainty determination for the induced seismicity in an oil/gas field. *Geophysical Journal International*, submitted.

Heikki Haario, Eero Saksman, and Johanna Tamminen. An adaptive metropolis algorithm. *Bernoulli*, pages 223–242, 2001.

JC Hampton, L Matzar, D Hu, M Gutierrez, et al. Fracture dimension investigation of laboratory hydraulic fracture interaction with natural discontinuity using acoustic emission. In *49th US Rock Mechanics/Geomechanics Symposium*. American Rock Mechanics Association, 2015.

W Keith Hastings. Monte carlo sampling methods using markov chains and their applications. *Biometrika*, 57(1):97–109, 1970.

Josef Horálek, Zuzana Jechumtálová, Louis Dorbath, and Jan Šílenỳ. Source mechanisms of micro-earthquakes induced in a fluid injection experiment at the hdr site soultz-sous-forêts (alsace) in 2003 and their temporal and spatial variations. *Geophysical Journal International*, 181(3):1547–1565, 2010.

Tsuyoshi Ishida, Kazuhei Aoyagi, Tomoya Niwa, Youqing Chen, Sumihiko Murata, Qu Chen, and Yoshiki Nakayama. Acoustic emission monitoring of hydraulic fracturing laboratory experiment with supercritical and liquid co2. *Geophysical Research Letters*, 39(16), 2012.

James Jackson and Dan McKenzie. Active tectonics of the alpinehimalayan belt between western turkey and pakistan. *Geophysical Journal International*, 77(1): 185–264, 1984.

Jari Kaipio and Erkki Somersalo. *Statistical and computational inverse problems*, volume 160. Springer Science & Business Media, 2006.

Jari Kaipio and Erkki Somersalo. Statistical inverse problems: discretization, model reduction and inverse crimes. *Journal of Computational and Applied Mathematics*, 198(2):493–504, 2007.

EJ Kaiser. A study of acoustic phenomena in tensile test. *Dr.-Ing. Dissertation. Technical University of Munich*, 1950.

Honn Kao and Shao-Ju Shan. The source-scanning algorithm: Mapping the distribution of seismic sources in time and space. *Geophysical Journal International*, 157 (2):589–594, 2004.

Marc C Kennedy and Anthony O'Hagan. Bayesian calibration of computer models. *Journal of the Royal Statistical Society: Series B (Statistical Methodology)*, 63(3): 425–464, 2001.

Monica D Kohler, Paul M Davis, and Erdal Safak. Earthquake and ambient vibration monitoring of the steel-frame ucla factor building. *Earthquake Spectra*, 21(3):715–736, 2005.

Jochen H Kurz, Christian U Grosse, and Hans-Wolf Reinhardt. Strategies for reliable automatic onset time picking of acoustic emissions and of ultrasound signals in concrete. *Ultrasonics*, 43(7):538–546, 2005.

Grzegorz Kwiatek, THW Goebel, and Georg Dresen. Seismic moment tensor and b value variations over successive seismic cycles in laboratory stick-slip experiments. *Geophysical Research Letters*, 41(16):5838–5846, 2014.

Gabi Laske, Guy Masters, Zhitu Ma, and Mike Pasyanos. Update on crust1. 0-a 1-degree global model of earths crust. In *EGU General Assembly Conference Abstracts*, volume 15, page 2658, 2013.

Junlun Li. *Study of Induced Seismicity for Reservoir Characterization*. PhD thesis, Massachusetts Institute of Technology, 2013.

Junlun Li, H Sadi Kuleli, Haijiang Zhang, and M Nafi Toksöz. Focal mechanism determination of induced microearthquakes in an oil field using full waveforms from shallow and deep seismic networks. *Geophysics*, 76(6):WC87–WC101, 2011a.

Junlun Li, Haijiang Zhang, H Sadi Kuleli, and M Nafi Toksoz. Focal mechanism determination using high-frequency waveform matching and its application to small magnitude induced earthquakes. *Geophysical Journal International*, 184(3):1261–1274, 2011b.

D Lockner and JD Byerlee. Hydrofracture in weber sandstone at high confining pressure and differential stress. *Journal of Geophysical Research*, 82(14):2018–2026, 1977.

Anthony Lomax, Jean Virieux, Philippe Volant, and Catherine Berge-Thierry. Probabilistic earthquake location in 3d and layered models. In *Advances in seismic event location*, pages 101–134. Springer, 2000.

Naoki Maeda. A method for reading and checking phase times in auto-processing system of seismic wave data. *Zisin= Jishin*, 38(3):365–379, 1985.

Shawn Maxwell et al. *Microseismic Imaging of Hydraulic Fracturing: Improved Engineering of Unconventional Shale Reservoirs*. Number 17. SEG Books, 2014.

TV McEvilly and EL Majer. Asp: An automated seismic processor for microearthquake networks. *Bulletin of the Seismological Society of America*, 72(1): 303–325, 1982.

Gregory C McLaskey, David A Lockner, Brian D Kilgore, and Nicholas M Beeler. A robust calibration technique for acoustic emission systems based on momentum transfer from a ball drop. *Bulletin of the Seismological Society of America*, 105(1): 257–271, 2015.

Nicholas Metropolis, Arianna W Rosenbluth, Marshall N Rosenbluth, Augusta H Teller, and Edward Teller. Equation of state calculations by fast computing machines. *The journal of chemical physics*, 21(6):1087–1092, 1953.

Marija Mustać and Hrvoje Tkalčić. Point source moment tensor inversion through a bayesian hierarchical model. *Geophysical Journal International*, 204(1):311–323, 2016.

Avinash Nayak and Douglas S Dreger. Moment tensor inversion of seismic events associated with the sinkhole at napoleonville salt dome, louisiana. *Bulletin of the Seismological Society of America*, 104(4):1763–1776, 2014.

Leonard Obert and Wilbur Duvall. Use of subaudible noises for the prediction of rock bursts, part ii, us bur. *Mines Rep*, 3654, 1942.

KB Olsen. Site amplification in the los angeles basin from three-dimensional modeling of ground motion. *Bulletin of the Seismological Society of America*, 90(6B):S77–S94, 2000.

KB Olsen, SM Day, JB Minster, Yifeng Cui, Amit Chourasia, Marcio Faerman, Reagan Moore, Philip Maechling, and Thomas Jordan. Strong shaking in los angeles expected from southern san andreas earthquake. *Geophysical Research Letters*, 33 (7), 2006.

KB Olsen, SM Day, LA Dalguer, J Mayhew, Y Cui, J Zhu, VM Cruz-Atienza, D Roten, P Maechling, TH Jordan, et al. Shakeout-d: Ground motion estimates using an ensemble of large earthquakes on the southern san andreas fault with spontaneous rupture propagation. *Geophysical Research Letters*, 36(4), 2009.

Kim B Olsen, Ralph J Archuleta, and Joseph R Matarese. Three-dimensional simulation of a magnitude 7.75 earthquake on the san andreas fault. *Science*, 270(5242): 1628, 1995.

Giuliano Francesco Panza and Angela Saraò. Monitoring volcanic and geothermal areas by full seismic moment tensor inversion: are non-double-couple components always artefacts of modelling? *Geophysical Journal International*, 143(2):353–364, 2000.

Michael E Pasyanos, Hrvoje Tkalčić, Rengin Gök, Abdullah Al-Enezi, and Arthur J Rodgers. Seismic structure of kuwait. *Geophysical Journal International*, 170(1): 299–312, 2007.

William S Pettitt. *Acoustic emission source studies of microcracking in rock.* PhD thesis, University of Keele, 1998.

A Pitarka, ME Pasyanos, RJ Mellors, and AJ Rodgers. Observation and simulation of long-period ground motions in the persian/arabian gulf from earthquakes in zagros thrust belt. Technical report, Lawrence Livermore National Laboratory (LLNL), Livermore, CA, 2012.

Arben Pitarka, Kojiro Irikura, Tomotaka Iwata, and Haruko Sekiguchi. Three-dimensional simulation of the near-fault ground motion for the 1995 hyogo-ken nanbu (kobe), japan, earthquake. *Bulletin of the Seismological Society of America*, 88(2):428–440, 1998.

Arben Pitarka, Abdullah Al-Amri, Michael E Pasyanos, Arthur J Rodgers, and Robert J Mellors. Long-period ground motion in the arabian gulf from earthquakes in the zagros mountains thrust belt. *Pure and Applied Geophysics*, 172(10): 2517–2532, 2015.

Germán A Prieto and Gregory C Beroza. Earthquake ground motion prediction using the ambient seismic field. *Geophysical Research Letters*, 35(14), 2008.

German A Prieto, Jesse F Lawrence, Angela I Chung, and Monica D Kohler. Impulse response of civil structures from ambient noise analysis. *Bulletin of the Seismological Society of America*, 100(5A):2322–2328, 2010.

AW Sadek. Seismic map for the state of kuwait. *Emirates Journal for Engineering Research*, 9(2):53–58, 2004.

Sudipta Sarkar. *Reservoir monitoring using induced seismicity at a petroleum field in Oman.* PhD thesis, Massachusetts Institute of Technology, 2008.

JC Savage and L Mansinha. Radiation from a tensile fracture. *Journal of Geophysical Research*, 68(23):6345–6358, 1963.

BH Schofield. Acoustic emission under applied stress. Technical Report ARL-150, Lessels and Associates, Boston, 1961.

CH Scholz. Experimental study of the fracturing process in brittle rock. *Journal of Geophysical Research*, 73(4):1447–1454, 1968a.

CH Scholz. Microfracturing and the inelastic deformation of rock in compression. *Journal of Geophysical Research*, 73(4):1417–1432, 1968b.

Christopher H Scholz. *Microfracturing of rock in compression.* PhD thesis, Massachusetts Institute of Technology, 1967.

Serge A Shapiro. *Fluid-Induced Seismicity.* Cambridge University Press, 2015.

J Šílenỳ, GF Panza, and P Campus. Waveform inversion for point source moment tensor retrieval with variable hypocentral depth and structural model. *Geophysical journal international*, 109(2):259–274, 1992.

J Šílenỳ, P Campus, and GF Panza. Seismic moment tensor resolution by waveform inversion of a few local noisy recordsi. synthetic tests. *Geophysical Journal International*, 126(3):605–619, 1996.

Jan Šílený, David P Hill, Leo Eisner, and Francois H Cornet. Non–double-couple mechanisms of microearthquakes induced by hydraulic fracturing. *Journal of Geophysical Research: Solid Earth (1978–2012)*, 114(B8), 2009.

Stuart A Sipkin. Estimation of earthquake source parameters by the inversion of waveform data: synthetic waveforms. *Physics of the Earth and Planetary Interiors*, 30(2-3):242–259, 1982.

Devinderjit Sivia and John Skilling. *Data analysis: a Bayesian tutorial.* OUP Oxford, 2006.

Roel Snieder and Erdal Şafak. Extracting the building response using seismic interferometry: Theory and application to the millikan library in pasadena, california. *Bulletin of the Seismological Society of America*, 96(2):586–598, 2006.

Fuxian Song. *Microseismic mapping and source characterization for hydrofracture monitoring: a full-waveform approach.* PhD thesis, Massachusetts Institute of Technology, 2013.

Fuxian Song and M. Nafi Toksöz. Full-waveform based complete moment tensor inversion and source parameter estimation from downhole microseismic data for hydrofracture monitoring. *Geophysics*, 76(6):WC103–WC116, November 2011. ISSN 0016-8033. URL `http://library.seg.org/doi/abs/10.1190/geo2011-0027.1`.

Sergei Stanchits, Sibylle Mayr, Serge Shapiro, and Georg Dresen. Fracturing of porous rock induced by fluid injection. *Tectonophysics*, 503(1):129–145, 2011.

Eva Stierle, Marco Bohnhoff, and Václav Vavryčuk. Resolution of non-double-couple components in the seismic moment tensor using regional networks – II: application to aftershocks of the 1999 Mw 7.4 Izmit earthquake. *Geophysical Journal International*, 196(3):1878–1888, 2014a. doi: 10.1093/gji/ggt503.

Eva Stierle, Vaclav Vavryčuk, Jan Šílenỳ, and Marco Bohnhoff. Resolution of non-double-couple components in the seismic moment tensor using regional networks – I: a synthetic case study. *Geophysical Journal International*, page ggt502, 2014b. doi: 10.1093/gji/ggt502.

Andrew M Stuart. Inverse problems: a bayesian perspective. *Acta Numerica*, 19: 451–559, 2010.

WH Swindell and NS Snell. Station processor automatic signal detection system, phase i: Final report, station processor software development. *Texas Instruments Report No. ALEX (01)-FR-77-01, AFTAC Contract Number FO8606-76-C-0025, Texas Instruments Incorporated, Dallas, Texas*, 1977.

Albert Tarantola. *Inverse problem theory and methods for model parameter estimation*. siam, 2005.

Dennise C Templeton and Douglas S Dreger. Non-double-couple earthquakes in the long valley volcanic region. *Bulletin of the Seismological Society of America*, 96(1): 69–79, 2006.

Václav Vavryčuk. Inversion for parameters of tensile earthquakes. *Journal of Geophysical Research: Solid Earth (1978–2012)*, 106(B8):16339–16355, 2001.

Václav Vavryčuk. Iterative joint inversion for stress and fault orientations from focal mechanisms. *Geophysical Journal International*, 199(1):69–77, 2014.

TH W Goebel, D Schorlemmer, TW Becker, G Dresen, and CG Sammis. Acoustic emissions document stress changes over many seismic cycles in stick-slip experiments. *Geophysical Research Letters*, 40(10):2049–2054, 2013.

Felix Waldhauser and William L Ellsworth. A double-difference earthquake location algorithm: Method and application to the northern hayward fault, california. *Bulletin of the Seismological Society of America*, 90(6):1353–1368, 2000.

Norman Raymond Warpinski and Jing Du. Source-mechanism studies on microseismicity induced by hydraulic fracturing. In *SPE Annual Technical Conference and Exhibition*. Society of Petroleum Engineers, 2010.

Haijiang Zhang, Sudipta Sarkar, M Nafi Toksöz, H Sadi Kuleli, and Fahad Al-Kindy. Passive seismic tomography using induced seismicity at a petroleum field in oman. *Geophysics*, 74(6):WCB57–WCB69, 2009.

Miao Zhang and Lianxing Wen. An effective method for small event detection: match and locate (m&l). *Geophysical Journal International*, 200(3):1523–1537, 2015.

Miao Zhang, Dongdong Tian, and Lianxing Wen. A new method for earthquake depth determination: stacking multiple-station autocorrelograms. *Geophysical Journal International*, 197(2):1107–1116, 2014.

Lupei Zhu and Donald V Helmberger. Advancement in source estimation techniques using broadband regional seismograms. *Bulletin of the Seismological Society of America*, 86(5):1634–1641, 1996.

Mark D Zoback and Steven M Gorelick. Earthquake triggering and large-scale geologic storage of carbon dioxide. *Proceedings of the National Academy of Sciences*, 109 (26):10164–10168, 2012.